MAGNETIC ARTIFICIAL CILIA FOR MICROFLUIDIC APPLICATIONS

A Ph.D. Dissertation Defense
Presented to
The Academic Faculty

By

Srinivas Hanasoge

In Partial Fulfillment
of the Requirements for the Degree
Doctor of Philosophy in the
George W. Woodruff School of Mechanical Engineering

Georgia Institute of Technology
December 2018

MAGNETIC ARTIFICIAL CILIA FOR MICROFLUIDIC APPLICATIONS

Approved By:

Dr. Peter Hesketh, Chair
G. W. Woodruff School of Mechanical Engineering
Georgia Institute of Technology

Dr. Alexander Alexeev
G. W. Woodruff School of Mechanical Engineering
Georgia Institute of Technology

Dr. Todd Sulchek
G. W. Woodruff School of Mechanical Engineering
Georgia Institute of Technology

Dr. Hang Lu
School of Chemical and Biomolecular Engineering
Georgia Institute of Technology

Dr. Amanda Stockton
School of Chemistry and Bio-chemistry
Georgia Institute of Technology

Date Approved: August 10, 2018

To Mira, Niveditha and Amma

ACKNOWLEDGEMENTS

I would like to express my deepest gratitude to my adviser Dr. Peter Hesketh. He devoted ample time towards educating me and provided all the freedom I needed to learn. His approach towards me encouraged me to try various ideas and learn a vast variety of things. His polite and humble attitude is something that I admire. I could not have asked for more from my adviser. Equally thankful to Dr. Alexander Alexeev. His approach to research has been very insightful and he has taught me a lot about writing. I thank him for treating me as one of his own students and helping me in my professional career. Working with them has certainly been a great learning experience and hopefully made me a good researcher. I thank Dr. Sulchek for not just being on my committee, but also for believing in my capabilities and offering me a position. I also thank my committee members Dr. Hang Lu and Dr. Amanda Stockton for reading my thesis and giving valuable inputs towards improving the quality of my work. Dr. Ynes Ortega and Dr. Marilyn Erikson from the University of Georgia for helping me with the bacteria capture experiments.

I have been immensely fortunate to be surrounded by people who I could always count on. I thank Sushruta Surappa for all the discussions, both academic and otherwise. Also for taking turns making the much-needed coffee. I thank past and present members of the lab, especially Matt Ballard and Drew Owen who inducted me into the group. I would also like to thank Ardalan Lotfi, Tzu-Hsuan Chang, Alireza. The undergraduate students I worked with helped me in the experimental setup; I would like to thank Ruwan Subashinga, John Nance and Chace McCard for their exceptional work. Louis Boulanger

from machine shop, Kyle French from the electronics lab have been instrumental in making accessories for my experiments. I thank cleanroom staff member Charlie Suh for accommodating my requests and maintaining the tools. I would also like to thank Dr. Wayne Whiteman for assigning a TA.

My friends, roommates, and first family in Atlanta - Kaivalya Bakshi, Karthik Rao, Subhrajit Charkaborty. I consider myself very fortunate to have met each one of you.

My parents Vishalakshi and Gowranga, brother Sushen, grandparents, and my parents-in-law have been the pillars of support throughout my graduate studies. My wife, Niveditha for the innumerable sacrifices she has made to see me succeed, grading home works and proof reading everything that I ever wrote. My newborn daughter, Mira who motivated me to graduate sooner. I hope I have made all of you proud.

CONTENTS

ACKNOWLEDGEMENTS iv

LIST OF TABLES x

LIST OF FIGURES xi

LIST OF VIDEOS IN ELECTRONIC SUPLEMENTAL INFORMATION xvi

LIST OF VARIABLES AND ABBREVIATIONS xvii

SUMMARY xviii

Chapter 1. INTRODUCTION 1

1.1 Micro scale fluid dynamics- Viscosity dominated flows 1

1.2 Motivation – Food safety and microfluidics 4

1.3 Artificial cilia – so far. 7

1.4 Organization of the thesis 10

Chapter 2. FABRICATION AND ACTUATION OF ARTIFICIAL CILIA 12

2.1 Microfabrication of cilia 13

2.2 Characterization of magnetic thin films 17

2.2.1 Measuring the composition 18

2.2.2 Stress in the free standing thin film 19

2.3 Soft lithography – Fabricating PDMS channels 22

2.4 Actuation of the filaments 23

2.5 Fluid transport by arrays of cilia 26

2.6 Summary 28

Chapter 3. KINEMATICS OF BEATING MAGNETIC CILIA 29

3.1 Introduction 30

3.2 Experimental and computational methodology 31

3.2.1 Experiments 32

3.2.2 Approximation of the magnetic force: 33

3.2.3 COMSOL Model 34

3.3 Results and discussion 34

3.3.1 Counter-clockwise rotation of magnetic field 36

3.3.2 Clockwise rotation of magnetic field 42

3.4 Dimensionless parameters 46

3.5 Characterizing the asymmetric strokes 47

3.6 Summary 53

Chapter 4. FLUID TRANSPORT CHARACTERISTICS OF ARRAYS OF ARTIFICIAL MAGNETIC CILIA 55

4.1 Introduction 55

4.2 Setup and experimental protocol of pumping experiments 58

4.3 Results and discussion 61

4.3.1 Fluid pumping by ciliary array 61

4.4 Microfluidic mixing 69

4.5 Conclusions 71

Chapter 5. METACHRONAL MOTION OF ARTIFICIAL CILIA 73

5.1 Introduction 73

5.2 Designing cilia that respond differently to the same force 75

5.2.1 Varying length across the array 77

5.2.2 Varying thickness across the array 87

5.2.3 Varying width across the array 91

5.3 Applying different forcing to each cilium 93

5.3.1 Translating the magnet 93

5.3.2 Rotating a magnet that is offset from the array center 95

5.4 Summary 97

Chapter 6. INDIVIDUAL CONTROL OF CILIA 99

6.1 Fabrication 101

6.2 Operation 102

6.2.1 Static magnetic field: 103

6.2.2 Oscillating magnetic field 103

6.3 Summary 105

Chapter 7. BIOMIMETIC CAPTURE 106

7.1 Introduction 106

7.2 Experimental setup 108

7.3 Surface functionalization 108

7.4 Particle capture experiments and results 110

7.4.1 Capture efficiency 115

7.5 Specificity of capture 117

7.6 Bacteria capture results 119

7.7 Summary 122

Chapter 8. CONCLUSIONS 124

8.1 Concluding remarks 124

8.2 Contributions of this thesis 128

8.3 Outlook for future development for other applications 129

APPENDIX A 130

APPENDIX B 132

REFERENCES 135

LIST OF TABLES

Table 1: Steps and conditions used for the first photolithography step in fabricating magnetic cilia. 15

Table 2: Steps and conditions used for the first photolithography step in fabricating magnetic cilia. 15

LIST OF FIGURES

Figure 1-1: a) Reciprocating swimmer propels itself if inertial effects are significant. b) No net motion of the swimmer if viscous forces are dominant. 2

Figure 2-1: Flowchart of the fabrication process showing the two steps-deposition of copper followed by NiFe layer, and titanium anchor layer. 16

Figure 2-2: SEM image of super critically dried cilia. 18

Figure 2-3: TEM dispersion spectroscopy images of the filament. **a**) Distribution of nickel in the filament. **b**) Distribution of iron in the filament. **c**) Combined distribution of Ni and Fe. **d**) Energy dispersion spectroscopy results of the filament revealing the composition. 19

Figure 2-4: Various defects in the filaments due to residual stress in the NiFe layer. 20

Figure 2-5:**a**) TEM images of the NiFe layer showing the surface roughness. **b**) Selected area electron diffraction (SAED) image of the NiFe thin film showing the cryptographic structure. **c**) grain size analysis of the NiFe layer. 21

Figure 2-6: Flowchart for fabricating the PDMS devices. The Su8 mold is first made on Silicon wafer. PDMS channel replicas are then made using the mold. The PDMS channels are plasma bonded on glass devices. 23

Figure 2-7: **a)** Schematic of the experimental setup showing the actuation of an array of cilia using a permanent rotating magnet. **b**, **c**, **d**, **e)**: Series of experimental images of an array of cilia actuated by a rotating magnet, as viewed from the bottom. **b)** Position of cilia when the magnetic field is horizontal, and cilia are relaxed. **c)**, **d)** Changing positions of the cilia as the magnetic field is being rotated from the horizontal to the vertical direction. **e)** Position of cilia when the field is normal to the substrate. 25

Figure 2-8: Fluid circulation produced by an array of magnetic cilia. The four columns of cilia are anchored on the opposite ends producing fluid pumping in the directions shown by the arrows. This leads to the fluid circulations as shown by the streaklines. Cilium dimensions are $200\mu m \times 20\mu m \times 70nm$ and the actuation frequency is $50Hz$. (See Video 1) 27

Figure 3-1**:** Schematic of the experimental setup showing the relative positioning of the cilium on the microscope with respect to the magnet. Note the cilium oscillation plane ($x-y$) is captured by the microscope. 31

Figure 3-2: Magnetic cilium oscillation due to a CCW rotating magnetic field in the $x-y$ plane (**a**) Experimental snapshots of a cilium with the following parameters: $L = 480\mu m$, $W = 10\mu m$, $Th = 55nm$, $\omega = 0.3Hz$, $B = 600Gauss$, $\mu = 1cP$. These parameters correspond to $Sp = 3.6$ and $Mn = 4.1$. Cilium positions ***P1*** and ***P2*** indicate

the beginning of the forward and recovery strokes, respectively. The tip trajectories during the forward and recovery strokes are shown by the solid and dotted lines, respectively. The snapshots are obtained from Video 2, in supplemental material. (**b**) Trajectory of the cilium obtained using computer simulations. 37

Figure 3-3: Cilium positions *a-e* at selected times throughout one oscillation cycle for CCW rotation of the magnetic field. Black arrows indicate the direction of the external magnetic field. The magnitude and direction of the applied magnetic moment along the cilium length are shown in red as a distribution plotted normal to the local cilium axis for the corresponding positions. Note that the magnetic moment varies continuously along the length..... 41

Figure 3-4: Cilium kinematics for the clockwise rotation of magnetic field. **a)** Overlay of experimentally recorded time lapse, from Video 2. **b)** Computer simulations obtained using COMSOL multiphysics. Cilium length is $L = 480\mu m$, and the actuation frequency is $1Hz$ 44

Figure 3-5: Cilium positions *a-e* at selected times throughout one oscillation cycle for CW rotation of the magnetic field. Black arrows indicate the direction of the external magnetic field. The magnitude and direction of the applied magnetic moment along the cilium length are shown in red as a distribution plotted normal to the local cilium axis for the corresponding positions. Note that the magnetic moment varies continuously along the length..... 45

Figure 3-6: Experimental trajectories of cilium tip normalized by cilium length. (**a**) Tip trajectories for different values of sperm number Sp varied by changing the frequencies magnetic field rotation. The arrow indicates tip trajectories with increasing Sp. (**b**) Tip trajectories for different values of magnetic number Mn varied by changing $\mathbf{B}$. The arrow shows the trajectories with decreasing Mn 49

Figure 3-7: (**a**) Normalized time difference between forward and recovery stroke as a function of sperm number Sp for different magnetic numbers Mn. (**b**) Normalized magnitude of cilium deflection as a function of sperm number Sp for different magnetic numbers Mn. The empty markers represent $Mn = 3.6 \pm 0.12$ and the filled markers represent $Mn = 3.1 \pm 0.08$. ○: $B = 600Gauss$, $L = 480\mu m$, $Th = 56nm$, $\mu = 1cP$; Δ: $B = 760Gauss$, $L = 480\mu m$, $Th = 68nm$, $\mu = 4cP$; ∇: $B = 760Gauss$, $L = 480\mu m$, $Th = 68nm$, $\mu = 2.1cP$; □: $B = 600Gauss$, $L = 480\mu m$, $Th = 68nm$, $\mu = 1cP$; ●: $B = 530Gauss$, $L = 480\mu m$, $Th = 56nm$, $\mu = 1cP$; ▲: $B = 650Gauss$, $L = 480\mu m$, $Th = 68nm$, $\mu = 4cP$; ▼: $B = 650Gauss$, $L = 480\mu m$, $Th = 68nm$, $\mu = 2.1cP$; ■: $B = 600Gauss$, $L = 430\mu m$, $Th = 56nm$, $\mu = 1cP$ 51

Figure 4-1: Schematic of experimental setup showing a microchannel loop through which the fluid pumped by cilia is circulated. A large diametrically magnetized permanent magnet is used to actuate the cilia. Inset shows actuated ciliary array as seen from the top for two different positions of the magnetic field. 59

Figure 4-2: Dimensionless pumping rate P_f as a function of Sp, for CCW and CW rotation of the magnetic field actuating a ciliary array. The array has 16 rows of cilia with 25 cilia per row. Spacing between array rows is $S = 250\mu m$, channel height is $H = 300\mu m$. 62

Figure 4-3: **a**) Dimensionless pumping rate P_f produced by ciliary arrays with different number of rows as a function of Sp for CCW rotation of the magnetic field actuating cilia. **b)** Pumping rate per row P_f / N as a function of the normalized distance C/D of the magnet from the center for an array with $N = 3$. The arrays have 25 cilia per row with spacing $S = 300\mu m$. Channel height is $H = 300\mu m$ 64

Figure 4-4: Dimensionless pumping rate P_f as a function of Sp for ciliary arrays with different spacing between consecutive rows. All arrays have four rows of cilia with 25 cilia per row. Channel height is $H = 300\mu m$. 67

Figure 4-5: Dimensionless pumping rate P_f as a function of normalized channel height H/L for selected values of *Sp*. A ciliary array with four rows of cilia, and 25 cilia per row is used. Spacing between rows of cilia is $S = 250\mu m$. 68

Figure 4-6: Mixing produced in a microchannel with two fluid streams. Inlet on the left shows two streams of fluid. The flowrate in the microchannel is $10\mu l / \min$. **a)** Cilia are not active, remaining flow streams unmixed. **b)** Cilia are actuated at $50Hz$ leading the merging of the two fluid streams. **c)** Steady state flow in the channel with actuated cilia results in highly mixed streams of fluid downstream. See Video 4 in ESI. 70

Figure 5-1: Schematic of the experimental setup with an array of cilia with linearly varying lengths actuated by a permanent magnet rotating,..... 77

Figure 5-2: **a-c)** Snapshots of the ciliary array at time $T = 0.1$, $T = 0.25$, and $T = 0.45$, respectively. Two rows of cilia are shown with cilium - $10\mu m$ in width and length changing form $60\mu m$ to $600\mu m$. The magnet is rotated counter clockwise with a frequency of $0.5Hz$. Metachronal motion can be viewed from left to right from below the glass substrate, with the wave front indicated by the arrow. See ESI for Video 5 of metachronal wave motion in ciliary arrays. 79

Figure 5-3: Position of the metachronal wave front $\chi = X/L_A$, where L_A is the array length, as a function of time T. Time T is normalized by the period of magnet rotation (T_o). 80

Figure 5-4: Motion of a single cilium in a beating cycle with length **a)** $L = 200\mu m$ and **b)** $L = 480\mu m$ The yellow and red arrows indicate the forward and recovery strokes, respectively. The green arrow is tangent to the cilium tip and the blue arrow indicates the direction of the magnetic field. 81

Figure 5-5: **a**) Plot of normalized trajectory of cilium tip of different lengths obtained through recording the beating pattern in the side view. **b**) The tip angle of beating cilia as a function of time T. The dotted lines show the rotational angle of the magnetic field. The angles are measured with respect to the substrate and are normalized by 2π. Time is normalized by the period of the external magnetic field rotation equal to $2s$. 84

Figure 5-6: Cycle completion time T_c as a function of cilium position χ for various experimental conditions. Note that data points collapse onto separate curves depending on Mn_L, indicating the weak dependence on Sp_L. The symbols ▲ and ▲ represent data obtained for $Mn_L = 7.4mm^{-1}$, $Sp_L = 6.6mm^{-1}$ from arrays with $150\mu m$ and $300\mu m$ spacing between cilia, respectively. 86

Figure 5-7: T_c as a function of Mn for cilia of various lengths. 87

Figure 5-8: a) Schematic of the shadow setup used to fabricate cilia of increasing thickness. **b**) Measured thickness across a row of cilia. **c**) Snapshots at different instances of time as the metachronal motion propagates from left to right across the row of cilia. Red arrows indicate the position of the wave front. **d**) Cycle completion time T_c as a function of Mn for various cilia of different lengths and thicknesses. 89

Figure 5-9: Flow produced by an array of cilia with varying cilium lengths. The fluid motion is the combined effect of metachronal motion and differences in kinematics due to changing lengths. 91

Figure 5-10: Array of cilia with varying cilium widths beat synchronously with no metachronal motion when actuated by a rotating magnetic field. $L = 200\mu m$, $W = 4\mu m - 40\mu m$ 92

Figure 5-11: Schematic of the experiment with magnet translating along an array of cilia. The cilia are actuated from right to left in a sequential manner as the magnet translates. 93

Figure 5-12: Metachronal motion in an array of cilia due to a magnet translating along the direction of the array. Cilium properties $L = 80\mu m$, $W = 8\mu m$, $P = 60nm$ 95

Figure 5-13: **a**) Schematic of the experimental setup with the magnet moved diagonally across an array. **b**) Snapshots at different times showing the propagation of the metachronal wave from left to right (See Video 9 in ESI). 96

Figure 6-1: Schematic of electrostatic actuation of the cilia. A patterned layer of gold is used as the bottom electrode, and the cilia act as the top electrode. 100

Figure 6-2: Flow chart showing the fabrication process for electrostatically actuated cilia. 102

Figure 6-3: Deflection of cilia for various values of voltage applied across the plates.. 103

Figure 6-4: Snapshots from the Video 10. **a)** Voltage is OFF and all the cilia are actuated. **b)** Voltage is ON and the cilia over the bottom electrode – 'GT' are immobilized, while the other continue to oscillate. 104

Figure 7-1: **a**) Mechanism of particle capture using magnetic cilia. The red dots indicate the particles captured on the cilia surface. **b**) schematic of the experimental setup consisting of a closed loop microchannel with cilia incorporated on one side. **c**) Immobilization of streptavidin beads on the NiFe cilia. **d**) Microscope image of Dynabeads M270 immobilized on the cilia and glass surface. 109

Figure 7-2: Snapshots of the ciliary array at different instances of time during a capture experiment. Note the increase in the number of fluorescent particles captured from 1min to 15mins. These images are taken for a cilia oscillation frequency $f = 8.3Hz, Sp = 1.9$, and particle concentration of $10^5/ml$ 111

Figure 7-3: Number of particles captured as a function of time for different oscillation frequencies of the cilia. 16 rows of $200\mu m$ length, $20\mu m$ width cilia were used for these experiments. 112

Figure 7-4: a) Comparison between the number of particles capture on the stationary glass surface and oscillating ciliary surface. b) Negligible particles captured on defective cilium that is not released. 113

Figure 7-5: Number of particles captured per cilium after $30s$ of oscillation, as a function of Sp 114

Figure 7-6: Particle concentration in the microchannel normalized with the initial concentration versus time. As the cilia oscillate to induce flow, the particles are captured and therefore the number of particles in the channel depletes. 40 rows of $80\mu m$ length, $8\mu m$ width cilia were used for these experiments. 116

Figure 7-7: **a**) Initial concentration of carboxyl beads and biotin particles. **b**) Final concentration of carboxyl and biotin particles after the device is washed. **c**) Comparison of the initial and final concentration of the particles in the device. Note the higher number of biotin particles captured point to the specificity of capture. 118

Figure 7-8: Schematic showing how the antibody is immobilized to the cilia. 120

Figure 7-9: Bacteria capture with anti-body immobilized cilia. **a)** The GFP tagged fluorescent salmonella are selectively captured by the cilia. Very few cells attach to the bottom glass substrate. **b)** Close up of the captured salmonella cells on the cilia surface. Notice that the cells stick mostly to the edges of the cilium. 121

LIST OF VIDEOS IN ELECTRONIC SUPLEMENTAL INFORMATION

Video 1: Fluid transport produced by an array of cilia.

Video 2: Side view motion picture showing the beating pattern of a cilium under the influence of a CCW rotating magnetic field.

Video 3: Simultaneous actuation of all cilia by a rotating magnetic field.

Video 4: Mixing of two fluid streams in a microchannel by magnetic cilia.

Video 5: Metachronal motion due to changing length across the array.

Video 6: Metachronal motion propagating in multiple directions simultaneously.

Video 7: Metachronal motion due to thickness variation across the array.

Video 8: No metachronal motion is obtained by varying the width of the cilium.

Video 9: Metachronal motion due to varying magnetic field across the array.

Video 10: Electrostatic actuation of cilia.

LIST OF VARIABLES AND ABBREVIATIONS

$\mathbf{B}$	Magnetic flux density vector
Re	Reynolds Number
D	Diameter of the magnet
Mn	Magnetic Number
Sp	Sperm Number
L	Length of Cilium
W	Width of Cilium
P	Thickness of Cilium
f	Frequency of oscillation (Hz)
ω	Angular frequency, $\omega = 2\pi f$ (rad/s)
t_s	Dimensionless cilium stroke time ratio
δ_s	Normalized cilium deflection amplitude ($\delta_s = \delta_{\max}/L$)
U_0	Centerline fluid velocity
P_f	Dimensionless pumping parameter
S	Spacing between the rows of cilia in an array
I	First Moment of Inertia
H	Microfluidic Channel Height
f_s	Self-Propelling Frequency
Q	Volumetric Flowrate
$S_{Package}$	Overall Working Volume of the Array
N	Number of ciliary Rows
T	Normalized time (Normalized by the period)
θ	Normalized cilium time angle (Normalized by 2π)
T_c	Normalized cycle completion time
t	Time
ρ	Density
E	Young's Modulus
ξ	Drag coefficient
μ	Dynamic Viscosity

SUMMARY

Biological organisms use hair-like cilia and flagella to perform fluid manipulations essential for their function and survival. This work aims at developing synthetic analogs of biological cilia. The fabrication, actuation, beating kinematics, and applications of bio-mimetic magnetic cilia that can be integrated into MEMS devices to enhance their functionality is detailed. Applications of the cilia to create metachronal waves, fluid mixing, and bacteria capture are demonstrated.

In this work, a simple lithographic technique to realize metallic thin film cilia is developed. The magnetic cilia can be driven to oscillate with highly asymmetric strokes using a simply rotating magnetic field. The beating of the synthetic cilia resembles the beating of biological cilia. The fabrication method follows standardized steps of thin-film microfabrication which allows for a higher degree of accuracy and reproducibility. The asymmetric motion opens the possibility of harnessing such synthetic cilia for fluid pumping and other fluid manipulations. A computational model is employed for analyzing the fluid structure interactions and to validate and further examine cilium motion due to a rotating magnetic field. The key parameters governing cilium motion are established and the actuation regimes enhancing asymmetry of cilium beating are identified.

The combined effect of multiple beating cilia generates rapid microfluidic pumping. The flow produced by the ciliary array depends on many factors like the direction of magnet rotation, the cilia properties, dimensions of ciliary array, and the microchannel dimensions. All these parameters are varied to characterize the fluid

flow produced. It is found that the cilia arrays can generate transitional flow speeds of up to $1.4mm/s$ corresponding to a flow rate of $11\mu l/\text{min}$ in closed-loop micro channels. These flow rates are the highest reported for such ciliary systems. Furthermore, optimum operating conditions for maximum pumping are established.

Inspired by biological cilia, it is shown that artificial cilia can be actuated in a sequential metachronal fashion. Multiple methods are explored to achieve sequential actuation of the cilia. The difference in magnetic cilium properties control the phase of the beating motion. This property is used to induce metachronal waves within a ciliary array and explore the effects of operation parameters on the wave motion. The metachronal motion in the artificial system is shown to depend on the magnetic and elastic properties of the filaments, unlike natural cilia, where metachronal motion arises due to fluid coupling.

Microorganisms use biological cilia to create various kinds of transport, and most important among them is the transport of suspended particles. Biological cilia are shown to effectively capture and trap specific particles for feeding. Motivated by this, the use of artificial magnetic cilia to capture particles suspended in a fluid is proposed. Perhaps, such nature-inspired ciliary capture and isolation of particles can be incorporated in microfluidic lab-on-chip devices for pre-concentration of cells and analytes. The particle capture capabilities of magnetic cilia are demonstrated and characterized. The surface of cilia is functionalized by the target specific receptor and the target is captured on the ciliary surface upon contact. It is found that maximum particle capture is obtained for same operating conditions that produce the maximum pumping. Furthermore, *Salmonella* bacteria capture on the surface of the cilia is demonstrated as a proof of concept.

Thus, the developed thin film magnetic cilia can find application in a wide variety of microfluidic devices. The ease of fabrication, actuation and reliability in operation make such cilia an attractive option for various applications. They can easily be incorporated into any microscale device where precise control and metering of fluid is necessary. Furthermore, they can be used to study and better understand the fluid transport produced by biological cilia.

Chapter 1. INTRODUCTION

1.1 Micro scale fluid dynamics- Viscosity dominated flows

Dr. Feynman remarked "there is plenty of room at the bottom" pointing to the potential to develop micro and nano devices. Today, the use of semiconductor fabrication technology for making microscale electro-mechanical devices (MEMS) has become widespread and such devices are often used as sensors and actuators in various applications. Biomimetic MEMS devices have gained significant attention in the recent past. Researchers have developed devices to perform microscale sensing, actuation, and other important functions in a manner that is inspired by biological organisms. In this context, microscale fluid handling is a particularly promising field for biomimetic MEMS design, as all of the biology exists in or around fluids. Such biomimetic fluid manipulation can be extremely useful in various lab-on-a-chip platforms for biomedical applications[1].

The most important characteristic of a bio-MEMS device is the length scale, in the order of micrometers. To achieve fluid transport at these micrometer length scales is difficult owing to the lack of inertial effects[2,3]. Fluid transport is governed by the ratio of inertial to viscous effects, and characterized by the Reynolds number, which is small ($<<1$) for these devices. In these regimes, the fluid transport is dominated by the fluid viscosity and the inertial effects are negligible.

To understand the effect of fluid inertia, consider a reciprocating swimmer in water (Figure 1-1a). The swimmer performs symmetric oscillations traversing the same

path in the forward and recovery strokes. The reciprocating tail pushes fluid against the direction of swim and the swimmer is capable of propelling itself. The propulsion mechanism in this case is mostly due to fluid inertia. Indeed most large fish and aquatic animals swim in this fashion. Trailing vortices are often observed downstream the swimmer, which is an inertial effect. The same reciprocating swimmer, however, will find it extremely difficult to swim in a fluid that is more viscous than water (Figure 1-1b). The increase in viscosity increases the frictional forces that the swimmer needs to overcome to propel itself. In these situations, the $Re << 1$, and the fluid transport is viscosity dominated. Microorganisms, owing to their small size operate in these regimes of negligible Re.

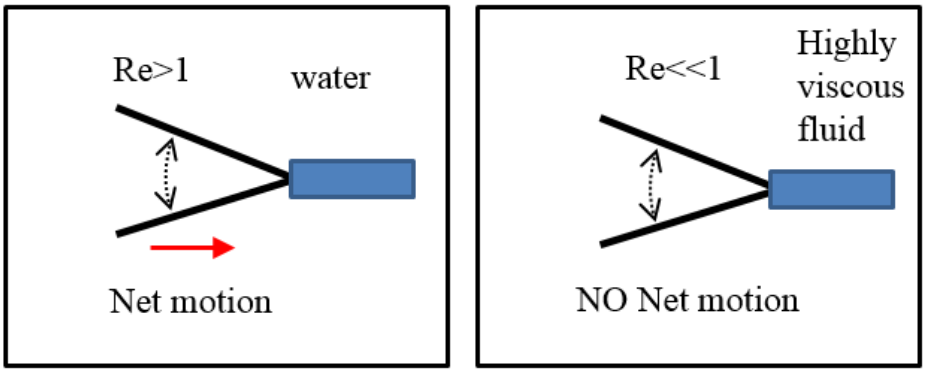

Figure 1-1: a) Reciprocating swimmer propels itself if inertial effects are significant. b) No net motion of the swimmer if viscous forces are dominant.

Interestingly, microorganisms and cells that usually operate in these inertia-less regimes have evolved to use organelles such as cilia and flagella with complex beating patterns yielding a net fluid transport[4–6]. Cilia are hair like structures that protrude from the cell body, and flagella are tail like organelles. A mere spatially symmetric oscillation

of these organelles is not sufficient to produce any net fluid transport[3]. They beat in a complex fashion involving a non-reciprocal, spatially asymmetric beating pattern in order to induce a net fluid flow. Cilia and flagella performing such complex beating is imperative to the organism in performing vital biophysical functions.

Naturally occurring cilia is found on nearly all mammalian cells. They aid in cell cycle progression and proliferation, and play a vital part in human and animal development and in everyday life. Natural cilia are broadly divided into two categories. **Motile** – moving cilia and **non-motile** – primary cilia. Motile cilia, such as the ones in human lungs, and respiratory tract, function to transport fluid and particles and keep the airways clear. Non-motile cilia usually perform functions of sensing nearby cells and the fluid around it. For example, in the kidney, cilia detect the flow of urine and send sensory signals. Dysfunction or defects in motile and non-motile cilia are understood to underlie a number of devastating genetic conditions - termed ciliopathies. It also known that flow produced by motile cilia determines the left-right asymmetry of the embryo[7,8]. Ciliary bands are used to produce feeding currents that draws the food particles towards the mouth of the organism for feeding[9,10]. Cilia also facilitate organism swimming[10,11]. Cilia are also seen in many parts of the human body. For example, the beating of cilia in the fallopian tubes moves the ovum from the ovary to the uterus, the inner lining of the nasal tract is kept clean by the constantly beating cilia.

The development of synthetic cilia that can perform similar non-reciprocal, spatially asymmetric beating pattern could prove useful for similar fluid and particle transport in lab-on-a-chip and bio-MEMS devices[12–16]. Furthermore, such synthetic systems can help us understand the functioning of natural cilia.

Artificial flagella has also been of interest among researchers in the recent years for various applications. Dreyfus et al.[17] have tethered red blood cells with an artificial flagella made of chains of magnetic particles and demonstrated its swimming mechanism. Researchers have also demonstrated coiled filaments that act as flagella for single cell drug delivery[18–22]. Acoustically actuated micro swimmers have been demonstrates using polymer micro structures[23,24]. Spiral filaments attached to a magnetic head as artificial swimmers have also been demonstrated[25]. Magnetically actuated soft robots are also becoming increasingly popular[26,27].

1.2 Motivation – Food safety and microfluidics

Harmful pathogenic bacteria cause a variety of diseases, including food poisoning, which poses a significant public health problem. Because microorganisms readily proliferate over time, the rapid detection of bacteria during the initial stages is highly important to prevent food borne diseases. It is estimated that *Salmonella* bacteria alone causes more than a million illnesses in humans every year. With a total of 50 million annual cases of bacteria related illnesses, of which around 3000 of them result in death[28]. It is known that bacteria in concentrations as low as 10-100 CFU/ml are capable of causing harm[29–31]. Microbiologists, therefore, are posed with the challenge of finding a needle-in-a-haystack. How does one detect small numbers of pathogens amid large numbers of harmless background in a large and complex sample matrix?

The problem of detection of low concentration of cells is also encountered in medical and pathological analysis. Particularly, the detection of circulating tumor cells (CTCs), in the circulatory system which is associated with cancer metastasis[32–34]. CTCs are

very rare events with an approximate concentration of 1 CTC per 10^5–10^7 blood mononuclear cells, and such rare nature makes it difficult both to detect and isolate them. These cells are usually larger $10\mu m$ in diameter, which makes their isolation and detection relatively easier. Many inertial separation methods have been developed for their isolation which use a body forces (gravity[35], centrifugal[36,37] or magnetic[38–40]) or surface forces[41,42] (dielectrophoretic) to isolate the cells from a mixture. These forces are proportional to the volume or surface area of the cell. These methods usually achieve a high throughput and separation efficiency. The same techniques, however, cannot be used to isolate bacterial cells because of their smaller size. Bacterial cells are usually $\sim 1\mu m$ in diameter, which is 10 times less than the diameter of CTCs, and 1000 times less in volume. Therefore, methods using inertial effects where the isolation efficiency is proportional to the cell volume does not work efficiently for bacterial cells.

The most commonly used detection technique for pathogenic bacteria is the cell culture technique. This technique first enumerates the cells and increases their concentration by plating them and then detecting the cells at higher concentrations.

Although cell culture techniques are widely used to detect pathogenic bacteria, they cannot provide on-site feedback because cultivation requires several days and a laboratory for screening. Over the years, more rapid methods have replaced plating steps with DNA hybridization or enzyme immunoassays. However, even these methods detect at best 10^3-10^4 CFU/g of target pathogens, meaning that culture enrichment steps are still necessary[43]. The protocol starts with an overnight or even longer enrichment phase conducted in liquid broth, in agitated flasks. Then, cultures are plated on Petri-dishes containing agar-based growth medium and incubated for durations that may range from

12 hours to several days before counting. Finally, additional molecular or immunological typing methods may be needed, for specific strain identification. This protocol is highly sensitive and specific, but it typically requires several days, skilled personnel and large volumes of consumables.

Other methods for isolation and detection of bacterial cells therefore need to be developed. Recently, novel detection methods based on functional magnetic nanoparticles have been used for the rapid detection of bacteria. Antibody-functionalized magnetic nanoparticles can capture, separate, and concentrate pathogenic bacteria. Captured bacteria may be detected without cultivation using a variety of analytical techniques, such as quartz crystal microbalance (QCM)[44], surface plasmon resonance (SPR)[45], electrochemical impedance spectroscopy (EIS)[46], surface-enhanced Raman scattering (SERS)[47,48], and fluorescence spectroscopy. These methods, however, have a low throughput and can analyze a small volume of sample. Commercially available Pathatrix® Auto Instrument concentrates pathogens and spoilage organisms from a wide range of food and environmental sample matrices for downstream testing by PCR, immunoassay or culture. This instrument is, however, expensive and required trained personnel to operate.

Researchers often resort to microfluidic approaches to isolate bacterial cells and for bacterial identification, use nucleic acid amplification techniques or further immuno-recognition protocols. Microfluidic systems with high surface to volume ratio pose multiple advantages of small sample volume, small size and low energy consumption[49–51]. Furthermore, larger sample volumes can be handled by designing continuous flow devices with a high throughput. A variety of microfluidic separation methods for bacteria

can be found in the literature. Pereiro et al.[30] have shown a total micro analysis system using magnetic fluidized beds for detection of pathogenic bacteria. They have been able to detect cells which are as low in 100 CFU/ml in a few hours. Kang et al. [52] alternatively proposed a system that combines DNAzymes, microfluidic droplets and 3D optical detection, reaching sensitivities between 10 and 100 CFU/ml, but this method is also prone to false positive results in the case of dead or lysed bacteria. Lee et al.[53] have isolated cells with concentrations as low as $10\,CFU/ml$ using 3D printed helical channels.

There is a need for the development of bacteria isolation/pre-concentration and detection techniques that enable portable, cheap, disposable, reliable and fast detection of pathogenic bacteria. This thesis aims to develop microscopic bio-mimetic artificial cilia that are capable creating local fluid transport, which in turn can capture bacterial cells. The artificial cilia are hair like structures that are micro fabricated and incorporated inside a microfluidic channel. These structures are magnetic and can oscillate to produce a local fluid transport and enhance the fluid mixing. Such cilia can potentially be used to capture and pre-concentrate bacterial cells, which can further be detected by other means such as polymerase chain reaction (PCR).

1.3 Artificial cilia – so far.

Several kinds of artificial ciliary systems have been experimentally demonstrated using electrostatic[54], pneumatic[55], and chemical actuation[56]. Den Toonder et al[54]. demonstrated that electrostatically actuated cilia are promising for microfluidic mixing, although they involve a rather complicated fabrication process with multiple metal and

polymer lithographic steps. Moreover, introduction of electric fields to actuate artificial cilia might limit the use of this approach in applications involving biological samples. Orbay et al.[57] have shown acoustical actuation of polymeric cilia, and demonstrated microfluidic fluid mixing using these structures.

Among the different approaches, magnetic actuation[58–63] is promising due to the relatively simple realization and operation. In this case, magnetic cilia can be actuated from a distance with no interference of the magnetic field with biological samples. Magnetically actuated ciliary systems typically comprise of a magnetic structure that can deform elastically and an external magnetic field that drives the magnetic structure.

Various sophisticated fabrication techniques to realize magnetic cilia such as roll up method, polymers embedded with magnetic particles, and beads self-assembly have been developed and demonstrated. The beads' self-assembly method lacks in control of the properties of cilia. The number of beads in a cilium may vary and the fabrication is rather complicated involving guiding particles into trenches using acousto-optic deflectors. The mechanical properties of polymeric cilia with magnetic particles are difficult to predict as the composition of the polymer and curing temperatures affect the material properties. This method also involves complex chemistry to realize the lithographic step. Permanent magnets and electromagnet setups are used to create alternating magnetic fields for synchronous actuation of ciliary arrays[59,64–66]. In general, an experimental realization of magnetic artificial cilia has not been a trivial task. A detailed review of the different fabrication approaches to fabricate magnetically actuated cilia can be found elsewhere[54].

Owing to the difficulty in realizing artificial cilia experimentally, researchers often resort to computational studies. Theory and computational models to understand the dynamics of magnetic artificial cilia and demonstrate their ability to pump fluids[67] have been developed. Two and three dimensional models are used to examine the kinematics of a metallic film cilium actuated by a rotating magnetic filed[68 69]. The net flow generated by magnetically-actuated cilia in the relation to the beating pattern and the Reynolds number is analysed[70]. A linear relation is reported between the area swept by the cilium tip and the fluid flow per cycle. Khaderi and Onck[69] have examined the effects of multiple cilia that interact in an array and discuss the effects of metachronal waves. The use of such cilia for micro-particle capture[12,14–16], particle transport[71], flow control[72] have been examined using computational modeling.

In this thesis, a simple and easy to implement fabrication and actuation mechanism for realizing magnetic artificial cilia is detailed. A surface micro-machining technique is detailed to fabricate microscale magnetic cilia and study their operating mechanism the creation of fluid transport when actuated by a rotating permanent magnet. The fabrication process results in soft magnetic filaments made of nickel-iron alloy, which has a high magnetic susceptibility, ensuring high magnetic forcing. Furthermore, the fabrication process is simple and employs standardized protocols of lithography and metal deposition. The process yields highly reproducible cilia of various shapes and sizes. Furthermore, the kinematics of the asymmetric beating, fluid pumping characteristics, metachronal motion, and particle capture capabilities of magnetic artificial cilia are discussed in detail.

1.4 Organization of the thesis

The fabrication process to realize the artificial cilia is first detailed in **Chapter 2**. The actuation mechanism using a simple rotating permanent magnet is described, and fluid transport by an array of cilia is demonstrated.

The kinematics of oscillation of an individual cilium is characterized in detail **Chapter 3**. The asymmetric beating pattern is directly imaged, and its mechanism is explained. The kinematics of beating are shown to depend only on governing non-dimensional parameters (magnetic number and sperm number). Differences in the beating pattern for clockwise and counterclockwise rotating field is described.

In **Chapter 4**, the fluid transport characteristics of arrays of artificial cilia is quantified. Record flow rate with a maximum upto 1.4mm/s are obtained in such ciliary systems. Distinction between flow rates produced due to clockwise and counter-clockwise rotation of the magnetic field are detailed.

Array of artificial cilia can be actuated in a sequential metachronal fashion. Such motion often observed in biological cilia is known to enhance the fluid transport characteristics. Multiple methods to create metachronal motion in artificial ciliary arrays is detailed in **Chapter 5**.

Artificial magnetic cilia are usually actuated by a uniform magnetic field across all the cilia in the array. This kind of actuation leads to all the cilia oscillating simultaneously. Individual control of such cilia can be achieved by combining the magnetic actuation with electrostatic actuation. Details of combined magnetic and electrostatic actuation are detailed in **Chapter 6**.

Revisiting the primary motivation for developing the magnetic cilia for capturing and isolating cells in low concentration samples, particle capture capabilities of artificial cilia are described in **Chapter 7**. Demonstration of *Salmonella* capture on the ciliary surface is detailed.

Conclusions and scope for future work is detailed in the **Chapter 8**.

Chapter 2. FABRICATION AND ACTUATION OF ARTIFICIAL CILIA

As discussed in INTRODUCTIONChapter 1, achieving fluid transport at the micrometer length scales is difficult owing to the lack of inertial effects[2,3]. A mere symmetrically reciprocating motion is not sufficient to produce any net fluid transport[3]. Microorganisms and cells that usually operate in these inertia-less regimes have evolved to use cilia and flagella with complex beating patterns to yield a net fluid transport[4–6]. Such complex beating cilia and flagella are imperative to the organism in performing vital biophysical functions.

The development of synthetic cilia that can perform similar non-reciprocal, spatially asymmetric beating pattern could prove useful for fluid and particle transport in lab-on-a-chip and bio-MEMS devices[12–16]. The primary objective of this work is the development of artificial magnetic cilia capable of achieving microfluidic transport. Fabricating arrays of artificial cilia has advantages in controlling the fluid flow produced for various applications that require the metering, mixing or pumping very small volumes of fluids. In this chapter, a surface micromachining process for creating artificial cilia is described. The cilia are made of a magnetic material such that they can be actuated by an external oscillating magnetic field. The idea is similar to the ones described by Fahrni et al.[64] and Belardi et al.[73], where polymer filaments embedded with magnetic material is used as cilia. The thin filaments are anchored on one end to the substrate and can then be forced using an oscillating external magnet.

Magnetic thin films deposited using physical vapor deposition - PVD process to fabricate the cilia is described in this chapter. Nickel-Iron permalloy (80% Ni and 20% Fe) is used to make the filaments. The high magnetic permeability of NiFe allows for maximum magnetic forces to act on the filament. NiFe is a soft magnetic material that gets magnetized in the presence of an external magnetic field and has negligible coercivity which ensures minimum remnant magnetization. Therefore, the same forcing can be applied over multiple cycles of oscillations as the filament re-magnetize easily in a time varying field. Furthermore, the high deformability of magnetic filaments allows for large deflections under the magnetic forcing.

2.1 Microfabrication of cilia

Microscopic borosilicate glass slides (MS400, Lab storage, St. Louis MO) are used as the substrate to fabricate the cilia. The glass slides are inexpensive and easily disposable. Moreover, because they are transparent, it can be used to visualize the motion of the cilia and fluid around it. Surface micromachining techniques are employed to fabricate cilia on the glass substrate and the process involves a simple two-mask lithographic process. Before beginning the fabrication, the glass slides are cleaned by washing them in acetone, followed by isopropanol, and dried using a nitrogen air gun. A flow chart that indicates the steps of fabrication is shown in Figure 2-1. First, the pattern of the cilia is imprinted using a negative photoresist (NR9 1500Py Futurex) on a glass substrate. The details of the first lithographic step are detailed Table 1. A 40nm sacrificial layer of copper is then sputtered (Unifilm sputterer) followed by a layer of NiFe (80:20 Ni:Fe permalloy) of required thickness (at a rate of $200\,\mathring{A}/min$). Lift-off is done to

remove the photoresist by dissolving it in acetone, which leaves the cilia features on the surface.

The next step is to deposit an anchor for holding the cilia on the substrate. A second lithographic step (

Table 2) is performed to obtain these features which are deposited with 150*nm* of titanium (at a rate of $350\,\text{Å}/min$). This anchor layer sticks to the glass and ensures the NiFe cilia are held on the substrate. The cilia are released by removing the sacrificial copper layer by dissolving it in 5% ammonium hydroxide, which selectively etches the copper.

The stresses due to sputtering NiFe alloy curls the film away from the substrate when the supporting Cu layer is removed. This leaves a free standing magnetic NiFe film that can be actuated by an external magnetic field. The yield of this process is high, with over 99% of cilia functioning properly. This process is simple and highly reproducible. Moreover, the fabricated devices can be stored for extended periods, and the sacrificial layer can be removed during the time of the experiment. The dimensions of the cilia are readily modified by changing the lithographic mask and NiFe film deposition conditions.

Once the sacrificial layer is removed and the filament is suspended in DI water, care should be taken to ensure that the filaments remain in a suspended state and do not dry out. If the fluid evaporates, the filaments comes in contact with the substrate and adheres to it via hydrogen bonding. Such sticking is observed to be strong and cannot be reversed. This leads to irreversible damage of the cilia. One way to overcome this issue is to suspend the filaments in a salty buffer solution. On drying, the salt crystalizes beneath

the surface of the filaments, thereby avoiding a direct contact between the surface of the filament and glass substrate. On adding water to re-suspend the filaments in such a case will ensure their proper functioning.

Table 1: Conditions used for the first step in fabricating magnetic cilia.

Spin coating	NR9 – 1500PY, 3000RPM, 5s ramp, 30s
Soft bake	120s at $150\,^{o}C$
Exposure	$190\,mJ/cm^{2}$
Post Exposure Bake	60s at $100\,^{o}C$
Development	15s in RD6 developer

Table 2: Conditions used for the second step in fabricating magnetic cilia.

Spin coating	SC1827, 3000RPM, 5s ramp, 30s
Soft bake	120s at $120\,^{o}C$
Exposure	$150\,mJ/cm^{2}$
Post Exposure Bake	Not required
Development	30s in MF319 developer

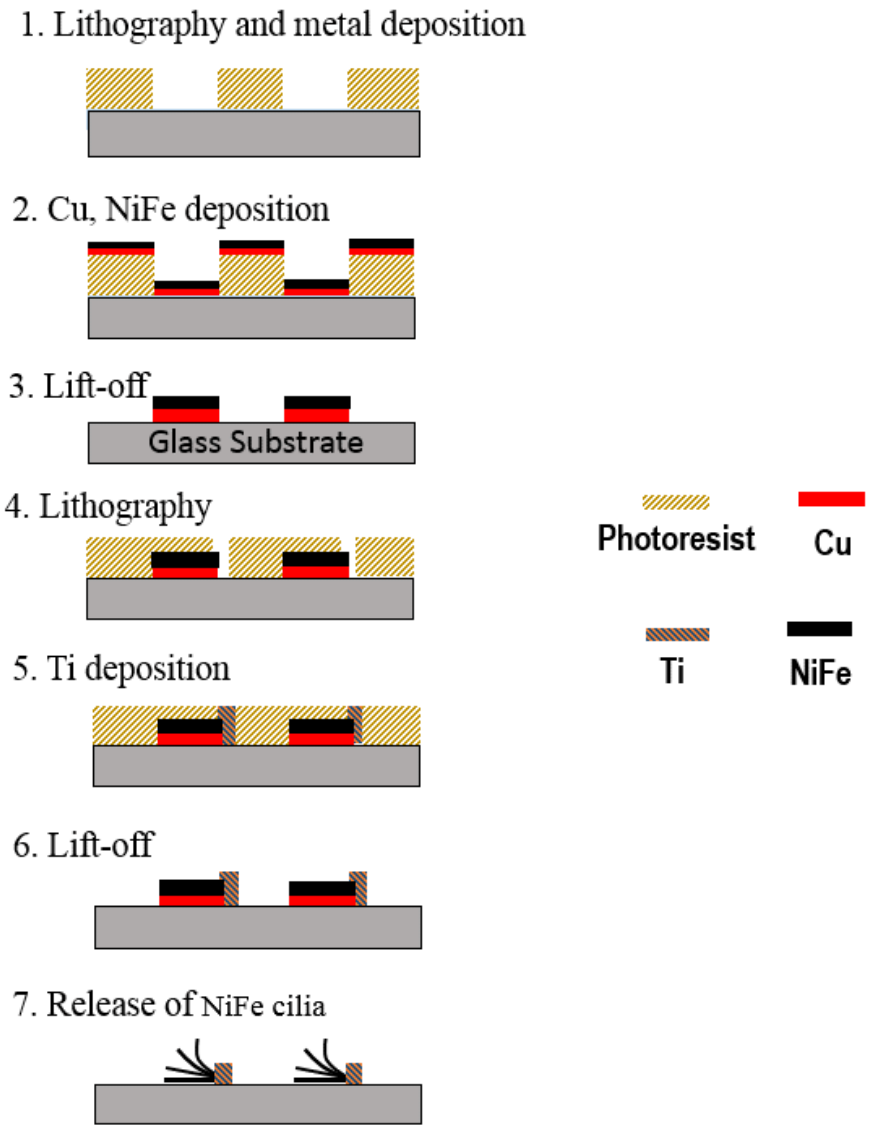

Figure 2-1: Flowchart of the fabrication process showing the two steps-deposition of copper followed by NiFe layer, and titanium anchor layer.

2.2 Characterization of magnetic thin films

Multiple parameters affect the behavior of the magnetic film including the geometry, composition and the stress in the filament. The initial orientation of the filament when the sacrificial layer is removed is determined by the stress in the NiFe layer. When the sacrificial layer is removed, the stresses in the NiFe deposited layer curl the filament away from the substrate. An SEM image of a super critically dried array of cilia is shown in Figure 2-2. Notice that the filaments curl away from the substrate. The curvature of the curled filament can be controlled by changing the metal residual stress, which in turn can be controlled by varying the deposition conditions. For example, evaporating NiFe results in a highly stressed filament which has a high curvature when the sacrificial layer is removed. Similarly, if the NiFe layer is sputtered which is a relatively low stress process, the stress in the filament is lower. Furthermore, it is noted that the filaments had least stress and minimum curvature when the copper and NiFe layers are deposited at 200A/min. All the cilia described in the rest of the thesis are fabricated using this deposition condition. It is also noted that the deposition conditions such as the sputter chamber pressure also affects the film quality and stress.

While the deposition condition and deposition rate determine the film's initial curvature, the parameters that determines the deformability of the cilia is the geometry and the magnetic properties. Thickness of the filaments determines the ability of fabricated filaments to follow the field. As thickness increases, the bending rigidity increases, and the deformation reduces. The thickness of cilia used in the various experiments ranges from 20nm to 120nm, as measured using Dektak profilometer.

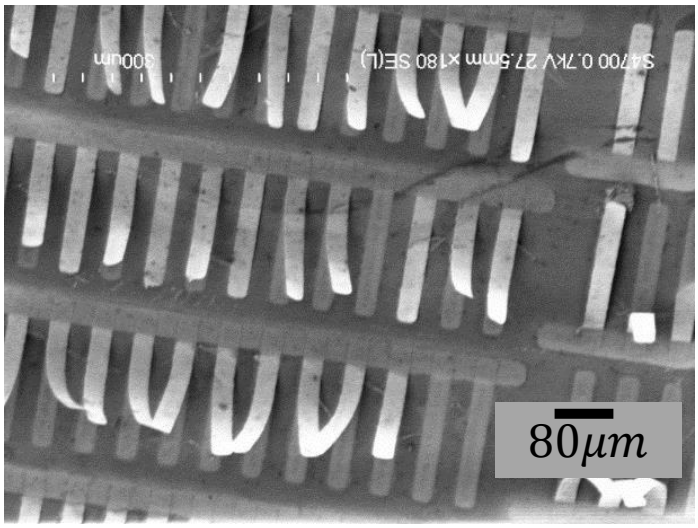

Figure 2-2: SEM image of super critically dried cilia.

2.2.1 Measuring the composition

The composition of NiFe determines the magnetic properties of the filaments. The NiFe sputtering target is obtained from Kurt Lesker company and has a composition of 80% Ni and 20% Fe. This composition is known to yield the maximum magnetic susceptibility and it is therefore important to ensure that this ratio of 80:20 of Ni to Fe is retained in the sputtered filaments. Figure 2-3a, b shows the composition of Ni and Fe present in the filament. Figure 2-3c shows the combined composition of Ni and Fe. Notice that the uniform distribution of Ni and Fe throughout the filament. Figure 2-3d. Shows the energy dispersion spectroscopy results revealing the composition of the filaments. The measured film composition is found to be very close to that of the sputtering target with a ratio of 80:20 nickel to iron.

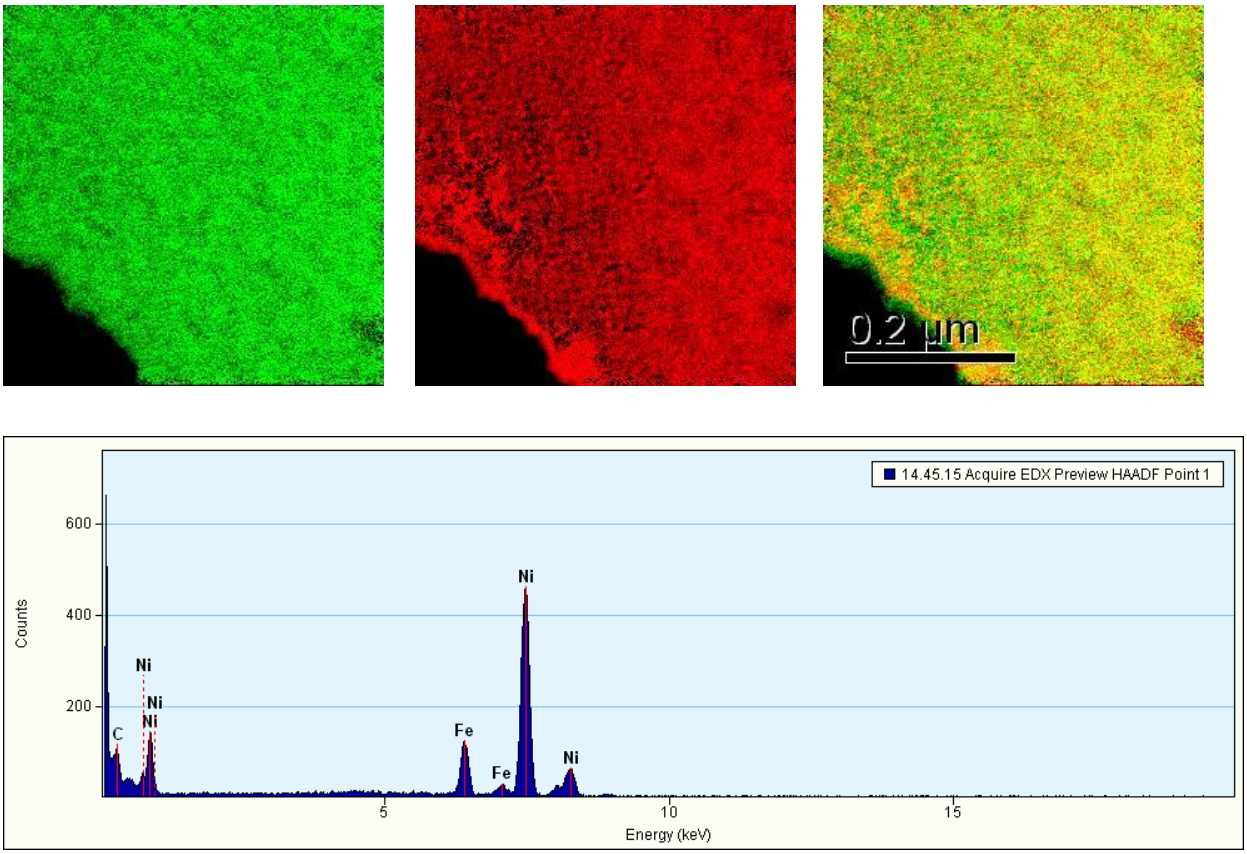

Figure 2-3: TEM dispersion spectroscopy images of the filament. **a**) Distribution of nickel in the filament. **b**) Distribution of iron in the filament. **c**) Combined distribution of Ni and Fe. **d**) Energy dispersion spectroscopy results of the filament revealing the composition.

2.2.2 Stress in the free standing thin film

In the experiments, it is noted that the deposition rate of copper sacrificial layer is as important as the deposition of NiFe to determine the residual stress. This is perhaps due to the matching of the grain sizes in the two metal layers. On the Unifilm sputterer, the deposition rate is set to $200\,\mathring{A}/min$ for the deposition of both Cu and NiFe layers. A

large deviation from this rate (more than $\pm 100 \, \text{Å}/min$) results in various defects in the fabricated filaments. A large deviation in the deposition rates leads to high film stress[74] that results in filaments that fracture or have an oblique orientation after the sacrificial layer is released. Figure 2-4a, b. shows the breaking of filaments and the oblique orientation in highly stressed filaments. For certain deposition conditions, the residual stress is just right for the filaments to curl into full circles. Examples of such circled filaments are shown in Figure 2-4c, d. Quantifying the causes leading to stresses in the free standing NiFe layer is important. However, this was not within the scope of this thesis.

It is also important to ensure that the cilia are properly anchored to the substrate. Poor adhesion of the titanium layer to the substrate can result in cilia being detached. Figure 2-4e shows an example where some cilia are detached from the substrate.

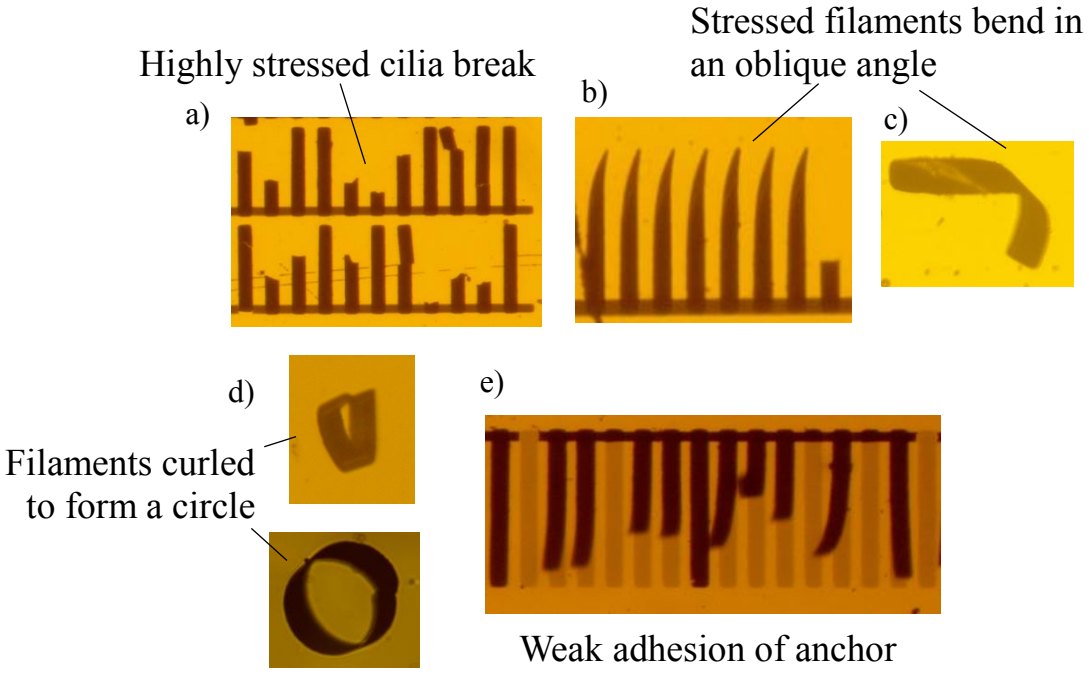

Figure 2-4: Various defects in the filaments due to residual stress in the NiFe layer.

To measure the surface roughness and grain size, TEM images of the free standing NiFe layer is taken. In Figure 2-5a the surface roughness of the filament is shown. Figure 2-5b shows the selected area electron diffraction (SAED) of the NiFe thin film. The bright rings indicate the crystalline structure in the filament. Figure 2-5c shows the grain size in the NiFe layer. The bright regions represent a crystallographic grain in the layer. The estimated average grain size is $\sim 30nm$ as measured using ImageJ distance measurement tool.

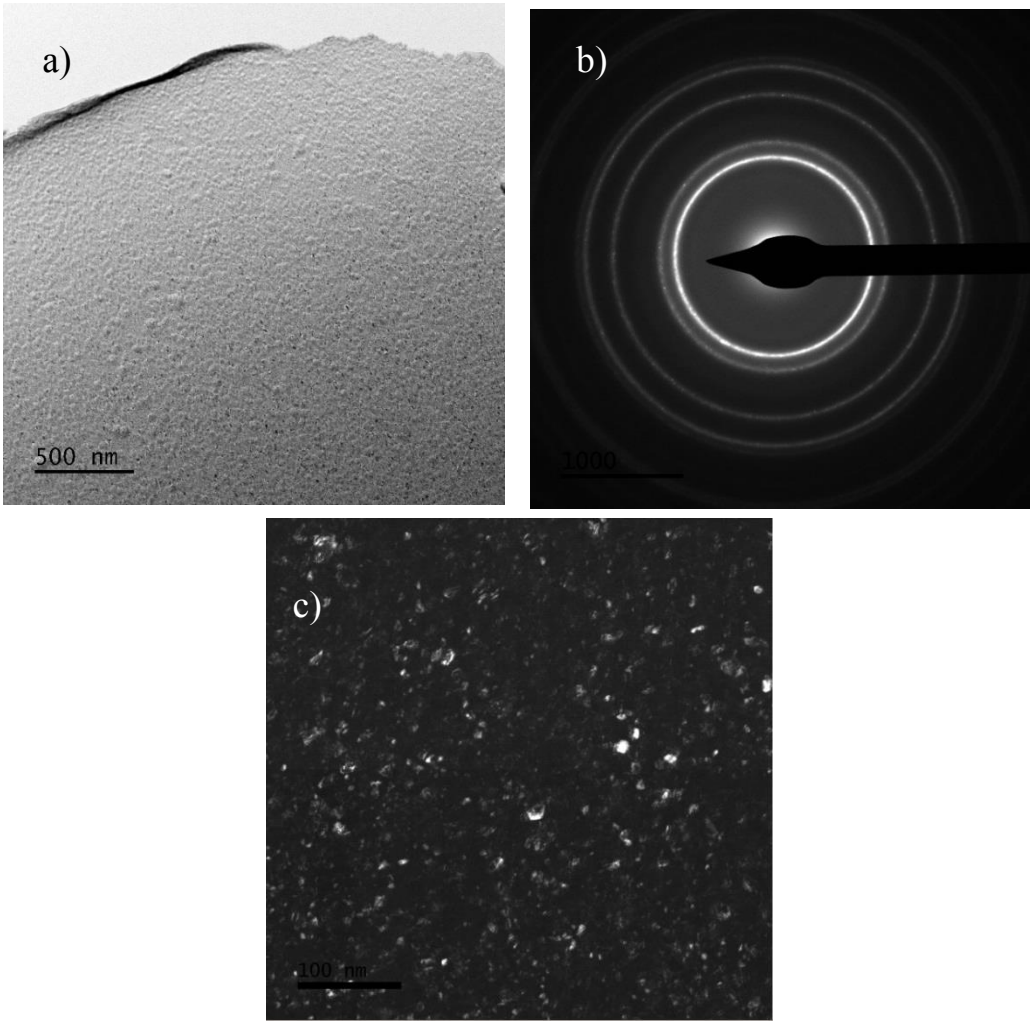

Figure 2-5:**a**) TEM images of the NiFe layer showing the surface roughness. **b**) Selected area electron diffraction (SAED) image of the NiFe thin film showing the cryptographic structure. **c**) grain size analysis of the NiFe layer.

2.3 Soft lithography – Fabricating PDMS channels

Standard techniques, of photolithography and soft-lithography, are used to fabricate microchannel. First, Su8 photoresist (MicroChem Corp) is coated on a silicon wafer. A spin coater (SCP spin coater) is used to coat a uniform thin layer of photoresist. After the resist is soft baked and cooled, it's exposed to UV light in a mask aligner through a photomask on which the image of the channel is drawn. A 2-dimensional latent image is formed on the resist. When the UV light is passed through a mask, the opaque pattern blocks the light and the clear regions allow the light beam to pass through, thus enabling a transfer of pattern on photoresist. It is later developed in a developer solution to form a 3-dimensional master mold of the image.

Channels are made using poly (Dimethylsiloxane) (PDMS) by the standard process of soft lithography. This is done by mixing 10 to 1 ratio of the elastomer and hardener and curing at $80^{o}C$ for 3 hours. These PDMS replicas are then peeled off from the silicon substrate and bonded to glass slides. This bonding is done by first treating the surface of PDMS and glass in an oxygen plasma for 1 minute, and then pressing them together to bond permanently. Reservoirs are dug into the PDMS micro channels before they are bonded to the glass slide, using a mechanical punch. Figure 2-6 shows the flow chart of the soft lithography procedure used.

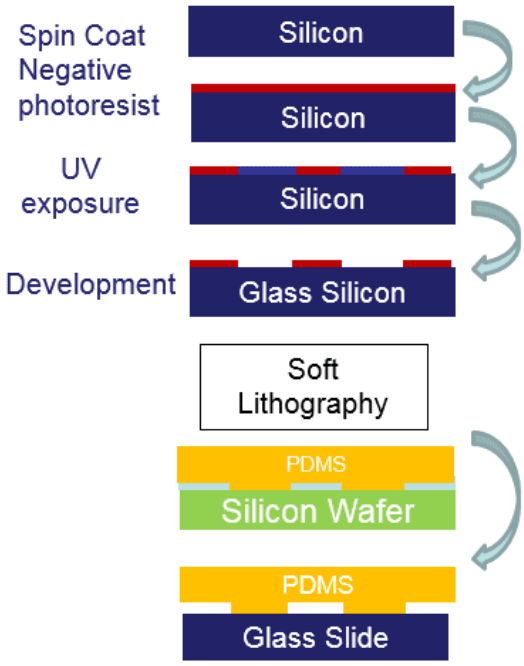

Figure 2-6: Flowchart for fabricating the PDMS devices. The Su8 mold is first made on Silicon wafer. PDMS channel replicas are then made using the mold. The PDMS channels are plasma bonded on glass devices.

2.4 Actuation of the filaments

The fabricated NiFe filaments can be subjected to a simple oscillating magnetic field, which the cilia follow. For example, a simply rotating magnetic field can be used to actuate the cilia. This is discussed in more detail in chapter 3. To ensure a uniform magnetic field over a cilium, it is important that the size of the magnet be much larger than the size of the filament. In all the experiments presented in this thesis, magnets larger than 2 *inches* in diameter are used. This is much larger than the size of the filaments. However, the size of a ciliary array can be large and magnetic field acting on the different parts of the array could be different (as explained in Chapter 4).

The general setup to actuate the array of cilia is shown in Figure 2-7a and a photograph of the experimental setup is shown in Figure 2-7b. A cylindrical magnet that is magnetized through its diameter is connected to the shaft of a motor and spun. The axis of rotation lies parallel to the plane of the substrate. As the magnet rotates, the magnetic cilia orient themselves in the direction of the magnetic field leading to their cyclic oscillations. Figure 2-7c, d, e, f shows a ciliary array at different rotational positions of the actuating permanent magnet. These images are recorded from beneath the substrate as indicated in Figure 2-7a and show that all the cilia oscillate synchronously throughout the beating pattern. Notice the large deformation of the cilia, as indicated by the projection of the deformed filament. Therefore, a simply rotating magnetic field can oscillate the cilia and produce large deformations in its motion.

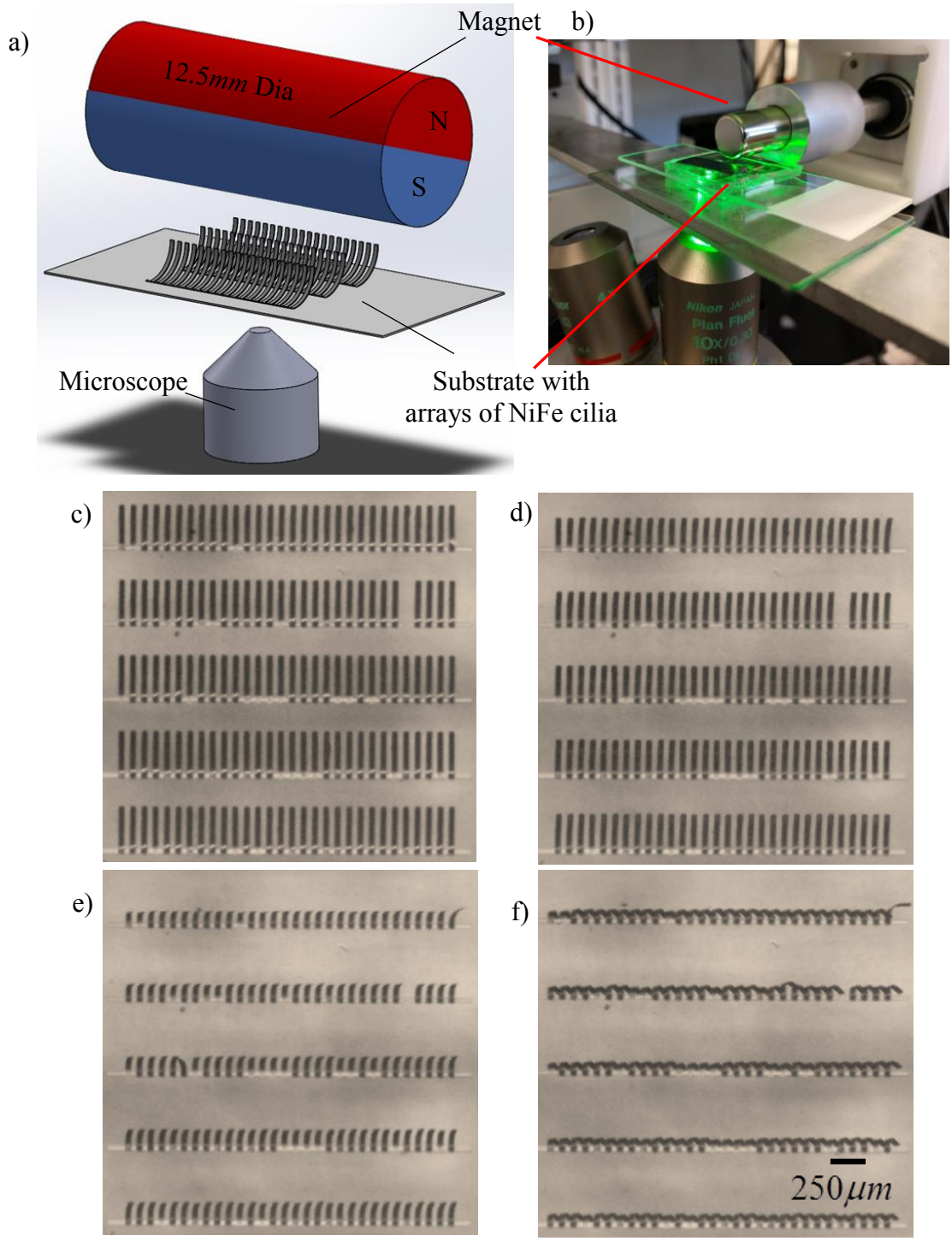

Figure 2-7: **a)** Schematic of the experimental setup showing the actuation of an array of cilia using a permanent rotating magnet. **b**, **c**, **d**, **e)**: Series of experimental images of an array of cilia actuated by a rotating magnet, as viewed from the bottom. **b)** Position of cilia when the magnetic field is horizontal, and cilia are relaxed. **c)**, **d)** Changing

positions of the cilia as the magnetic field is being rotated from the horizontal to the vertical direction. **e)** Position of cilia when the field is normal to the substrate.

2.5 Fluid transport by arrays of cilia

Next, to probe whether the oscillating magnetic cilia can produce a net fluid flow, experiments are conducted in which flow patterns around beating cilia are visualized using fluorescent microparticles. The fluid is seeded with micrometer-sized fluorescent particles (1μm FluoSpheres™ - F13080, Thermofisher Scientific, USA) and their motion is registered using a standard epifluorescence microscope (Nikon - Eclipse Ti) while the array of cilia is subject to a rotating magnetic field. Figure 2-8 shows a snapshot of a fluid flow pattern produced by a ciliary array, where the trajectories of the fluorescent particles indicate fluid transport. In this experiment, cilia are arranged in four columns with four rows of cilia. Each row contains 15 individual cilia. The cilia in the successive columns are anchored at opposite edges. This results in cilia that face opposite directions in the four columns, as indicated by the arrows. The columns of cilia pump fluid in the direction of the arrows, that result in a circulatory flow pattern shown by the streak lines generated by the fluorescent particles.

The dimensions of each individual cilium in the array are $200\mu m \times 20\mu m \times 70nm$, and the actuation frequency in this experiment is $50Hz$. These experimental conditions lead to a Reynolds number, $Re = \rho LWf/\mu \approx 0.1$, that represents the ratio of inertial forces to viscous forces that act on the cilia. Here, ρ is the fluid density, L is the length, W is the width, f is the frequency and μ is the dynamic viscosity. For such values of

Reynolds number, inertial effects are negligible and a time irreversible motion with a spatial asymmetry of the beating pattern is required to create a net fluid transport[58] (As discussed in Section 1.1). Thus, the result in Figure 2-8 indicates that magnetic cilia is able to generate a time irreversible motion that leads to a net fluid flow. In the next chapter, the beating kinematics of individual magnetic cilium to understand the mechanism leading to fluid transport is explored.

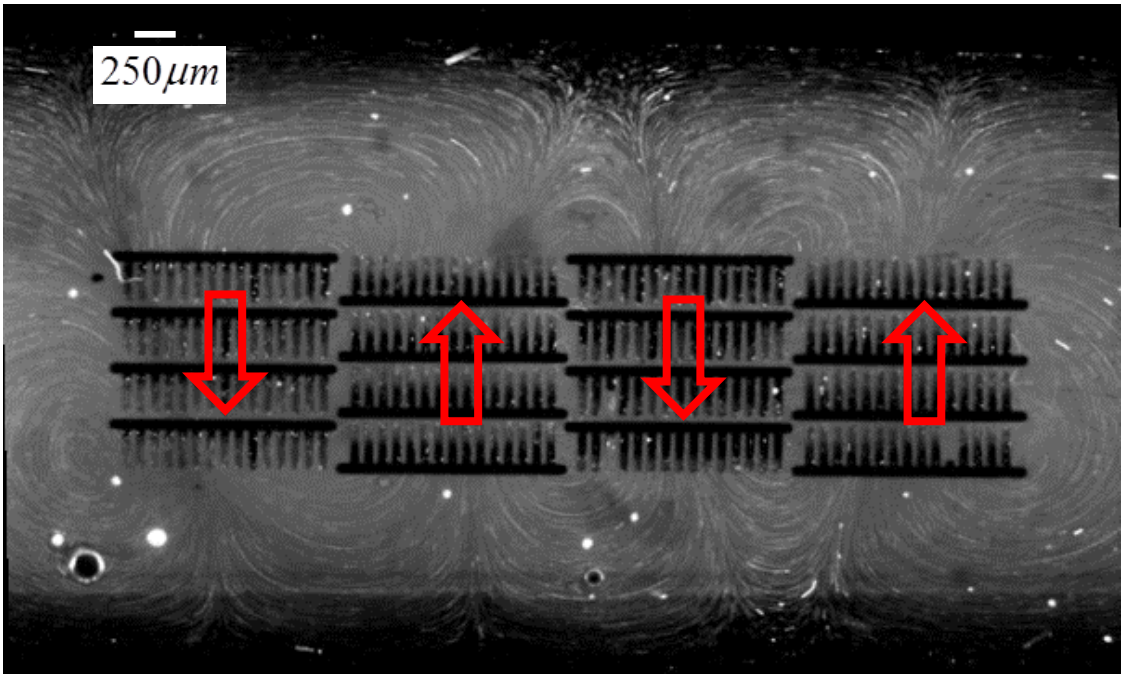

Figure 2-8: Fluid circulation produced by an array of magnetic cilia. The four columns of cilia are anchored on the opposite ends producing fluid pumping in the directions shown by the arrows. This leads to the fluid circulations as shown by the streaklines. Cilium dimensions are $200\mu m \times 20\mu m \times 70nm$ and the actuation frequency is $50Hz$. (See Video 1)

2.6 Summary

A simple fabrication method to create magnetic artificial cilia is developed. The cilia are prepared using a two-step lithographic process by releasing a thin permalloy stripe, anchored at one end to the substrate. The filaments are characterized using thickness, composition and grain size analysis. The resulting cilia are magnetic filaments that can be actuated by an externally varying magnetic field. Furthermore, an array of cilia is shown to produce considerable fluid flow in low Reynolds number environments, implying an asymmetric beating pattern. The asymmetry in the beating pattern is discussed in more detail in chapter 3.

The method discussed in this chapter involves standardized steps for thin-film microfabrication that enables fabrication of elastic cilia with a wider range of parameters, high degree of accuracy, and reproducibility. Thus, can be readily adapted for the applications in lab-on-a-chip devices and can be especially useful in various biomedical assays to handle biological samples using low magnetic fields that are typically harmless. The fabrication approach allows us to readily create extended arrays of multiple simultaneously beating cilia, including heterogeneous arrays of cilia with different geometries.

Chapter 3. KINEMATICS OF BEATING MAGNETIC CILIA

As explained in Chapter 2, a mere reciprocating, back and forth motion of cilia is insufficient to create a net fluid transport. However, as demonstrated in Chapter 2, the fabricated magnetic cilia show a net fluid transport when actuated. The ability of an array of magnetic cilia to produce fluid circulation must be related to time-irreversible, spatially asymmetric oscillations.

In this chapter, the kinematics of beating of an individual cilium is investigated. The mechanism of their beating in a time-irreversible and spatially asymmetric fashion is detailed. The cilium motion is defined by an interplay among elastic, magnetic, and viscous forces. This difference in dominating forces that act during the forward stroke and the recovery stroke leads to an asymmetric beating pattern of the cilium. Experiments are performed on a single cilium and its beating pattern is directly recorded by imaging the stroke pattern. Furthermore, computer simulations are performed to validate the understanding of the kinematics and reproduce similar beating.

The relative importance of magnetic, elastic, and viscous forces in terms of dimensionless magnetic (*Mn*) and sperm numbers (*Sp*) is characterized. The dependence of cilium kinematics on these dimensionless parameters is demonstrated experimentally. The cilium oscillations are promising for creating spatially asymmetric motion required to induce fluid pumping and other transport processes in a low Reynolds number environment. Note that the fabrication approach allows us to readily create extended arrays of multiple simultaneously beating cilia, including heterogeneous arrays of cilia with different geometries.

3.1 Introduction

Researchers have developed theory and computational models to understand the dynamics of magnetic artificial cilia and demonstrate their ability to pump fluids[67]. Two and three dimensional models are used to examine the kinematics of a metallic film cilium actuated by a rotating magnetic filed[68 69]. The net flow generated by magnetically-actuated cilia in relation to the beating pattern and the Reynolds number is analysed[70]. A linear relation is reported between the area swept by the cilium tip and the fluid flow per cycle. Khaderi and Onck[69] have examined the effects of multiple cilia interacting in an array and discussed the effects of metachronal waves. The use of such cilia for micro-particle capture[12,14–16], particle transport[71], flow control[72] has been examined using computational modeling.

In this chapter, it is shown that using a rotating permanent magnet, the magnetic cilia can be driven to oscillate with highly asymmetric strokes, resembling the beating of biological cilia. The asymmetric motion opens the possibility of harnessing such synthetic cilia for fluid pumping and other fluid manipulations. The magnetically-oscillated artificial cilia can be utilized for various microfluidic purposes due to the ease of fabrication and actuation. It is, therefore, important to understand the kinematics of such cilia under different magnetic forcing conditions. Although, researchers have studied the mechanisms of fluid manipulation in similar systems[60,75], experimental studies characterizing the asymmetric beating cilia are still limited[64]. Here, both experiments and theory are combined to understand the kinematics of magnetically driven thin film cilia for a range of actuation conditions. A setup with a rotating permanent magnet and visualize motion of a cilium in this plane of oscillation for a range

of actuation conditions is used and a computational model for fluid-structure interactions to validate and further examine cilium motion due to a rotating magnetic field is employed. The key parameters governing cilium motion and identify actuation regimes enhancing asymmetry of cilium beating are established.

3.2 Experimental and computational methodology

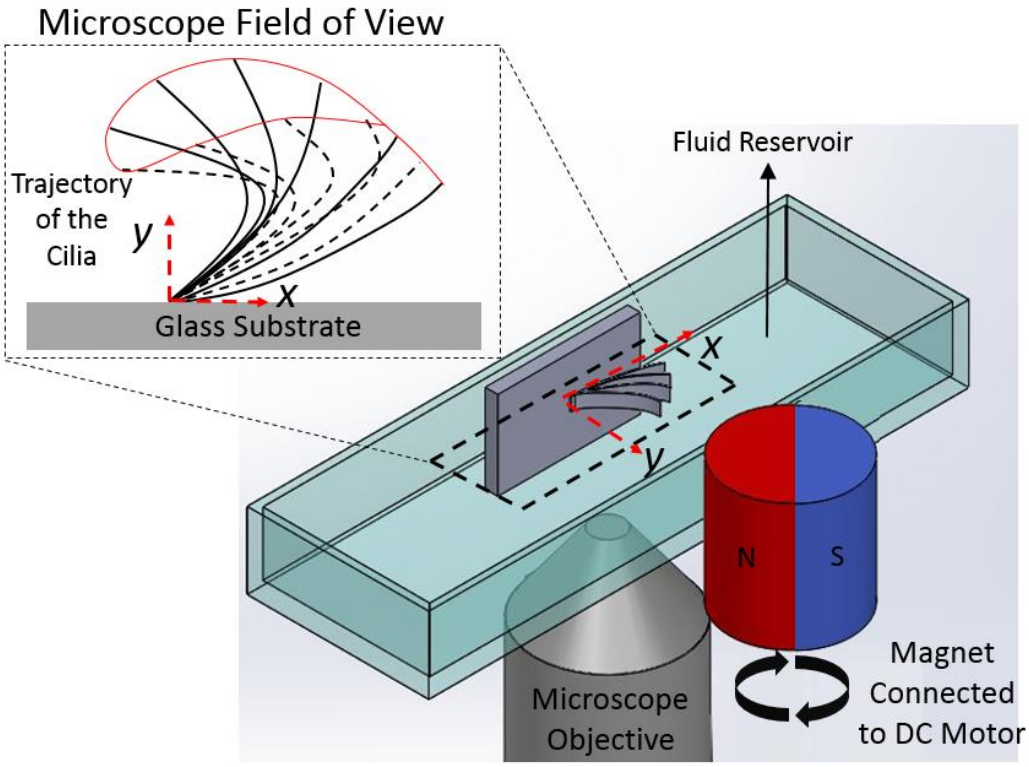

Figure 3-1**:** Schematic of the experimental setup showing the relative positioning of the cilium on the microscope with respect to the magnet. Note the cilium oscillation plane ($x-y$) is captured by the microscope.

3.2.1 Experiments

Analysis of the motion of cilia from the top view[64] does not reveal all of the important features of their motion. To better capture the cyclic motion of the cilium, the cilium in its plane of oscillations is imaged. To this end, the substrate vertically on an inverted microscope (Nikon Eclipse Ti) such that the plane of oscillations of the cilium is parallel to the microscope plane of view, $x-y$ (Figure 3-1) is placed. The cilium is actuated using a cylindrical magnet, magnetized through its diameter ($12mm$ diameter, D8X0DIA, KJ Magnetics)). The magnet rotates with its axis perpendicular to the plane of view. Since the size of the magnet ($12mm$ in diameter) is much larger than the length of the cilium ($\sim 500\mu m$), the magnetic field experienced is nearly uniform, i.e. the cilium experiences a uniform magnetic field that rotates in time. To capture bright-field images of the cilium motion, a high-speed camera (Phantom Miro C110, Vision research) that is operated at 800 frames per second rate is used. TIFF image stack obtained by the camera is transferred to the completer for analysis.

Trajectories of cilium oscillations are captured under varied experimental conditions. In these experiments, the rotation rate of the magnet, magnetic flux density, cilium length, cilium thickness, and fluid viscosity are all varied. The magnet rotates in counter-clockwise (CCW) direction with frequencies f ranging from 1 to 24 Hz. The magnetic flux density is varied by changing the distance between the magnet and cilium, and measured using a gauss meter (Alpha labs, model 1140), with an average reading error of $\pm 20Gauss$. Water ($\mu = 1cP$), iso-propyl alcohol ($\mu = 2.1cP$), and a 2:1 mixture of water and glycerol ($\mu = 4cP$) are used in the experiments. Two thicknesses (

$P = 56 \pm 1nm$, $68 \pm 1nm$), and two lengths ($L = 480\mu m, 430\mu m$) of the cilium are examined. Cilium width *W* is kept constant and equal to $10\mu m$. The modulus of NiFe is estimated to be $200GPa$ [76]. For these experimental conditions, the Reynolds number $\mathrm{Re} = \rho LWf/\mu$ does not exceed 0.12.

3.2.2 Approximation of the magnetic force:

To model the magnetic forces that act on the cilium, it is assumed that the entire cilium is exposed to a uniform magnetic field. This assumption can be validated based on the fact that the size of the magnet is much larger than the cilium length. If magnetic field Ho is applied on the soft magnetic cilium, it induces a magnetization M. Here, **B** and ***M*** are given by

$$\mathbf{B} = (B_{x0}, B_{y0})$$

$$(M_x, M_y) = (\chi_x \frac{B_{x0}}{1 + \chi_x \alpha}, \chi_y \frac{B_{y0}}{1 + \chi_y \beta})$$

Where, $\alpha = 2tan^{-1}(h/L)$, $\beta = 2tan^{-1}(L/h)/\pi \sim 1$

Furthermore, the magnetic couple acting on a filament with magnetization ***M*** and exposed to field **B** is given by their cross product.

$$\boldsymbol{N} = \boldsymbol{M} \times \mathbf{B}$$

On expanding,

$$N_z = \frac{\mu_0 B_0^2 sin2\theta \, (\chi_x - \chi_y + \chi_x \chi_y (\beta - \alpha))}{1 + \alpha\beta\chi_x\chi_y + \alpha\chi_x + \beta\chi_y}$$

Further, assuming that NiFe permalloy is an isotropic magnetic material ($\chi_x = \chi_y = \chi$), and a high geometric asymmetry. ($P \ll L$), the above equation reduces to

$$N_z = \frac{\mu_0 \chi B_0^2 sin(2\theta)}{2}$$

The important thing to note in this equation is that the magnetic moment along the cilium is proportional to $N_z \sim \sin(2\theta)$, where θ is the angle between magnetic field **B** and the local axis is applied.[54,60–63,77]. In the presented model, a distributed moment that acts on the elastic cilium with its magnitude proportional to $\sin(2\theta)$ is imposed.

3.2.3 COMSOL Model

Two-dimensional computer simulations to understand the kinematics of a single cilium are used. The fluid-structure interaction simulations are performed using COMSOL with an arbitrary Lagrangian-Eulerian (ALE) method[78]. A distributed moment that acts on the elastic cilium with its magnitude proportional to $\sin(2\theta)$ is imposed. The magnitude of the moment is set to match cilium deflection observed in the experiment, and the fluid far from the cilium is assumed to be stationary. Results from the simulations are compared against the beating kinematics of a single isolated cilium. More details on the model setup and meshing can be found in APPENDIX A.

3.3 Results and discussion

Microscale magnetic cilia that oscillate in fluid, experience forces due to the rotating magnetic field, cilium elasticity, and the viscous fluid. To better understand the effect of these forces on an oscillating cilium, an elastic soft magnetic filament subjected

to a uniform magnetic field is first considered. Under the action of **B**, the filament magnetizes and experiences a net moment due to this induced magnetization. This moment acts to align the poles on the filament with the direction of the field, so as to minimize its potential energy. When the filament axis is aligned with **B** (or –**B**), its magnetization is aligned with –**B** (or **B**) and the filament experiences no magnetic moment, and allows it to remain at rest in alignment with the field.

When the filament axis is misaligned with the direction of the magnetic field, the filament experiences a distributed magnetic moment, locally proportional to $\sin(2\theta)$, where θ is the angle between magnetic field **B** and the local filament axis. This local magnetic moment drives the filament to align with the direction of **B**. Due to the filament's ability to change its magnetization such that it aligns with either **B** or –**B**, the magnetic moment is maximum at θ equal to $45°$, and is equal to zero when $\theta = 0°$ or $\theta = 90°$. In other words, a stationary cilium experiences a maximum magnetic force four times for every rotation of the magnetic field.

When the magnetic field rotates, it induces magnetic moments such that a free-standing filament rotates following the field rotation. If one end of the filament is anchored, the anchored portion is unable to follow the magnetic field, while the free end tends to align with the field driven by the magnetic moments. This results in bending of the elastic filament. The arising internal elastic forces act to restore the filament's initial (un-deformed) shape. Furthermore, if the filament is submerged in a viscous fluid, it also experiences a viscous force when it moves. The viscous force is proportional to the filament velocity and acts to dissipate its movement. In this limit of a low Reynolds number ($Re \ll 1$), the inertial forces can be neglected. Thus, the dynamic behavior of an

anchored elastic magnetic filament in a viscous fluid subjected to a rotating magnetic field is determined by a balance of magnetic, elastic, and viscous forces.

The soft magnetic cilia get magnetized in the presence of an external magnetic field and tend to align along the direction of the field. this actuates the cilia by subjecting it to a magnetic field rotated in the *x-y* plane as shown in Figure 3-1. The magnetic field is rotated either in the clockwise (CW) or in the counter clockwise (CCW) direction. The change of the direction of magnet rotation results in significantly different beating patterns as shown Figure 3-2 and in Figure 3-4 that present the side view images of cilia collected during CCW and CW magnet rotation, respectively. In the following sections, the cilia are observed beating due to CCW and CW magnet rotation.

3.3.1 Counter-clockwise rotation of magnetic field

Magnetic cilia follow spatially asymmetric motion when exposed to a CCW rotating magnetic field[62,63]. An example of such a motion is shown in Figure 3-2a that presents a series of overlapped images of a cilium actuated by a CCW rotating magnet. These overlapped experimental images are obtained from Video 2 in the supplemental material, showing the motion of a cilium induced by CCW rotation of the magnet. In Figure 3-2b, simulation results for cilium positions under conditions similar to the experiment presented in Figure 3-2a. Good qualitative agreement between the prediction of the computational model and experimental results are recorded. These results are also in agreement with the simulation results reported by Khaderi and Onck[69].

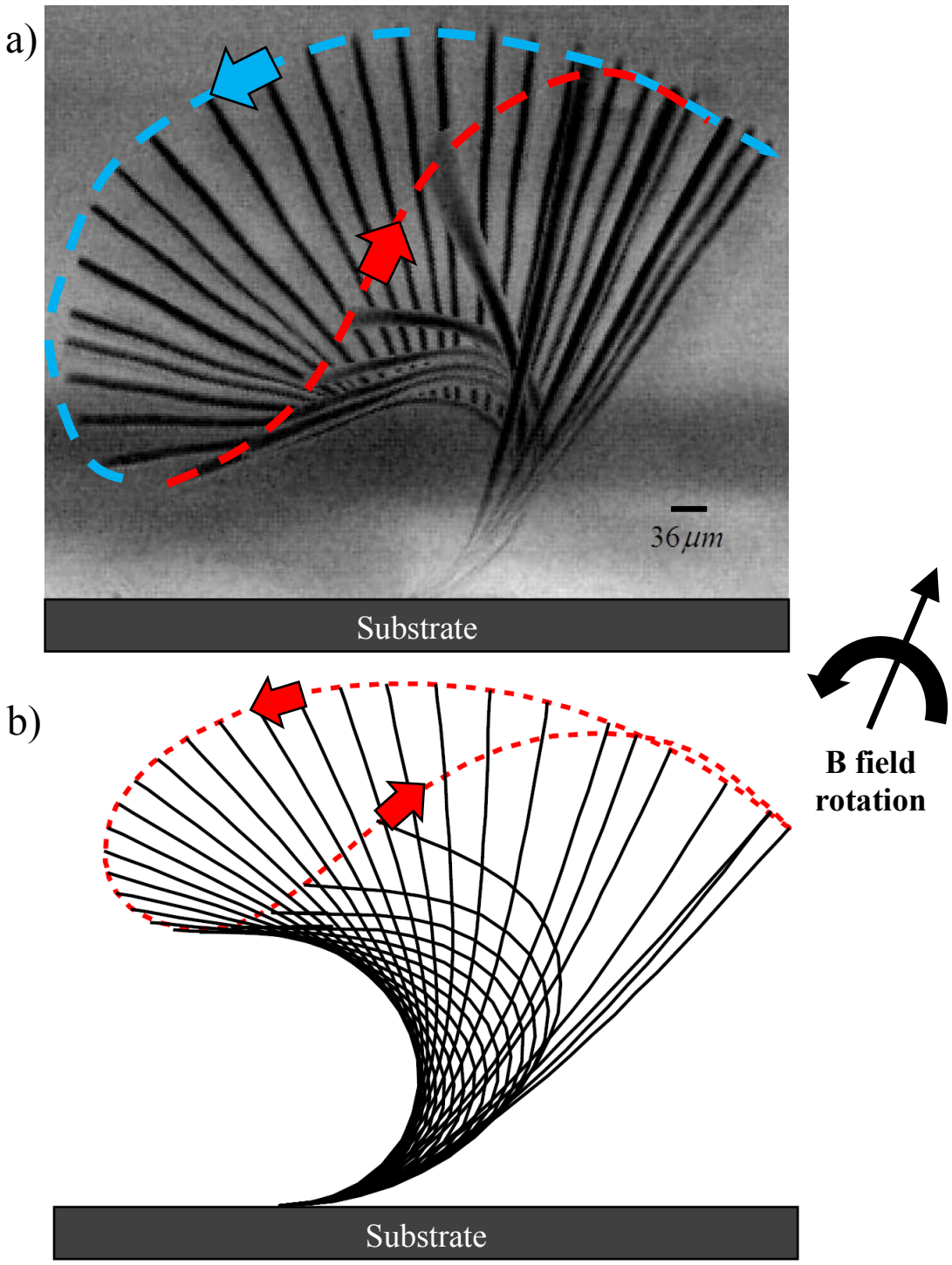

Figure 3-2: Magnetic cilium oscillation due to a CCW rotating magnetic field in the $x-y$ plane (**a**) Experimental snapshots of a cilium with the following parameters: $L=480\mu m$, $W=10\mu m$, $Th=55nm$, $\omega=0.3Hz$, $B=600Gauss$, $\mu=1cP$. These parameters correspond to $Sp=3.6$ and $Mn=4.1$. Cilium positions ***P1*** and ***P2*** indicate

the beginning of the forward and recovery strokes, respectively. The tip trajectories during the forward and recovery strokes are shown by the solid and dotted lines, respectively. The snapshots are obtained from Video 2, in supplemental material. (**b**) Trajectory of the cilium obtained using computer simulations.

The tip trajectory in Figure 3-2 represents an enclosed curve with distinct paths corresponding to the cilium forward (in the direction of magnet rotation) and backward (against the direction of magnet rotation) motions. Thus, the cilium follows an asymmetric stroke where its motion differs significantly between the forward and recovery sections. The stroke asymmetry arises as a result of a difference in the forces governing the forward and backward (recovery) strokes, as discussed below in detail.

Magnetic forcing of elastic cilium by considering a cilium at selected positions throughout an oscillation cycle are depicted in Figure 3-2. The forward stroke begins when the cilium assumes the rightmost position denoted by (a) in Figure 3-3. The time corresponding to this position as $t = 0$. In position (a), most of the cilium is well aligned with the direction of the magnetic field, and experiences less forces, except for a short segment near the base where a bending moment arises due to the local curvature. As the magnetic field rotates CCW, the cilium bends such that its tip remains aligned with the field as shown for the positions (b) and (c). At the same time, the distributed magnetic moment near the base increases in magnitude and expands towards the tip. This happens due to increased bending which results in greater curvature near the base. Note that at position (c), the local magnetic moment at the base changes direction and acts to enhance the bending by increasing the curvature.

In position (d), the angle between the tip and the *x* axis reaches the maximum. This position is used to define the end of the forward stroke and the beginning of the recovery stroke. The forward stroke lasts for the majority of the cycle. Due to the high curvature in this position, the bending magnetic moment changes sign twice along the length leading to a complex effect on cilium deformation.

Magnetic field rotation beyond position (d) results in a situation where the tip experiences a decreasing magnetic moment such that the elastic force exceeds it and the cilium rapidly straightens releasing the accumulated elastic energy and swiftly following position (e). Furthermore, magnetic moment along the entire cilium, except for a small portion near the base, acts to straighten the cilium, enhancing the action of internal elastic bending moments. Thus, during this portion of the recovery stroke magnetic moments facilitates the straightening of the cilium and it moves to position (a). After the cilium returns to this position, the cycle repeats.

An important difference between the forward and recovery strokes is related to the action of the drag force due to the surrounding viscous fluid. During the forward stroke, the cilium closely follows the magnetic field rotation and the rate of bending is proportional to the rotation rate of the field. When the rotation rate is low, slow velocities lead to relatively low viscous drag. In such cases, motion during the forward stroke can be seen as quasi-static. If the rotation of the magnetic field is stopped, the motion of the cilium will stop, and it will remain in equilibrium, in the position corresponding to a specific direction of the magnetic field. This equilibrium position is defined by a balance between the induced magnetic moment and the internal elastic force.

This quasi-static behavior can only be observed during the initial part of the recovery stroke. During the latter part of the recovery stroke, cilium behavior changes drastically as it rapidly snaps to the right due to the release of accumulated elastic energy. In this case, its velocity is defined by a balance between the internal elastic forcing and the viscous drag on the rapidly moving cilium. The time of the forward stroke t_f is more than 10 times longer that the time of the recovery stroke t_r. Since the recovery stroke occurs in a short interval of time, larger viscous force experienced during this part of the recovery stroke. Although the instantaneous velocity of the cilia can be significant in certain parts of the recovery stroke, it is rapidly dissipated by the viscous drag keeping the inertial effects negligible[70].

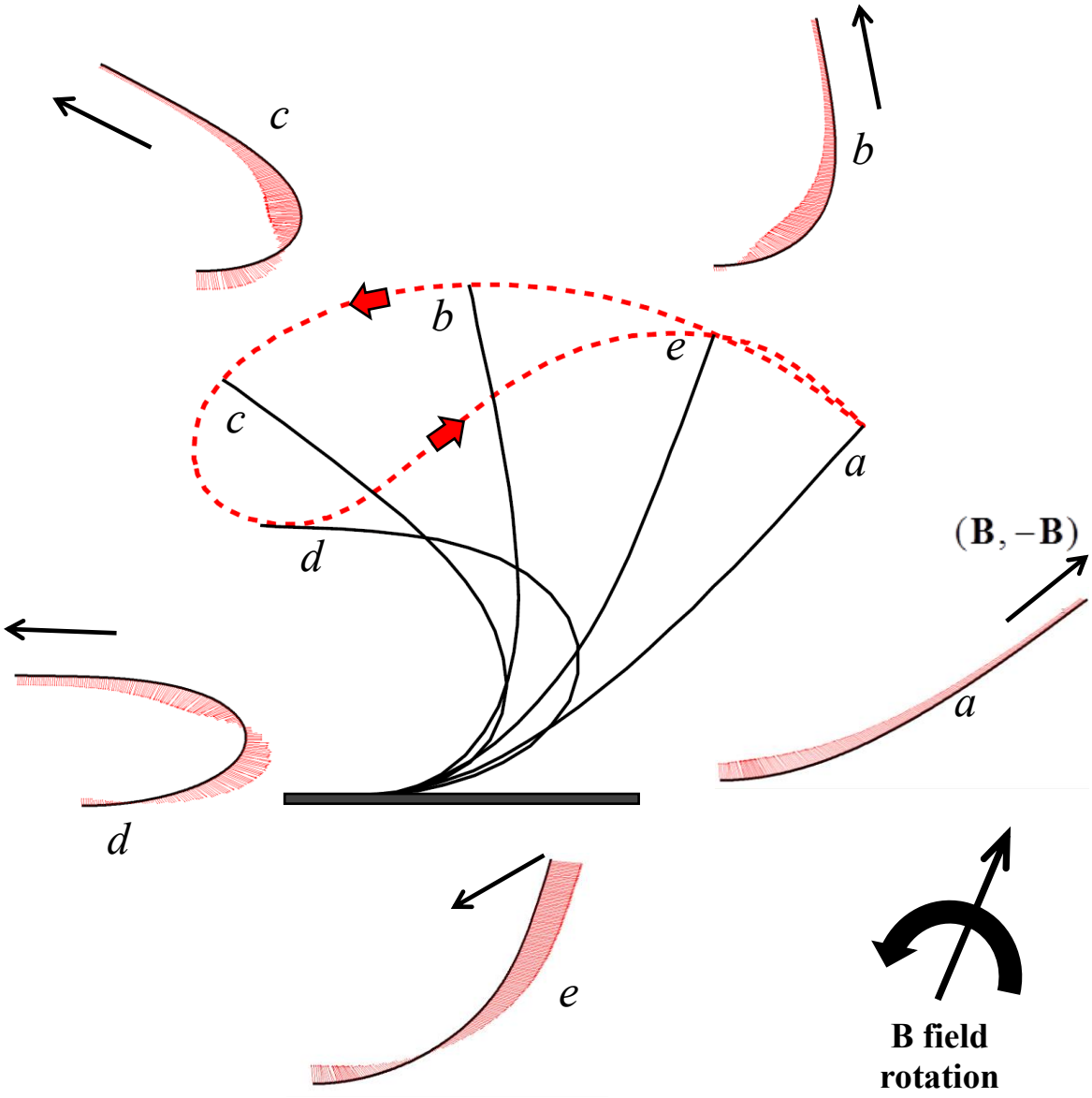

Figure 3-3: Cilium positions *a*-*e* at selected times throughout one oscillation cycle for CCW rotation of the magnetic field. Black arrows indicate the direction of the external magnetic field. The magnitude and direction of the applied magnetic moment along the cilium length are shown in red as a distribution plotted normal to the local cilium axis for the corresponding positions. Note that the magnetic moment varies continuously along the length.

3.3.2 Clockwise rotation of magnetic field

Figure 3-4a. shows a cilium that is subjected to a magnetic field rotating in the CW direction. This cilium has the same properties as the one shown in Figure 3-2a. It is found that cilium beating due to CW magnet rotation differs significantly from that induced by the CCW rotation of the magnet (cf. Figure 3-2 and Figure 3-4). The limiting positions *a* and *d* between which the cilium oscillates are shifted to the right when the magnet rotation is changed from CCW to CW (i.e., the cilia tend to deform in the direction of the magnet rotation). Furthermore, the area enclosed by the cilium tip is significantly smaller for the CW rotating magnet than for the CCW rotation. This indicates that the CCW magnet rotation is beneficial for enhancing beating asymmetry.

Cilium motion obtained in the experiments (Figure 3-4a) is well captured by the computer simulations (Figure 3-4b). The CW forward stroke is defined to begin at position *a* (Figure 3-5). In this position most of the cilium is aligned with the field direction, except near the base. As the magnetic field rotates in the CW direction, the magnetic moment decreases bending as shown in Figure 3-5. This follows the rotating field until position *d* when it touches the substrate. The magnetic moment at this position is negligible since the cilium is fully aligned with the field. It remains at this position *d* prevented by the substrate to move as the magnetic field continues to rotate CW until the angle θ between the cilium and field is less than 90^0, the moments act in the clockwise direction, and force the cilium to remain in position *d*.

When the magnetic field is oriented vertically, θ is equal to 90^0. Further rotation of the field flips the magnetization in the cilium and leads to a situation where the angle between cilium and $-\mathbf{B}$ reduces. This is indicated by *d'* in Figure 3-5. The cilium does

not move and is aligned along the substrate between positions *d* and *d'*. The magnetic moments at *d'* flips direction and pulls it upwards and away from the substrate. As the cilium bends to align with the magnetic field, it goes thorough an intermediate position *e* and completes the recovery stroke back at the nearly vertical position *a*. Thus, during the recovery stroke it moves in the direction opposite to the rotation of the field.

Similar to the CCW field rotation scenario, speed during forward stroke is set by the rate of the CW magnetic field rotation. During the backward stroke, cilium motion is defined by the balance between magnetic force and viscous forces. (Recall that for CCW rotation, the recovery stroke is a result of balance between the elastic and viscous forces) The difference in acting forces between the forward and recovery strokes gives rise to the asymmetry of the motion in CW rotating magnetic field. Note that at the end of the forward stroke the cilium pauses while the magnetic field continues to rotate clockwise until the magnetization changes direction. No such pause exists for cilia driven by the CCW rotating magnetic field.

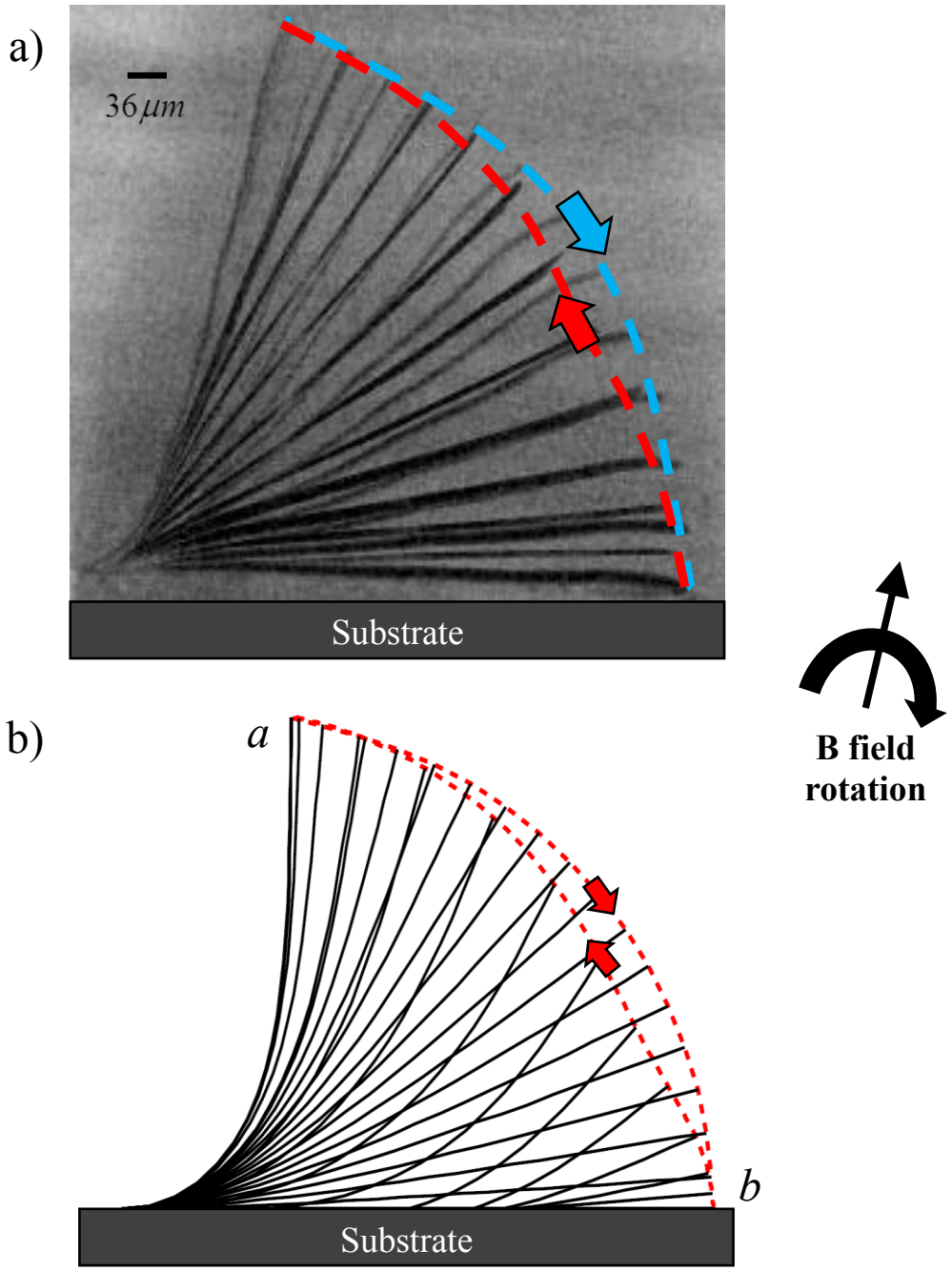

Figure 3-4: Cilium kinematics for the clockwise rotation of magnetic field. **a)** Overlay of experimentally recorded time lapse, from Video 2. **b)** Computer simulations obtained using COMSOL multiphysics. Cilium length is $L = 480\mu m$, and the actuation frequency is $1Hz$.

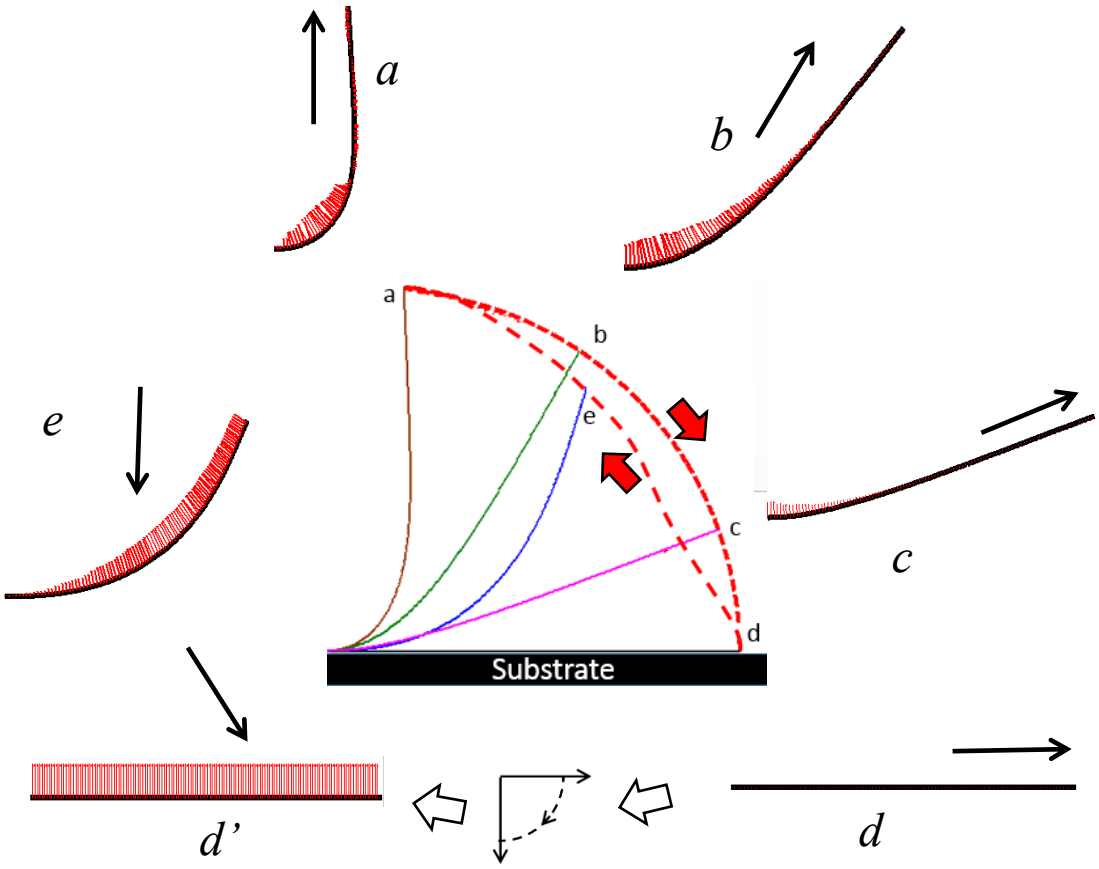

Figure 3-5: Cilium positions *a-e* at selected times throughout one oscillation cycle for CW rotation of the magnetic field. Black arrows indicate the direction of the external magnetic field. The magnitude and direction of the applied magnetic moment along the cilium length are shown in red as a distribution plotted normal to the local cilium axis for the corresponding positions. Note that the magnetic moment varies continuously along the length..

Both CW and CCW modes of cilium actuation result in two cycles of cilium beating for every rotation of the magnetic field. However, the kinematics is significantly different for these two modes. The CCW rotating magnetic field acts to increase the bending during the forward stroke, whereas CW rotation reduces the bending in the

forward stroke. These differences result in significantly different bending patterns for the CW and CCW directions of magnet rotation. Furthermore, CCW rotation leads to a significantly larger spatial asymmetry of beating cycle compared to the CW case. In the following sections, the asymmetry for the more interesting CCW rotation of the magnet is characterized.

3.4 Dimensionless parameters

The kinematics of fluid structure interactions between the cilia and the surrounding fluid can be simplified by grouping relevant parameters into dimensionless groups. For this case of magnetic cilia, the motion is governed by magnetic, inertial, viscous and elastic forces. Using these different forces acting on the cilia, three dimensionless parameters are considered- Reynolds number Re, Magnetic number Mn and Sperm number Sp.

The Reynolds number $Re = \rho LWf / \mu$ is the ratio of inertial forces to viscous forces. Here, ρ is the density, L is the length of the cilium, W is the width, f is the frequency of operation, and μ is the viscosity of water. Re is estimated to be in the range between 0.09 and 0.6 for all the experiments. For these relatively low values of Re, the cilia operate in a flow regime that is dominated by viscous forces[3]. This has been discussed in detail in chapter 1.

It has been shown that for $Re << 1$, since the fluid inertia is negligible, the kinematics is entirely governed by magnetic, elastic and viscous forces. The action of these forces can be characterized using two dimensionless parameters- magnetic number

Mn and a sperm number Sp.[17,63,70] The sperm number $Sp = L\left(\omega\xi/EI\right)^{0.25}$ characterizes the ratio of viscous to elastic forces acting on the cilia. Here $\omega = 2\pi f$ is the angular velocity, $\xi = 4\pi\mu$ is the lateral drag coefficient of the cilium, and EI is the cilium bending rigidity.

The magnetic number $Mn = \left(B^2L^2WP/\mu_0 EI\right)^{0.5}$ represents the ratio of magnetic and elastic forces acting on the cilia[17,61,63,68]. Here, $B = |\mathbf{B}|$ is the magnitude of the magnetic flux density, W and P are the cilium width and thickness, respectively, and $\mu_0 = 4\pi \times 10^{-7}$ is the permittivity of free space. For this experimental setup, an estimated average error of ± 0.05 in measuring Sp and ± 0.12 in Mn is considered.

3.5 Characterizing the asymmetric strokes

The demonstrated spatial asymmetry (Figure 3-2 and Figure 3-4) is critical for creating a net fluid flow[3,58]. Simulations by Khaderi et al.[68] have shown a direct dependence between the flow rate and area enclosed by the tip trajectory. It is, therefore, important to examine how the tip trajectory changes depending on the non-dimensional parameters of the system. This information is essential for the use of magnetic cilia in fluid pumping applications. In Figure 3-6a, trajectories of the cilium tips driven at different values of Sp and a constant $Mn = 4.1.$ are shown. To change Sp the frequency of the magnetic field rotation is varied. For low $Sp = 3.6$, the viscous drag force in the forward stroke is relatively low, allowing for large deflection of the cilium. Increasing Sp increases the viscous drag during the forward stroke, reducing the magnitude of cilium deflection during the oscillation cycle. Thus, increasing Sp leads to a smaller

amplitude of oscillation and smaller area enclosed by the trajectory of the tip. For smaller values of Sp equal to 3.6 and 4.1 the tip trajectories change only slightly, indicating a limiting cycle behavior for the smaller values of Sp.

Figure 3-6b shows the tip trajectories for different magnitudes of Mn and a constant $Sp = 3.6$. Here, Mn is changed by varying the magnetic flux density. It is found that the cilium oscillated at a higher value of $Mn = 4.1$ exhibits a larger deflection. This is a result of a relatively large magnetic force compared to the elastic force that enables significant cilium deformation. As Mn decreases, the deflection is reduced due to the lower magnetic moments, which is unable to bend the elastic cilium to achieve large deformations. Thus, reduction of Mn, leads to a smaller amplitude of the tip deflection and consequently smaller area enclosed by the tip trajectory.

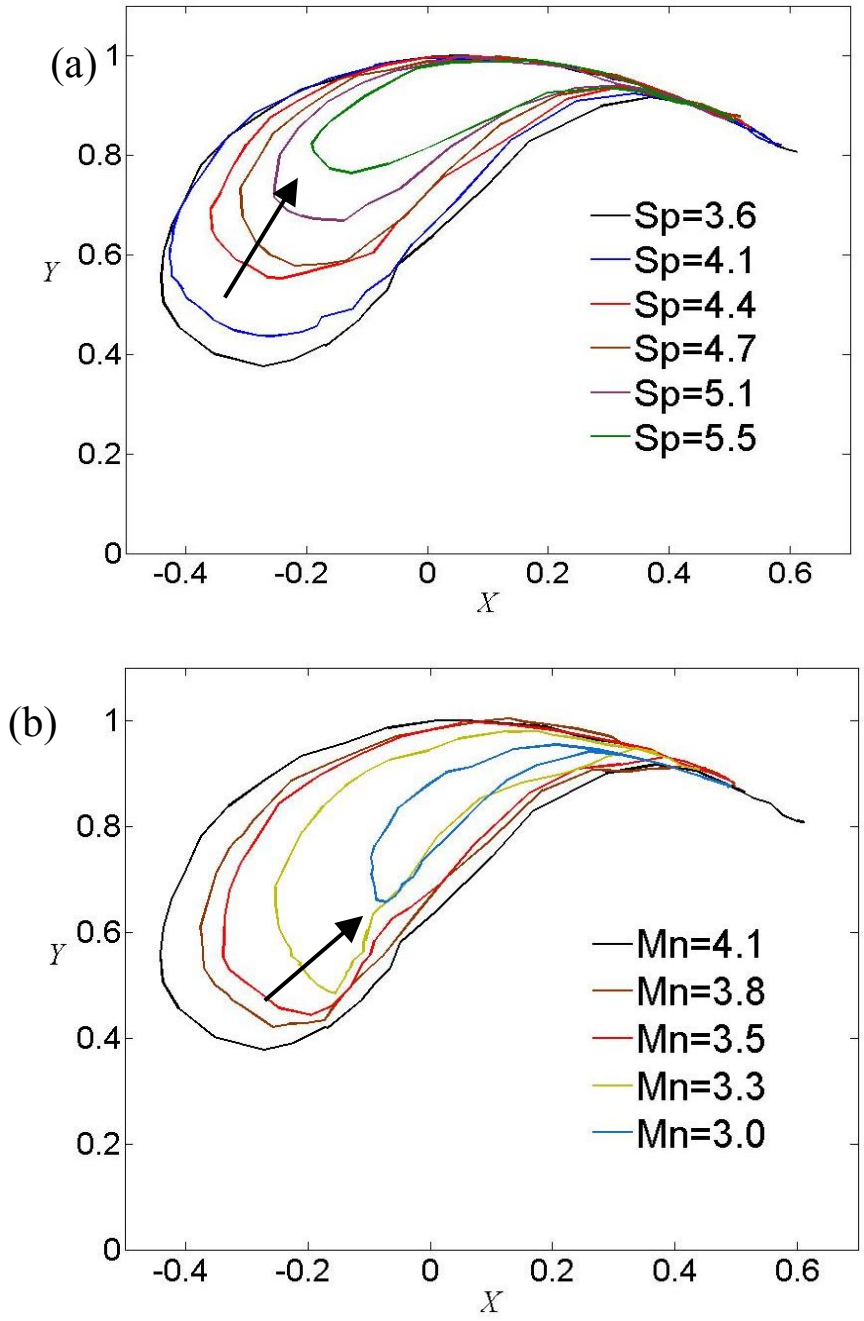

Figure 3-6: Experimental trajectories of cilium tip normalized by cilium length. (**a**) Tip trajectories for different values of sperm number *Sp* varied by changing the frequencies magnetic field rotation. The arrow indicates tip trajectories with increasing *Sp*. (**b**) Tip trajectories for different values of magnetic number *Mn* varied by changing **B**. The arrow shows the trajectories with decreasing *Mn*.

In the limit of low Re, fluid motion is fully defined by the kinematics of cilium stroke and its spatial asymmetry[58]. As discussed above, the magnitude of cilium deformation during the recovery stroke is set by the balance of elastic and viscous forces. Since the viscous force is proportional to the cilium velocity, it is important to characterize the relative extent of the forward and recovery strokes that depend on the actuation regime. To this end, a dimensionless stroke time ratio $t_s = \frac{t_f - t_r}{t_f + t_r}$ is defined, where t_f is the duration of the forward stroke and t_r is the duration of the recovery stroke indicated by the cilium positions ***P1*** and ***P2*** in Figure 3-2a. This parameter is used to characterize the difference in forward and recovery stroke velocities. When $t_s = 1$ the recovery velocity significantly exceeds the velocity during the forward stroke leading to a stroke with high spatial asymmetry. On the other hand, $t_s = 0$ corresponds to a stroke where the velocities of the forward and recovery strokes are equal resulting in a nearly symmetrical stroke kinematics.

In Figure 3-7a, t_s is shown as a function of Sp for two values of Mn. In these experiments B, ω, L, P, and μ are varied to alter the dimensionless parameters. The values of t_s collapse onto a single curve for each value of Mn. This confirms that the motion of an elastic magnetic cilium is defined by two dimensionless numbers, Mn and Sp. The figure also shows that t_s decreases with increasing Sp. This can be explained by the increasing effect of viscous force damping the velocity of cilium motion, which in turn increases the time of the elasticity-driven recovery stroke. For larger Sp, t_s converges to a constant value of about 0.25 for both Mn, indicating that, in this limit, the

forward and recovery strokes are nearly equal. On the other hand, for smaller Sp the effect of viscosity is reduced, leading to a shorter recovery time and a larger asymmetry between forward and recovery strokes, as indicated by t_s approaching unity. Furthermore, a stronger magnetic force, indicated by a larger Mn, increases the asymmetry between the forward and recovery strokes for a given Sp.

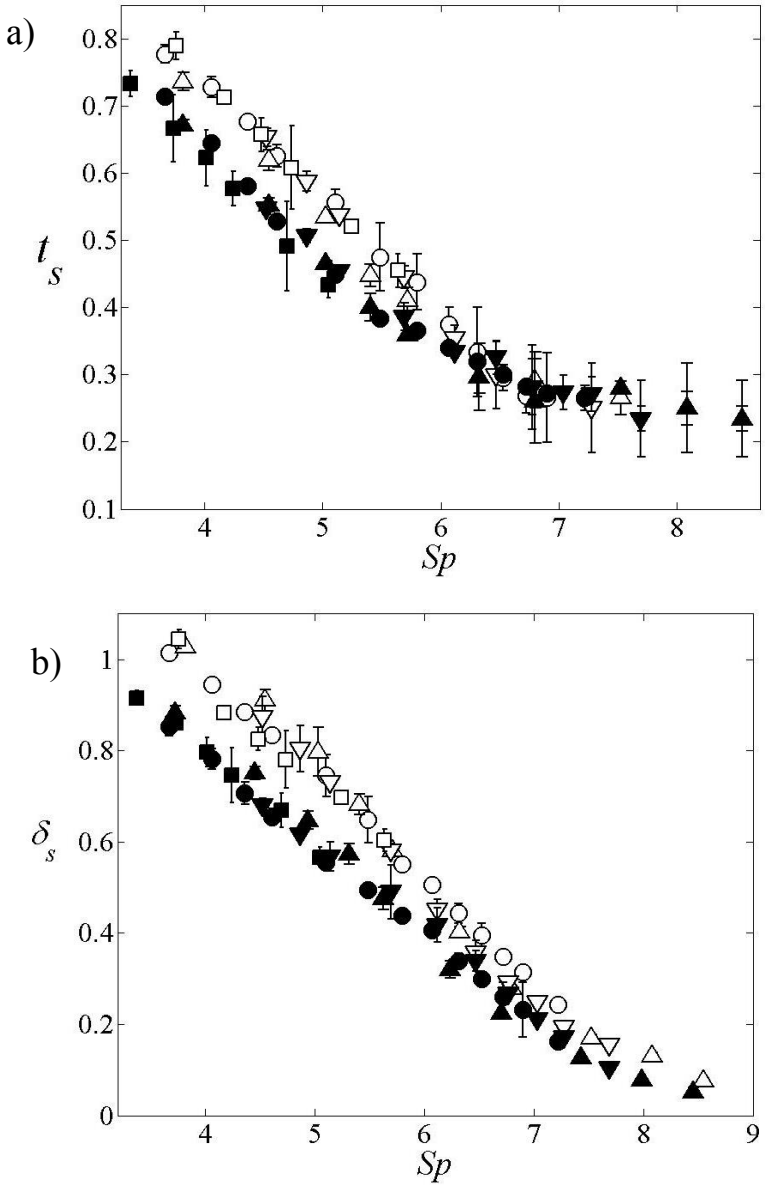

Figure 3-7: (**a**) Normalized time difference between forward and recovery stroke as a function of sperm number Sp for different magnetic numbers Mn. (**b**) Normalized

magnitude of cilium deflection as a function of sperm number Sp for different magnetic numbers Mn. The empty markers represent $Mn = 3.6 \pm 0.12$ and the filled markers represent $Mn = 3.1 \pm 0.08$. ○: $B = 600Gauss$, $L = 480\mu m$, $Th = 56nm$, $\mu = 1cP$; Δ: $B = 760Gauss$, $L = 480\mu m$, $Th = 68nm$, $\mu = 4cP$; ∇: $B = 760Gauss$, $L = 480\mu m$, $Th = 68nm$, $\mu = 2.1cP$; □: $B = 600Gauss$, $L = 480\mu m$, $Th = 68nm$, $\mu = 1cP$; ●: $B = 530Gauss$, $L = 480\mu m$, $Th = 56nm$, $\mu = 1cP$; ▲: $B = 650Gauss$, $L = 480\mu m$, $Th = 68nm$, $\mu = 4cP$; ▼: $B = 650Gauss$, $L = 480\mu m$, $Th = 68nm$, $\mu = 2.1cP$; ■: $B = 600Gauss$, $L = 430\mu m$, $Th = 56nm$, $\mu = 1cP$.

To characterize the extent of the deflection of cilium, a normalized deflection amplitude $\delta_s = \delta_{\max}/L$ is introduced. Here, $\delta_{\max}$ is the projected length of the trajectory in the x- direction and L is the cilium length (Figure 3-2a). Figure 3-7b shows the variation of δ_s as a function of Sp for two values of Mn. It is found that δ_s obtained from different experiments collapse on to curves depending only on Mn. Further it is noted that δ_s decreases with increasing Sp. The reduction of the cilium amplitude is related to the increased effect of viscosity during the forward stroke. Viscous drag causes the cilium to lag behind rotating **B** during the forward stroke, decreasing the angle at which it can no longer follow **B**. This in turn, shortens the forward stroke and decreases deflection δ_s. The magnitude of cilium deflection δ_s also decreases with decreasing Mn. Thus, increasing Sp and decreasing Mn act to suppress the deflection of the cilium. It is found that for larger Sp the viscous force nearly completely stops cilium motion in which case δ_s approaches zero. This also agrees with a minute time difference between the forward and recovery strokes for larger values of Sp shown in Fig. 5a.

It is noted that the Reynolds number for the data presented in Figure 3-7 vary in the range between 0.006 and 0.12. The fact that the data collapse into the master curves independently of particular values of the Reynolds number supports the assumption that inertial effects play a negligible role for experimental conditions tested. However, that it may not be the case for larger values of Reynolds number than those used in the experiments, in which case inertial effects can influence the cilium bending pattern[70].

3.6 Summary

It is shown that when a thin permalloy cilium is actuated by a uniformly rotating magnetic field, it exhibits spatially asymmetric periodic motion. Kinematics of a such beating is examined by imaging its stroke pattern. The cilium follows different bending pattern defined by the direction of magnet rotation. The CCW rotation of the magnet produces larger spatial asymmetry in the beating pattern compared to the CW rotation of the magnet. The cilium follows the rotation of the magnetic field during the forward stroke, and returns traversing a different path in the recovery stroke. It is found that the time of the forward stroke which is proportional to the angular rotation rate of the magnet differs significantly from the time of the recovery stroke. The relative importance of magnetic, elastic, and viscous forces in terms of dimensionless magnetic (Mn) and sperm numbers (Sp) are characterized. The experimental demonstration shows the dependence of cilium kinematics on these dimensionless parameters for CCW rotating magnetic field. For small values of the sperm number, the recovery stroke is significantly faster than the forward stroke, leading to asymmetric oscillations of the cilium characterized by a large area enclosed by the tip trajectory. These cilium oscillations are promising for creating spatially asymmetric motion required to induce fluid pumping and

other transport processes in a low Reynolds number environment[68]. It is noted that this fabrication approach allows us to readily create extended arrays of multiple simultaneously beating cilia, including heterogeneous arrays of cilia with different geometries. Understanding the dynamic behavior of a single isolated cilium, sets the stage for future exploration of more complex cilium systems. Multiple important effects can be investigated using magnetic cilia arrays. Furthermore, formation of biomimetic metachronal waves has been suggested for magnetic cilia[69,79]. It has been also reported that actuation of cilia at greater Reynolds numbers can lead to dramatic changes in cilium beating pattern and ultimately flow reversal[70]. These and other effects make the magnetic elastic cilia especially attractive for a range of microfluidic applications including fluid transport, mixing, particle capture, etc. which are the subject of Chapter 4,Chapter 5, Chapter 7.

Chapter 4. FLUID TRANSPORT CHARACTERISTICS OF ARRAYS OF ARTIFICIAL MAGNETIC CILIA

One of the vital functions of naturally occurring cilia is fluid transport. Biological cilia use spatially asymmetric strokes to generate a net fluid flow that can be utilized for feeding, swimming, and other functions. Biomimetic synthetic cilia with similar asymmetric beating can be useful for fluid manipulations in lab-on-chip devices. In this chapter, microfluidic pumping by magnetically-actuated synthetic cilia arranged in multi-row arrays is demonstrated. A microchannel loop to visualize flow created by the ciliary array and to examine pumping for a range of cilia and microchannel parameters. Magnetic cilia can achieve flow rates of up to $11 \mu l/min$ with the pressure drop of $\sim 1 Pa$. Such magnetic ciliary array can be useful in microfluidic applications requiring rapid and controlled fluid transport.

4.1 Introduction

Achieving fluid transport at the microscale is particularly difficult owing to the lack of inertial effects[2,3]. It means that any reciprocal motion displaces the fluid back and forth without producing any net flow[80]. Microorganisms typically operate in these regimes of negligible inertial effects. To perform vital biophysical functions requiring fluid agitation and motion, microorganisms have evolved to use cilia and flagella with complex beating patterns yielding a net fluid transport[4–6,75]. Ciliary bands are used to produce feeding currents that draws the food particles towards the mouth of the organism for feeding[9,10]. Cilia facilitate organism swimming[10,11]. Further, the flow produced by motile cilia in an embryo is shown to directly affect the developing organism left-right

asymmetry[81]. The cilia beating can be planar or three-dimensional[82]. Researchers have studied flow patterns generated by natural cilia[9–11,81,83–85] and have shown that ciliary carpets[84,85] are able to produce flow speeds of up $1 mm/s$. These biological cilia inspire researchers to develop synthetic analogs of cilia capable of performing complex biomimetic functions that could prove to be useful for lab-on-chip microfluidic devices, in vitro and in vivo artificial organs, and drug delivery applications[1,13–15,54,86–88].

Different fabrication methods have been demonstrated to create artificial cilia capable of microfluidic pumping[59,64,89]. Researchers have used continuous roll up approach[59] to fabricate synthetic cilia and have demonstrated transitional flow speeds up to $120 \mu m/s$ in such systems. The self-pumping frequency – a metric used to assess the effectiveness of the pump based on its size[90] (ratio of the flowrate to package size $f_s = Q / S_{package}$) is estimated to be $0.2 \min^{-1}$ for this pump. Wang et al[89] have used self-assembled magnetic bead cilia to demonstrate transitional flow speeds of $\sim 240 \mu m/s$. Toonder et al.[91] fabricated micro beams from bilayer films of polyimide and chromium. Their cilia showed substantial mixing and pumping abilities when actuated electrostatically and demonstrated a translational fluid flow rate of over $500 \mu m/s$. Fahrni et al.[64] made ferromagnetic PDMS flaps using photolithography techniques and actuated them externally using an electromagnetic setup with a frequency up to $50 Hz$. Rotational as well as translational flow was created with instantaneous fluid velocities of up to $\sim 500 \mu m/s$. Hussong et al.[92] have shown the use of polymeric cilia capable of producing net transitional velocities of up to $\sim 130 \mu m/s$. In general, ciliary pumps have shown to produce a relatively high flowrate, whereas the pressure drop in these systems

is relatively low ($\sim 1Pa$). Among different fabrication and actuation techniques demonstrated for artificial cilia, the use of magnetic cilia is highly promising due to the ease of actuation by manipulating an external magnetic field. Further, magnetic actuation does not interfere with the biological samples making such cilia especially useful in various biomedical applications.

Researchers have studied the mechanism of artificial cilia beating and fluid transport through computer simulations[58,68,69,87]. Khadri et al.[60] have simulated the pumping characteristics of magnetic cilia in a microchannel. They show results with cilia capable of producing flow rates of $\sim 18\mu l/min$ and $3mm$ of water pressure. The net flow generated by magnetic cilia and its relation to the beating pattern and Reynolds number was analyzed[70]. Researchers have also examined the effects of multiple cilia interacting in an array and discussed the effects of metachronal waves[79,93] (See chapter 5). The use of cilia for micro-particle capture[12,14–16], particle transport[71], and flow control[87] has been examined using computational modeling (See chapter 7).

As discussed in Chapter 3, a magnetic filament actuated by a rotating magnetic field produces spatially asymmetric motion[63] in a two-dimensional plane of oscillation. Furthermore, this motion is time-irreversible, in that, reversing the direction of magnet rotation results in a different beating pattern. In this chapter, the effect of these different beating pattern is looked into, obtained by reversing the rotation of the magnetic field, on fluid pumping. The net pumping generated by an array of synchronously actuated cilia are characterized. To quantify the pumping, an array of cilia inside a closed loop micro-channel is incorporated. Thus, actuated cilia pump and circulate fluid through the channel loop. The pumping rate is measured by visualizing the flow. The combined effect of

multiple beating cilia generates rapid microfluidic pumping with rates that depend on parameters including the direction of magnet rotation, the cilia properties, dimensions of ciliary array and the microchannel dimensions. These cilia arrays can generate transitional flow speeds of up to $1.4mm/s$ corresponding to a flowrate of $11\mu l/min$ in closed loop channels. To the best of this research's scope, these results are the highest reported flowrates for such ciliary pumps. These magnetic cilia can find applications in biomedical assays. Closed loop pumping systems are useful in cell culture applications, where a fluid sample needs to be circulated continuously. They can potentially replace conventional peristaltic pumps, which are bulky and expensive.

4.2 Setup and experimental protocol of pumping experiments

To study the fluid pumped by the cilia, an array of cilia was incorporated inside a microchannel loop. The dimensions of the cilia are length $L = 200\mu m$, width $W = 20\mu m$, and thickness $P = 60nm$, whereas the spacing between neighboring cilia within a row is $20\mu m$. A PDMS microchannel loop (width of $1mm$, depth of $300\mu m$, and loop length of ~$36mm$) is fabricated using standard soft lithography[94] and two inlet/outlet holes are punched for adding and removing the fluid. The channel is then placed on the glass substrate decorated with a micro-machined ciliary array, and gently pressed to form a reversible bond.

After bonding the PDMS on glass surface, pure ethanol is introduced to wet the inner walls of the channel. DI water is then introduced in the already wet channel to displace ethanol. This is followed by introducing 5% ammonium hydroxide to selectively etch the copper sacrificial layer and release the cilia. The last step is to displace the

ammonia water with DI water containing fluorescent beads ($3\mu m$, Fluoro-Max, Thermo-Fisher scientific) for flow visualization. Lastly, the inlet/outlet reservoirs are sealed by placing a glass coverslip on top of the PDMS and gently pressing. This process results in a leak free channel loop with cilia on the bottom channel wall. Videos of fluorescent beads are recorded under a microscope to evaluate the fluid flow velocity. A schematic of the experimental setup is shown in Figure 4-1.

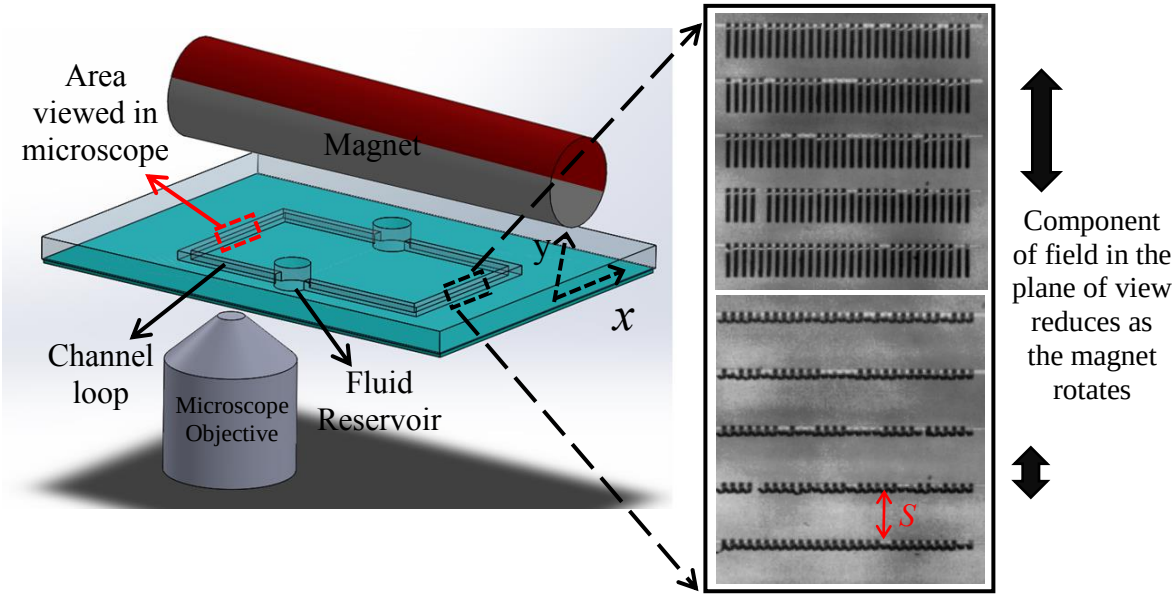

Figure 4-1: Schematic of experimental setup showing a microchannel loop through which the fluid pumped by cilia is circulated. A large diametrically magnetized permanent magnet is used to actuate the cilia. Inset shows actuated ciliary array as seen from the top for two different positions of the magnetic field.

A long permanent magnet magnetized through its diameter (see section 2.4 for details) and rotated along the long axis is used to actuate the ciliary array. The magnet is held in position using a fixture that can be precisely manipulated in the x and y

directions such that the magnet axis aligns with the center of the array. The diameter of the permanent magnet is $D = 12.5mm$, which is significantly larger than the size of an individual cilium with is about $100\mu m$. This ensures that each cilium is exposed to a nearly uniform magnetic field. Figure 1 shows the top view of a ciliary array at two positions of the beating cycle. All cilia show the same in-phase motion due to their synchronous actuation. See Video 3 in ESI.

In these experiments, the pumping by varying the frequency, direction of rotation, number of cilia rows, spacing between rows, and the channel height is characterized. The pumping produced by ciliary array is characterized by measuring the centerline flow velocity on the opposite side of the microfluidic channel loop (see section A in Figure 4-1). To measure this velocity, videos of fluorescent particles flowing in the microchannel were recorded. Care was taken to ensure that the particles near the center of the microchannel were imaged. ImageJ is used to track particles by manually selecting the start and end positions. The centerline velocity is computed by measuring the distance travelled by the particles in a given time.

In the experiments reported here, the magnet distance from the array was kept constant at 9*mm*, which corresponds to a magnetic number $Mn \approx 3.1$.

To quantify the pumping by arrays of magnetic cilia, a dimensionless parameter is defined $P_f = U_0 Sp^4 / \omega L$ that represents pumping generated by the ciliary array per unit time[87]. Here, U_0 is the centerline velocity measured in segment *A* of the channel (Figure 4-1).

4.3 Results and discussion

It is known that spatial asymmetry in a beating pattern is essential for creating any net fluid transport at the low Reynolds number environment[58]. A direct correlation between area enclosed by the cilium tip trajectory and fluid transport has been found[60]. In chapter 3, it was shown that the CCW rotation of the magnet results in a larger asymmetric stroke, compared to CW rotation. Therefore, larger fluid transport by cilia actuated by CCW rotating field can be expected.

4.3.1 Fluid pumping by ciliary array

Fluid transport by arrays of magnetic cilia is characterized by measuring the fluid pumping in a microchannel loop. Figure 4-2 shows a comparison of pumping parameter P_f in the microchannel loop for CW and CCW actuated cilia as a function of Sp. In these experiments, 16 rows of cilia are used with 25 individual cilia per row.

It is found that CCW actuation results in superior pumping performance compared to CW actuation mode. This result holds for all Sp tested in the experiment. The maximum pumping rate for cilia in the CCW mode is $P_f \approx 14$, which is significantly higher than the maximum pumping rate at the CW mode equal to $P_f \approx 4.5$. Better pumping performance for a CCW magnet rotation is related to a larger sweep area by the cilium tip compared to CW actuation.

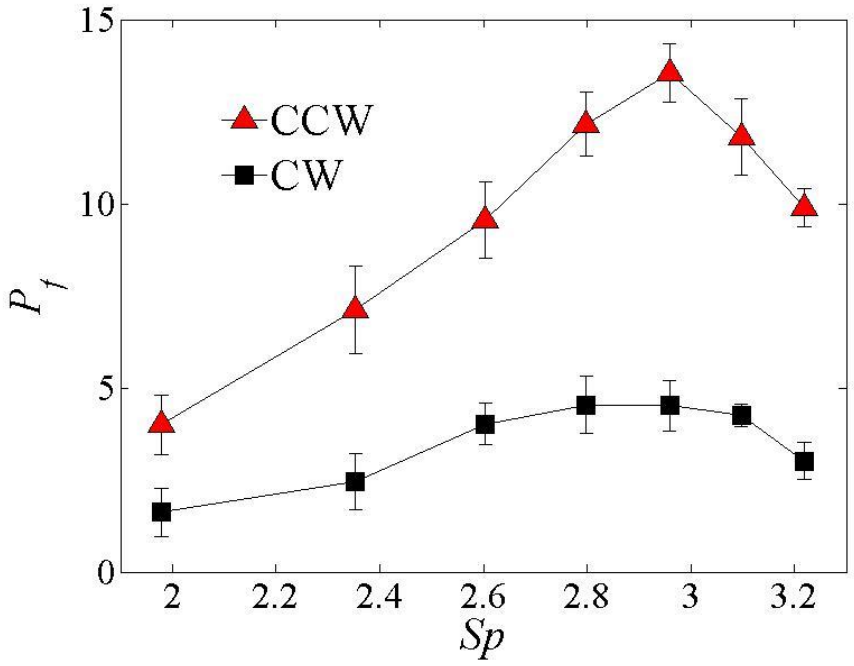

Figure 4-2: Dimensionless pumping rate P_f as a function of Sp, for CCW and CW rotation of the magnetic field actuating a ciliary array. The array has 16 rows of cilia with 25 cilia per row. Spacing between array rows is $S = 250\mu m$, channel height is $H = 300\mu m$.

Furthermore, it is found that the direction of flow for CCW and CW rotation of the magnet is opposite. For both CCW and CW rotation of the magnet, the cilium in forward stroke sweeps through a larger area compared to the recovery stroke. However, the direction of the forward sweep is different as indicated by the blue tip trajectories in Figure 3-2 and Figure 3-4 for the two rotation directions, respectively. The direction of the resulting fluid pumping coincides with the direction of the forward stroke, thus leading to different pumping directions for CCW and CW magnet rotation.

For a constant magnetic number, it is found that the pumping initially increases with increasing Sp until a maximum is reached (Figure 4-2). Further increase in Sp results in a reduction of pumping rate per unit time. For low Sp which was obtained in these experiments at lower oscillation frequencies, cilia experience weaker viscous forces. This allows the cilia to sweep a larger area increasing fluid transport[63]. The overall performance is, however, relatively low since cilia can only complete a few oscillations per unit time. As Sp increases, increasing viscous forces reduce the stroke asymmetry[63] and, therefore, the fluid pumping per oscillation cycle. The faster oscillation rate, on the other hand, increases the overall pumping rate until a maximum is reached at around $Sp \approx 2.9$. Beyond this value, fluid viscosity significantly suppresses cilium beating leading to a decline of the pumping performance.

In these experiments, the maximum pumping rate obtained for CCW actuation is about $P_f \approx 14$ at 2500RPM. This corresponds to a centerline velocity equal to $\sim 1350 \mu m/s$ and volumetric flow rate $\sim 11 \mu l/min$ in a channel with $1mm \times 280 \mu m$ cross-section. This flow rate exceeds the values previously reported for synthetic ciliary systems[60,92]. The self-propelling frequency $f_s = Q/S_{package}$ for this device is estimated to be $\sim 2.5 min^{-1}$, indicating its effectiveness. Assuming a Poiseuille flow in the microchannel, a pressure drop of $\sim 1Pa$ is estimated to be generated by the ciliary array in the $\sim 4cm$ channel loop.

Thus, these ciliary arrays with CCW magnetic actuation exhibit a high pumping flow rate with a low pressure drop, which is consistent with previously reported data[60]. In

what follows, pumping by CCW actuated cilia for different array and channel parameters is systematically examined.

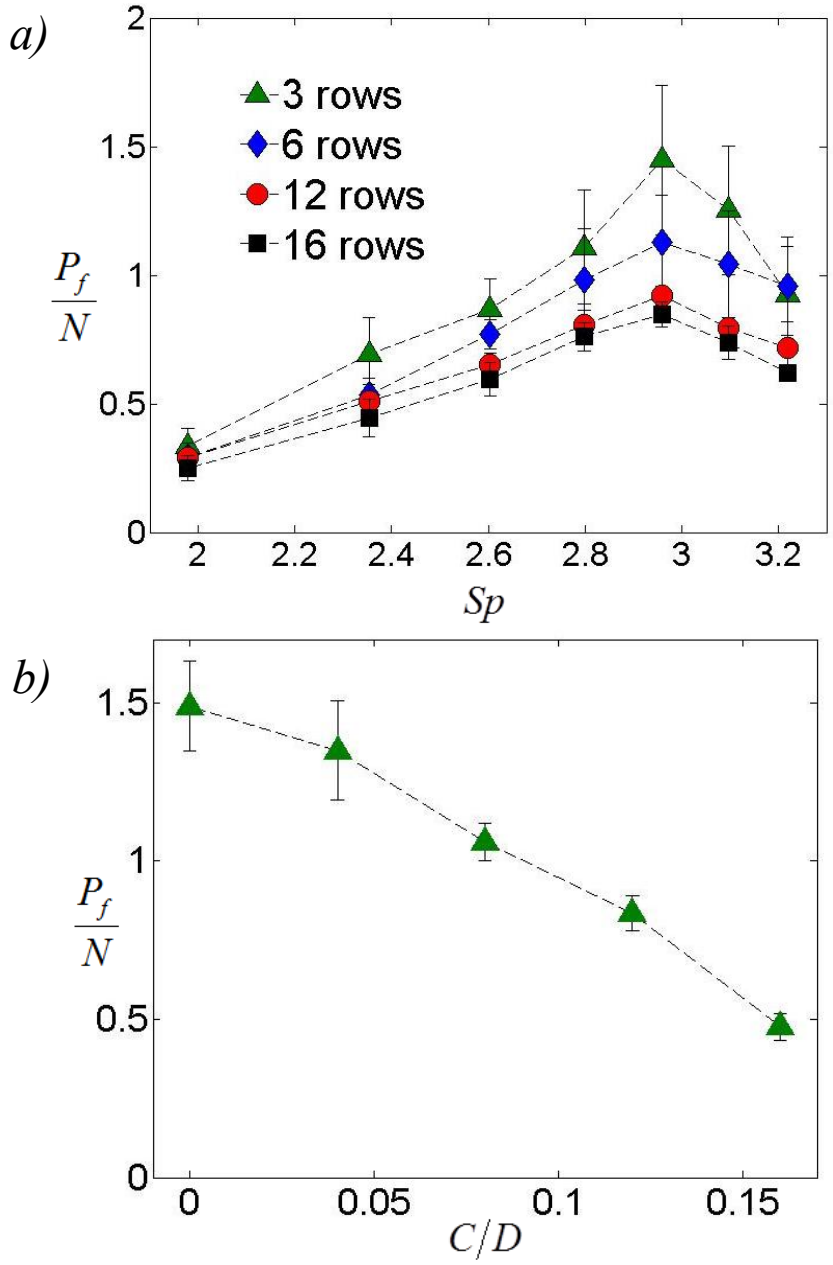

Figure 4-3: **a**) Dimensionless pumping rate P_f produced by ciliary arrays with different number of rows as a function of Sp for CCW rotation of the magnetic field actuating cilia. **b)** Pumping rate per row P_f/N as a function of the normalized distance C/D of the magnet from the center for an array with $N=3$. The arrays have 25 cilia per row with spacing $S=300\mu m$. Channel height is $H=300\mu m$.

Figure 4-3a shows how the ciliary array pumping depends on the number of rows of cilia. Here, the pumping rate P_f is normalized by number of rows of cilia N to characterize the effectiveness per row. The number of rows between 3 and 16, while keeping the separation between rows constant and equal to $300\mu m$. It is found that pumping per row P_f/N decreases as the number of rows in the array increases. This result can be explained based on the difference in magnetic forces experienced by cilia at different rows. As the number of rows is increased, the distance between the magnet and cilia at different rows also changes. Cilia near the array center are closest to the magnet and experience the maximum magnetic force, whereas the cilia in the outer rows of the array experience a reduced force. In these experiments, a $\sim 70 Gauss$ reduction is measured in the magnetic field strength acting on the cilia in outer rows. The reduction in magnetic field strength reduced the beating amplitude of cilia located at the outer rows in the array and, therefore, suppress the overall pumping performance of the ciliary array.

To further investigate the dependence of the cilium performance on the magnet position, experiments are performed in which the magnet distance from an array is varied. A small array with $N = 3$ and displace the magnet in the x direction is chosen. x is defined as the distance between the center of the array and axis of the magnetic field as C. In Figure 4-3b, the magnitude of fluid pumping per row is plotted as P_f/N of the ciliary array with $N = 3$ as a function of the normalized magnet position C/D, where D is the magnet diameter. A significant drop is found in the pumping when C/D is increased from 0 to 0.15. For $C/D = 0.15$, the magnet is displaced by a distance of $2mm$ from the center of the array which is equivalent to the distance to the cilia near the

edges for an array with *N*=16. This result suggests that the reduced pumping per row for larger arrays is indeed related to the reduced magnetic force. This decrease in performance for larger array can be mitigated by using a rotating magnet with a larger diameter to create a more uniform magnetic field across the entire array of cilia.

To understand the mutual influence of cilia in a multi-row arrays, the spacing S (shown in Figure 4-1) is varied between consecutive rows of cilia. The cilia are actuated by CCW magnet rotation. The case where $S/L=1$, represents a scenario in which the rows of cilia are closely packed. Figure 4-4 shows the pumping rate as function of Sp for arrays with different inter-row spacing. Pumping data for the different spacing arrays is found to differ insignificantly. In fact, the average pumping rate is within the experimental error for all S/L. This implies that the cilium performance is not significantly affected by neighboring ciliary rows and the hydrodynamic interaction between them is relatively weak.

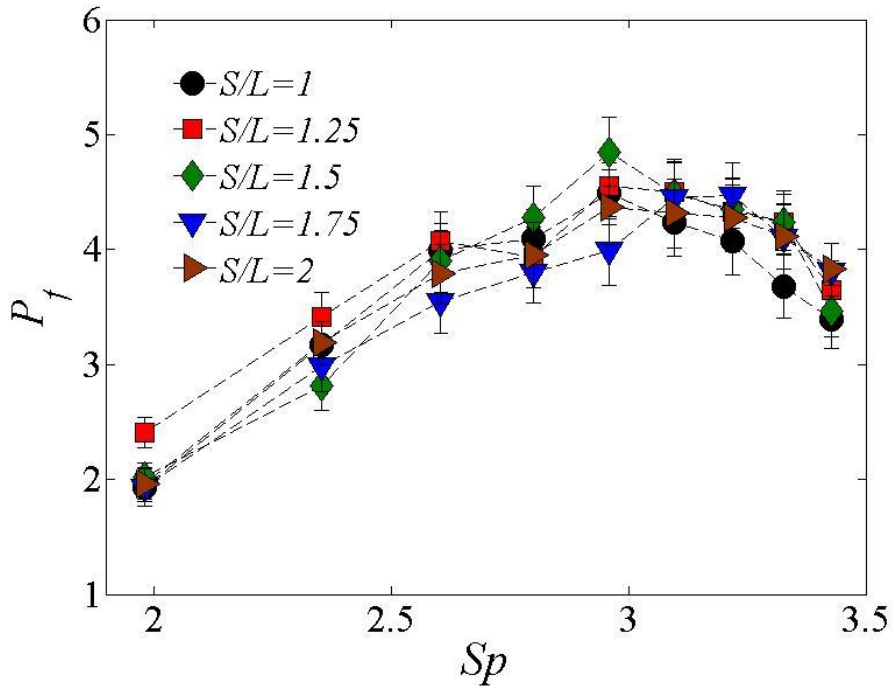

Figure 4-4: Dimensionless pumping rate P_f as a function of Sp for ciliary arrays with different spacing between consecutive rows. All arrays have four rows of cilia with 25 cilia per row. Channel height is $H = 300\mu m$.

In the next set of experiments, dependence of pumping on the channel height H is investigated. Figure 4-5 shows the effect of varying channel height on the pumping. In these experiments, cilia in actuated in CCW mode with three different Sp. The arrays used for these experiments consists of cilia arranged in 4 rows with 25 cilia per row. The channel height is varied between $220\mu m$ to $750\mu m$. A significant increase in pumping rate from $P_f \approx 2.8$ to $P_f \approx 4$, as H/L is increased from 1.2 to 1.8 is found. Further increase in channel height beyond $H/L = 1.8$ results in little change in the pumping rate.

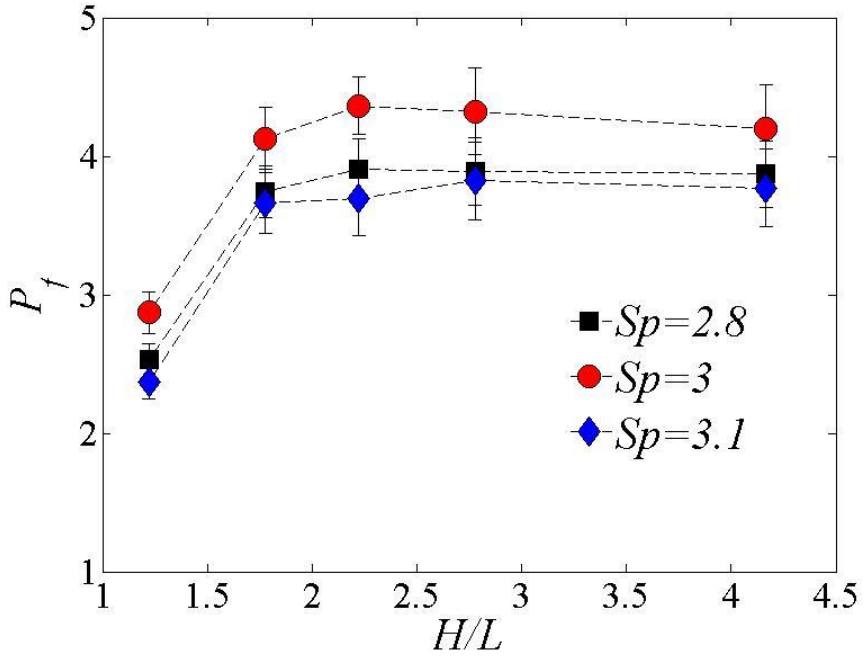

Figure 4-5: Dimensionless pumping rate P_f as a function of normalized channel height H/L for selected values of *Sp*. A ciliary array with four rows of cilia, and 25 cilia per row is used. Spacing between rows of cilia is $S = 250\mu m$.

It is predicted that the flow above the cilia in a closed loop channel with $H >> L$ resembles the Couette flow, with no-slip at the top boundary and bottom boundary being tangentially moved by the cilia[60]. In such cases, the flowrate scales linearly with channel height and the centerline velocity is independent of channel height. These experiments confirm this result, as demonstrated by the negligible change in centerline velocity for $H/L \geq 1.8$. However, when channel height is comparable to cilia length, the centerline velocity decreases as shown for $H/L = 1.2$. This indicates that the motion of the cilia is affected by the channel top wall.

4.4 Microfluidic mixing

Fluid mixing at the microscale is a challenging task because the flow is typically viscosity dominated and the mixing process is governed by relatively slow molecular diffusion. To achieve an efficient and fast mixing, fluid flows that cause repeated stretching and folding of the fluid have to be used. The fluid transport created by magnetic cilia can be used for mixing fluid streams.

To examine the ability of magnetic cilia to effectively mix fluid streams a microfluidic channel with an array of cilia actuated by a rotating permanent magnet is used. Two fluid streams, one of which is fluorescent, are introduced in a Y-shaped microchannel made by PDMS molding and bonding on a glass slide (mixing channel dimension - $220\mu m$ height and $1mm$ width). The glass slide is decorated with ciliary array consisting of four columns with alternating pumping directions. The fluid is pumped at a $10\mu l$ / min flowrate using a syringe pump.

Figure 4-6 shows experimental snapshots in which an array of cilia is used to mix two fluid streams pumped thorough the microchannel. Without any actuation of the ciliary array, two streams continue to flow nearly undisturbed along the array without intermixing, which indicates a minor effect of the diffusion on stream mixing (Figure 4-6a). As soon as the array is activated by the rotating permanent magnet, the cilia generate local flows normal to the direction of the fluid streams. Furthermore, the directions of the cilium induced flows alternate in the consecutive array columns resulting in flow circulations across the microchannel. These flow circulations have an immediate effect onto the two fluid steams by disrupting them and causing them to

penetrate each other, as shown in Figure 4-6b. After a short transient, the flow within the microchannel reaches a steady state with a nearly complete mixing of the fluorescent and non-fluorescent streams in the microchannel downstream, as shown in Figure 4-6c. In this system, the mixing time is less than the that required by diffusive mixing. Thus, the array of magnetic cilia demonstrates high potential for continuous mixing of fluids in microchannels.

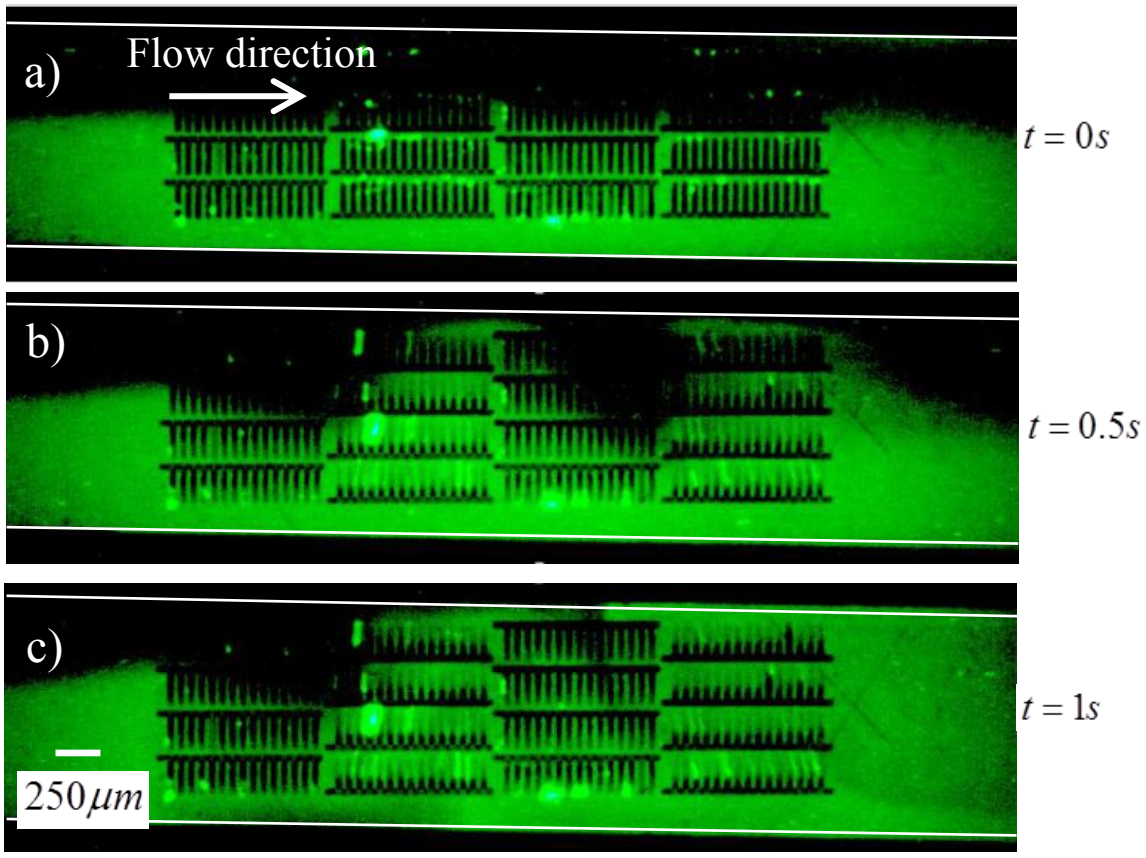

Figure 4-6: Mixing produced in a microchannel with two fluid streams. Inlet on the left shows two streams of fluid. The flowrate in the microchannel is $10\mu l / \min$. **a)** Cilia are not active, remaining flow streams unmixed. **b)** Cilia are actuated at $50Hz$ leading the merging of the two fluid streams. **c)** Steady state flow in the channel with actuated cilia results in highly mixed streams of fluid downstream. See Video 4 in ESI.

4.5 Conclusions

Fluid pumping is demonstrated by an array of beating magnetic cilia. The cilia are made of soft magnetic thin films, which are actuated by a rotating permanent magnet. Kinematics of a single cilium is examined by imaging its motion. The cilium follows different bending pattern defined by the direction of magnet rotation. The CCW rotation of the magnet produces larger spatial asymmetry in the beating pattern compared to the CW rotation of the magnet. This, in turn, results in faster pumping by cilia actuated using CCW rotating magnet. The pumping is shown to depend on a dimensionless sperm number with the fastest pumping rate occurring at $Sp \approx 2.9$ The pumping rate increases with increasing the number of ciliary rows in the array, but nearly independent from the spacing between the rows. The maximum centerline velocity generated by the magnetic cilia is $\sim 1350\,\mu m/s$, which corresponds to a volumetric flowrate of $\sim 11\,\mu l/min$. The self-pumping frequency, a metric used to assess the effectiveness of the pump based on its size, is estimated to be $\sim 2.5 min^{-1}$. This is the highest reported value in similar ciliary microfluidic pumping systems. The flowrates produced by the artificial cilia are comparable to that of natural cilia[10,84,85].

Artificial magnetic cilia such as developed in this study are promising for active control of fluid flow in microfluidic devices. For example, the transport created by magnetic cilia can be used for applications such as mixing fluid streams. The mixing of two fluid streams is demonstrated using arrays of cilia arranged such that they pump the fluid in opposite directions. It is observed that the fluid streams mix thoroughly downstream the array of cilia.

The resulted results presented in this chapter provide guidelines for designing biomimetic magnetic cilia for various lab-on-a-chip applications. Maximum flowrate can be obtained for operating conditions which result in a sperm number $Sp \sim 2.9$. The magnetic actuation has the particular advantage of being able to actuate remotely and not interfere with biological samples. Such cilia incorporated inside stents and tubes can be used for precise fluid metering. Furthermore, combining magnetic cilia with different orientations can be used for fluid mixing and probing the behavior of microorganisms in a variety of flow conditions.

Chapter 5. METACHRONAL MOTION OF ARTIFICIAL CILIA

Naturally occurring cilia do not beat simultaneously but beat in a sequential one by one fashion to actively transport fluid and suspended particles. Such sequential motion is termed metachronal motion. Metachronal motion emerges due to a phase difference between beating cycles of neighboring cilia and appears as traveling waves propagating along ciliary carpet. In this chapter, the demonstration of metachronal motion in magnetic artificial cilia is discussed. It is shown that the difference in magnetic cilium geometric properties controls the phase of the beating motion. This property is used to induce metachronal waves within a ciliary array, and the effect of various operation parameters on the wave motion are discussed. The metachronal motion in the artificial system is shown to depend on the magnetic and elastic properties of the filaments, unlike natural cilia, where metachronal motion arises due to fluid coupling. This approach enables an easy integration of metachronal magnetic cilia in lab-on-a-chip devices for enhanced fluid and particle manipulations.

5.1 Introduction

Biological organisms use organelles such as hair-like cilia to perform vital functions involving fluid manipulation in their vicinity. Each cilium performs time-irreversible motion, traversing a spatially asymmetric path, and generates local fluid transport. It is often observed that carpets of natural cilia beat in a metachronal fashion, which appear as propagating waves. For example, lung cilia beat in a metachronal fashion to facilitate the net transport of fluid and microscopic particulates.[95–97] Similar

metachronal motion is found on larger scales in the gait of millipedes, spiders and other invertebrates.[98]

In natural cilia, metachronal motion usually emerges as a self-organized phenomenon due to hydrodynamic coupling between a cilium and its neighbors.[97,99–101] As a result, tiny flexible cilia beat with a phase difference with respect to their neighbors, thereby generating travelling waves propagating along the ciliary carpet. The direction of metachronal waves in natural cilia can be symplectic (in the direction of the effective stroke), antiplectic (opposite to the direction of effective stoke), or laeoplectic (perpendicular to the direction of effective stoke).[102]

Studies point to specific advantages in the use of metachronal motion by natural cilia.[103,104] It has been reported that such motion can lead to a 3-fold increase in propulsion rate and a 10-fold increase in efficiency compared to synchronously beating cilia.[97] Metachronal beating is more energetically efficient and requires a decreased amount of adenosine triphosphate (ATP) consumed by cilia.[105] Furthermore, metachronal beating is advantageous in creating a unidirectional fluid pumping.[79] The attractive advantages offered by metachronal beating of natural cilia have motivated researchers to explore artificial analogs of ciliary carpets capable of performing metachronal motion that could be harnessed in microfluidic devices for efficient fluid transport and particle manipulation.[14,95–97,100,106]

To create metachronal motion artificially, it is essential to impose a phase difference in the beating cycles of multiple individual cilia. Such phase difference can be achieved by either applying different forcing to each cilium or by having cilia with different responses to a uniform forcing applied to the entire cilium array. The later

approach that relies on a uniform actuation is more attractive from an experimental point of view. In this chapter, methods to achieve metachronal motion using both these approaches are discussed.

5.2 Designing cilia that respond differently to the same force

Only recently a uniform magnetic force was used by Tasumori et al.[107] to demonstrate metachronal motion in an array of artificial magnetic cilia that had a different magnetic orientation. The $2mm$ cilia were created using a sophisticated fabrication method that required carefully monitored processing steps with each cilium fabricated individually. The authors intend to miniaturize their cilia to a sub-millimeter size in the future work.

This chapter discusses new approaches to create metachronal motion in an array of magnetic cilia actuated by a uniform rotating magnetic field. High-aspect-ratio magnetic filaments that are periodically deformed by a rotating magnetic field have been previously suggested as an attractive approach to create artificial beating cilia (see Chapter 2,Chapter 3Chapter 4).[108] Cilia that are made up of paramagnetic metallic filaments with identical magnetic properties are used.[62,63,109] The motion of such cilia in a rotating magnetic field is defined by magnetic, elastic, and viscous hydrodynamic forces. The counter-clockwise rotating magnetic field bends the elastic cilium during the forward stroke, during which elastic energy is accumulated. After reaching maximum bending, cilia recover to the initial position by releasing the accumulated elastic energy. At relatively low actuation frequencies, the forward stroke is governed by a balance of the

magnetic and elastic forces, whereas the recovery stroke is controlled by an interplay of the elastic and viscous forces.[62]

Metachronal wave motion in a ciliary array emerges when there is a phase difference in beating strokes of neighboring cilia, such that neighboring cilia transition from the forward to the recovery stroke in a sequential manner. In this system, the transition happens when the elastic force in deformed cilia exceeds the magnetic force due to the rotating magnet. More flexible cilia deflect more easily by the magnetic field[108,110] and, therefore, transition to the recovery at larger rotational angles of the magnet compared to stiffer cilia with the same magnetic properties. This leads to a phase difference between the beating of more flexible and less flexible magnetic cilia. This property is used to fabricate an array of cilia that exhibit metachronal motion under uniform rotating magnetic field.[110]

Consider elastic cilia that are made of a paramagnetic material. In this case, the ratio between magnetic and elastic forces acting on a cilium can be characterized by a magnetic number, as discussed in chapter 3. Note that in the above definition of Mn, W cancels out and, therefore, Mn is independent of cilium width. To achieve metachronal motion, the magnet angle at which cilia transition is changed from forward to recovery stroke and, therefore, the phase of cilium beating, by altering the magnitude of Mn for individual filaments in a ciliary array. To change the Mn for across an array of cilia, geometric properties such as the length or thickness of the filaments can be varied. Note that Mn is independent of cilium width, as W cancels out in the definition. In the following sections, the metachronal motion obtained by varying the length as well as the thickness of the filaments is discussed.

5.2.1 Varying length across the array

Since Mn linearly depends on the cilium length L, a linear change of cilium length should lead to a metachronal wave propagating along the ciliary array with a constant speed.[110] To test this hypothesis, an array with cilium length increasing linearly with the cilium position along the array was fabricated.

An array of nickel iron permalloy cilia is fabricated using the technique discussed in chapter 2 with cilium length increasing from $60\mu m$ to $600\mu m$. The cilia are $10\mu m$ in width, and $60nm$ in thickness. The separation between neighboring cilia within a row is $50\mu m$, unless indicated otherwise. Details of the fabrication process and imaging procedure can be found elsewhere (See Chapter 2, Chapter 3 and Chapter 4).[63] The cilia are actuated by a permanent magnet with a $12mm$ diameter (D8X0DIA, KJ Magnetics) rotating with a constant frequency f. The large size of the magnet compared to the ciliary array ensures a uniform magnetic field experienced by cilia. A schematic of the experimental setup is shown in Figure 5-1.

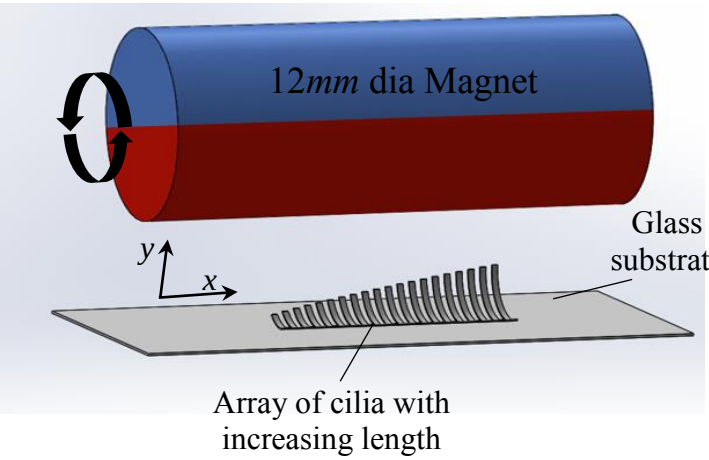

Figure 5-1: Schematic of the experimental setup with an array of cilia with linearly varying lengths actuated by a permanent magnet rotating,

Figure 5-2a, b, and c show snapshots of the ciliary array at different times during the magnet rotation. The snapshots illustrate the propagation of a metachronal wave along the array (also see Video 5 in ESI). The front of the metachronal wave are identified by the position of the cilia within the array that have just completed the recovery stroke, as indicated by the arrows in Figure 5-2a, b, and c. It is found that the metachronal wave propagates from the shorter cilia on the left to the longer cilia on the right with a nearly constant speed. This is indicated by the linearly increasing position of the wave front with time T (Figure 5-3). Note that front position X is normalized by total length of the array L_A.

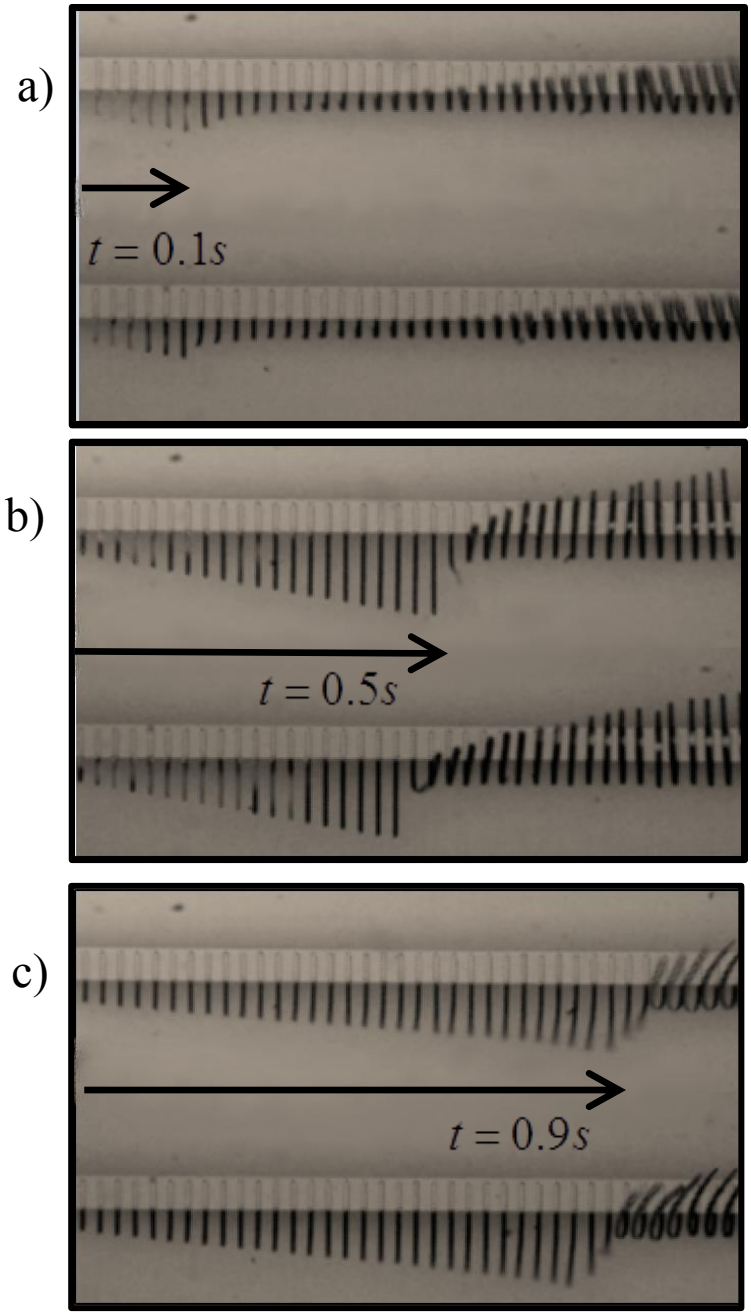

Figure 5-2: **a-c)** Snapshots of the ciliary array at time $T = 0.1$, $T = 0.25$, and $T = 0.45$, respectively. Two rows of cilia are shown with cilium - $10\mu m$ in width and length changing form $60\mu m$ to $600\mu m$. The magnet is rotated counter clockwise with a frequency of $0.5Hz$. Metachronal motion can be viewed from left to right from below the glass substrate, with the wave front indicated by the arrow. See ESI for Video 5 of metachronal wave motion in ciliary arrays.

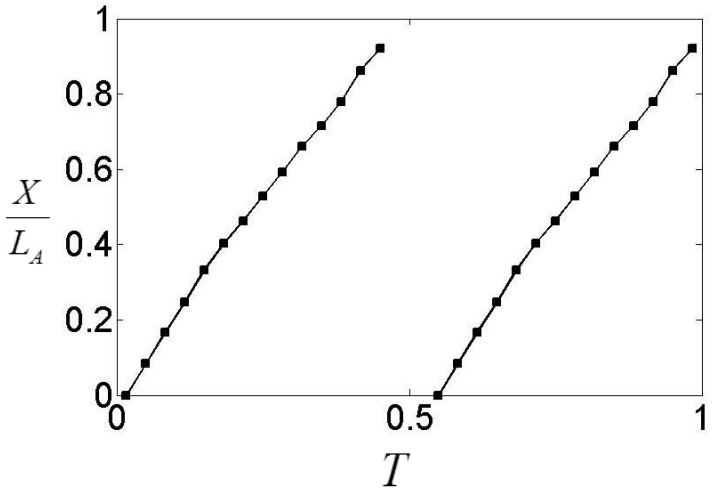

Figure 5-3: Position of the metachronal wave front $\chi = X/L_A$, where L_A is the array length, as a function of time T. Time T is normalized by the period of magnet rotation (T_o).

To further understand how the metachronal beating is created in the ciliary array, the kinematics of two beating cilia with different length are examined. Figure 5-4a and b present a series of overlapped images of cilia with length $L = 220\mu m$ and $L = 480\mu m$, respectively. In both cases, cilium tips follow closed trajectories shown by a yellow line during the forward stroke and by a red line during the recovery stroke.

The forward stroke starts at position *P1*. For both the cilia, the tip angle, indicated by the green arrow, is closely aligned with the direction of the magnetic field, indicated by the blue arrow. The CCW rotating field induces a magnetic moment that bends the cilia in the counter-clockwise direction. The cilium tip angle increases and reaches a maximum at position *P2*. At this position of the maximum bending, the elastic

force due to cilium deformation exceeds the magnetic force causing the beginning of the recovery stroke. Position $P2$ is determined by the value of Mn. Shorter cilia with larger stiffness, and therefore a lower Mn, bend to a lesser extent (Figure 5-4a), whereas longer cilia with lower stiffness and higher Mn are capable of bending to larger angles to follow the field (Figure 5-4b). Thus, the maximum bending angle at position $P2$ is greater for the longer cilia that are characterized by higher values of Mn.

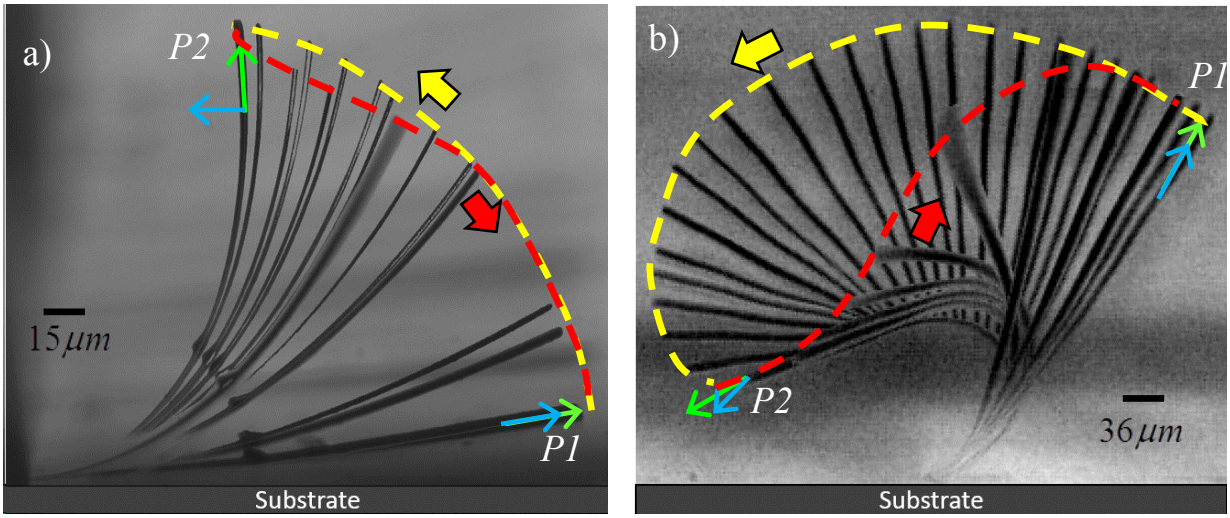

Figure 5-4: Motion of a single cilium in a beating cycle with length **a)** $L = 200\mu m$ and **b)** $L = 480\mu m$ The yellow and red arrows indicate the forward and recovery strokes, respectively. The green arrow is tangent to the cilium tip and the blue arrow indicates the direction of the magnetic field.

At position $P2$, the angle between the cilium tip and magnetic field is larger for the shorter cilium compared to the longer cilium, as indicated by the angle between the red and blue arrows in Figure 5-4. Further rotation of the magnet beyond $P2$ reduces the magnetic moment and the cilia return to position $P1$ releasing the accumulated elastic energy. The shorter cilium returns to $P1$ at a smaller magnet angle than the longer cilium

leading to a phase difference in the beating cycle that is proportional to the cilium length. Note that magnetization of the cilia flips its direction during the recovery stroke. As a result, cilia perform two beating cycles for each rotation of the magnetic field.[63,68,70]

Such a phase difference in the motion of cilia of different lengths can be extended to multiple cilia of different lengths and a phase difference between their motions can be obtained. Figure 5-5a shows the normalized tip trajectory of four cilium of lengths $L = 200, 300, 400, 600 \mu m$. These $x - y$ positions are normalized using the length (L) of the cilium. The shortest cilium has the largest bending rigidity, and therefore the magnetic moments can only bend the cilium to a smaller angle. The tip trajectory for the shortest cilium is shown in blue. Note, that the shortest cilium oscillates between points that subtend an angle shown in blue. As the length of the cilium increases, the bending rigidity reduced, and the magnetic field is capable of bending the cilium to a larger angle. This is indicated by the green, red, and black tip trajectories, which correspond to lengths $L = 300, 400, 600 \mu m$ respectively. The angle subtended by the beating cycle for longer cilium shifts counter-clockwise as shown by the green, red and black angles respectively. This shift in the angle subtended by the beating cycles leads to the phase difference in their oscillations.

The phase offset in the motion of different length cilia is illustrated in Figure 5-5b. Here, the normalized tip angle θ is plotted as a function of time T. Tip angle θ is measured with respect to the substrate in the counter-clockwise direction. Time T is normalized by period of the magnetic field. The increasing value of θ indicates the forward stroke, whereas the decreasing θ represents the recovery stroke. The angle of the magnetic field θ_M is indicated by the tilted dotted lines.

The forward stroke starts when the direction of the magnetic field θ_M coincides with the tip angle θ. This happens at different T for cilia with different length, with shorter cilia initiating the forward stroke earlier than longer cilia. The tip angle increases nearly linearly with T until the maximum is reached. As cilia deform, the difference between the cilia tip angle θ and the direction of magnetic fields θ_M increases, indicating the lag in cilium tip angle with respect to the magnet. This difference is larger for shorter cilia which are effectively stiffer. The maximum θ coincides the beginning of the recovery stroke, which starts earlier for shorter cilia. During the recovery stroke, θ decreases until it matches the direction of the magnetic field and then the cycle repeats. Thus, cilia of different length perform cyclic motion with period matching the half period of the magnet rotation, but with different phases with respect to the rotation of the magnetic field. The phase is proportional to the effective bending elasticity of the cilia and, thus, depends on the magnitude of the magnetic number Mn. Remember, $Mn = BL\left(WP/\mu_0 EI\right)^{0.5}$ represents the ratio between the magnetic force and the elastic forces that is proportional to the cilium length. As a result, a metachronal wave emerges that propagates in the direction of the increasing cilium length (see Video 6 in ESI that shows two metachronal waves simultaneously propagating in opposing directions within a ciliary array with different cilium lengths).

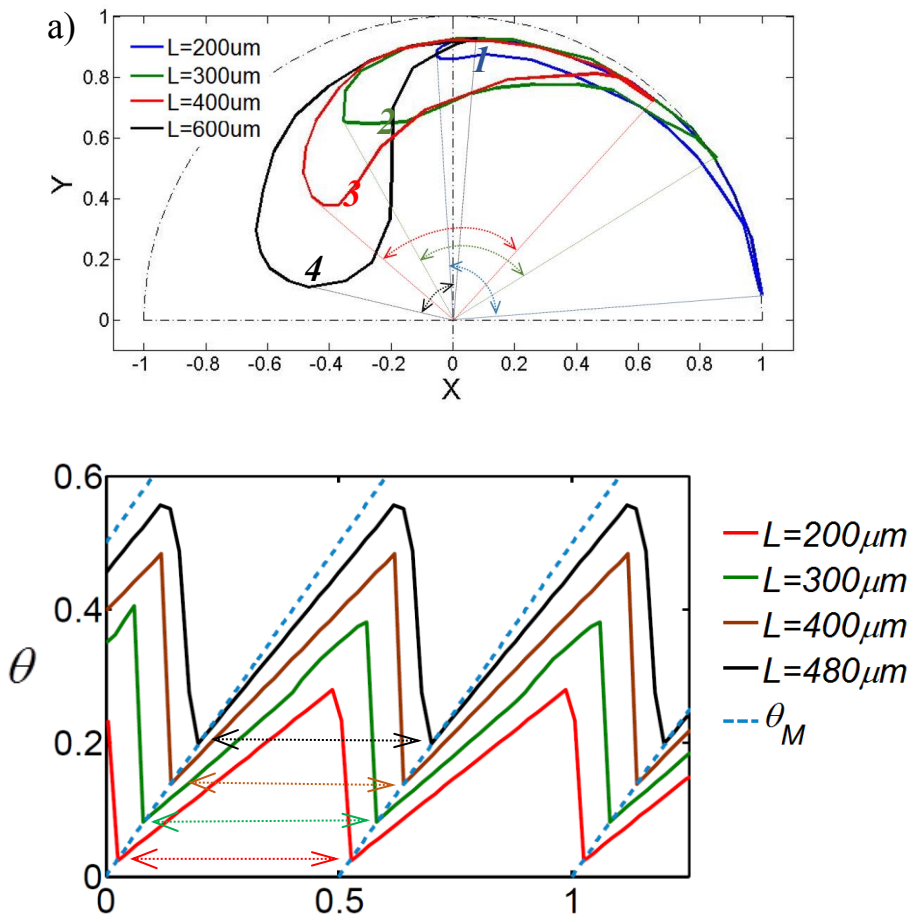

Figure 5-5: **a**) Plot of normalized trajectory of cilium tip of different lengths obtained through recording the beating pattern in the side view. **b**) The tip angle of beating cilia as a function of time T. The dotted lines show the rotational angle of the magnetic field. The angles are measured with respect to the substrate and are normalized by 2π. Time is normalized by the period of the external magnetic field rotation equal to $2s$.

The sperm number Sp characterizes the ratio of viscous to elastic forces acting on cilia. To further explore the effect of Sp and Mn on metachronal waves, experiments were conducted in which both these dimensionless parameters are varied in the ranges from 0 to 6.5 and from 0 to 4.9, respectively. Since, Sp and Mn are both proportional to

L, their magnitudes change along the ciliary arrays. It therefore, introduces dimensional parameters $Sp_L = Sp/L$ and $Mn_L = Mn/L$ to describe the operating condition for the entire array. In the experiments, Sp_L is varied by changing the magnet frequency, whereas Mn_L is changed by altering the distance from the array to the magnet. Note that Sp_L and Mn_L have the unit of m^{-1}

To characterize the metachronal motion, the time T_c is measured at which a cilium returns to $P1$ completing a beating cycle (see Figure 5-4). In Figure 5-5, T_c is plotted as a function of the normalized cilium position $\chi = X/L_A$, where X is the cilium position within the array and $L_A = 3mm$ is the length of the array. The results are presented for selected values of Sp_L and Mn_L. Figure 3 shows that T_c increases nearly linearly with χ along the array indicating the propagation of a metachronal wave with a constant speed. Furthermore, the inverse of T_c slope represents the wave speed.

It is found in Figure 5-6 that all the data for T_c collapses into two curves corresponding to the two values of Mn_L tested in these experiments. The results are independent of Sp_L confirming that the metachronal wave motion is solely defined by Mn_L that sets the speed of the wave propagation. A lower value of Mn_L results in a faster wave speed. Indeed, weaker magnetic field can deform cilia to a smaller angle triggering an earlier transition to the recovery stroke. Therefore, T_c decreases with decreasing Mn_L.

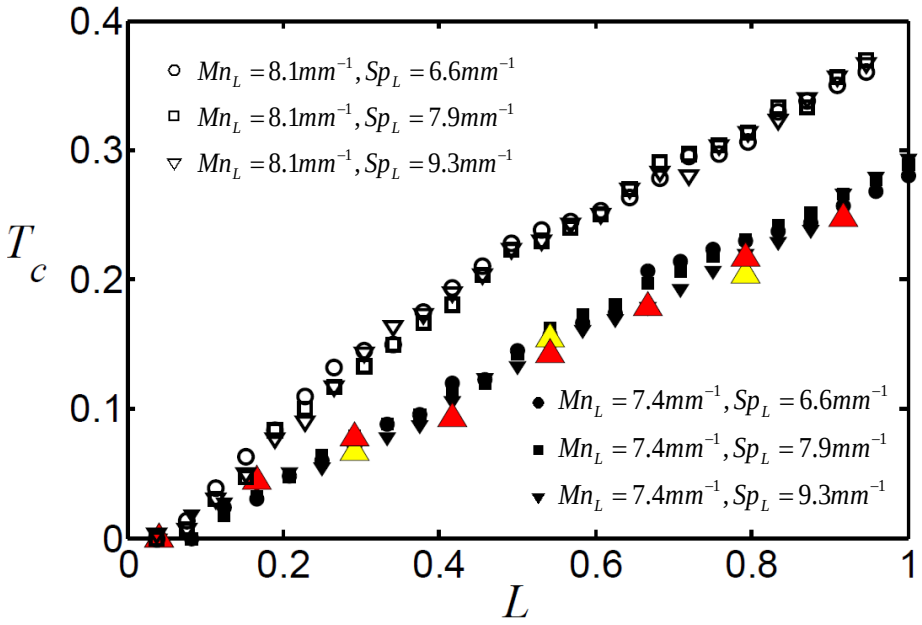

Figure 5-6: Cycle completion time T_c as a function of cilium position χ for various experimental conditions. Note that data points collapse onto separate curves depending on Mn_L, indicating the weak dependence on Sp_L. The symbols ▲ and ▲ represent data obtained for $Mn_L = 7.4mm^{-1}$, $Sp_L = 6.6mm^{-1}$ from arrays with $150\mu m$ and $300\mu m$ spacing between cilia, respectively.

In naturally occurring cilia, metachronal motion emerges as a result of hydrodynamic coupling between neighboring cilia.[97,99–101] To probe the effect of hydrodynamic interactions between neighboring cilia in the synthetic system, experiments were conducted with ciliary arrays having different distances between cilia within a row. Specifically, f arrays of cilia are fabricated with 3 and 6 times greater spacing between the neighboring filaments as compared to the original arrays. The results for T_c obtained in these experiments are indicated in Figure 5-6 by the colored symbols. It is found that spacing between cilia does not affect metachronal wave propagation.

Thus, in the artificial ciliary system, metachronal motion is solely controlled by the interplay between magnetic and elastic forces, and not due to hydrodynamic coupling.

Further, in Figure 5-7, T_c is plotted as a function of Mn and it is noted that the all the data points for different lengths, frequencies and magnetic field strength collapse one to a single curve. This implies that T_c is influenced only by the relative scale of magnetic to elastic forces, i.e. magnetic number, and is insensitive to the viscous forces acting on the cilia.

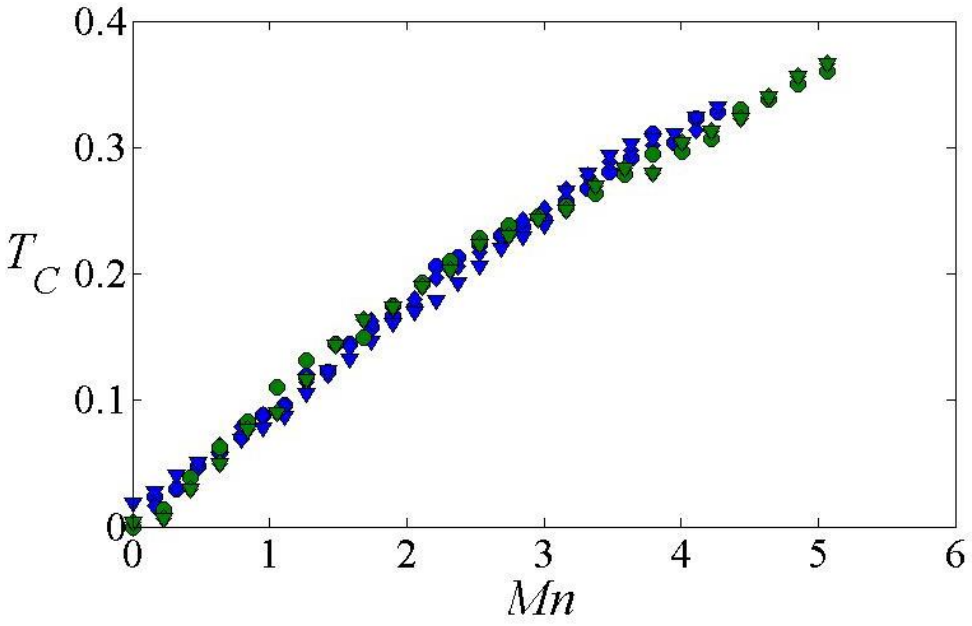

Figure 5-7: T_c as a function of Mn for cilia of various lengths.

5.2.2 Varying thickness across the array

Mn can also be changed across the array of cilia by varying other parameters such as the thickness. Mn is proportional to P^{-1}, and by varying the thickness across the

array, a phase difference between the successive cilia is expected. To test this, cilia with increasing thickness across the array are fabricated.

To achieve a thickness gradient across the array, a shadow is used to partially cover the features during the NiFe sputtering process. Figure 5-8a shows a schematic of partially shadowing the features in a sputtering machine. A glass slide is placed at 1mm from the substrate and partially covers the lithographically patterned features. Sputtering the metal on such a setup leads to deposition of metal with increasing thickness. The film thickness gradually decreases in the shadow region shown in Figure 5-8a. With this, cilia obtained are increasing in thickness across the array, with thickness varying between 20nm and 100nm. Figure 5-8b shows the thickness of cilia measured across the array fabricated using this method. Dektak 150 surface profilometer was used for this measurement.

When subject to a uniform rotating magnetic field, the cilia are actuated with a phase difference. Figure 5-8c shows snapshots at three different times during which the cilia are actuated one after the other in a sequential manner (See Video 7 in ESI). The metachronal motion propagates from left to right with thick cilia completing the cycle first, followed by the thinner ones as indicated by the red arrows.

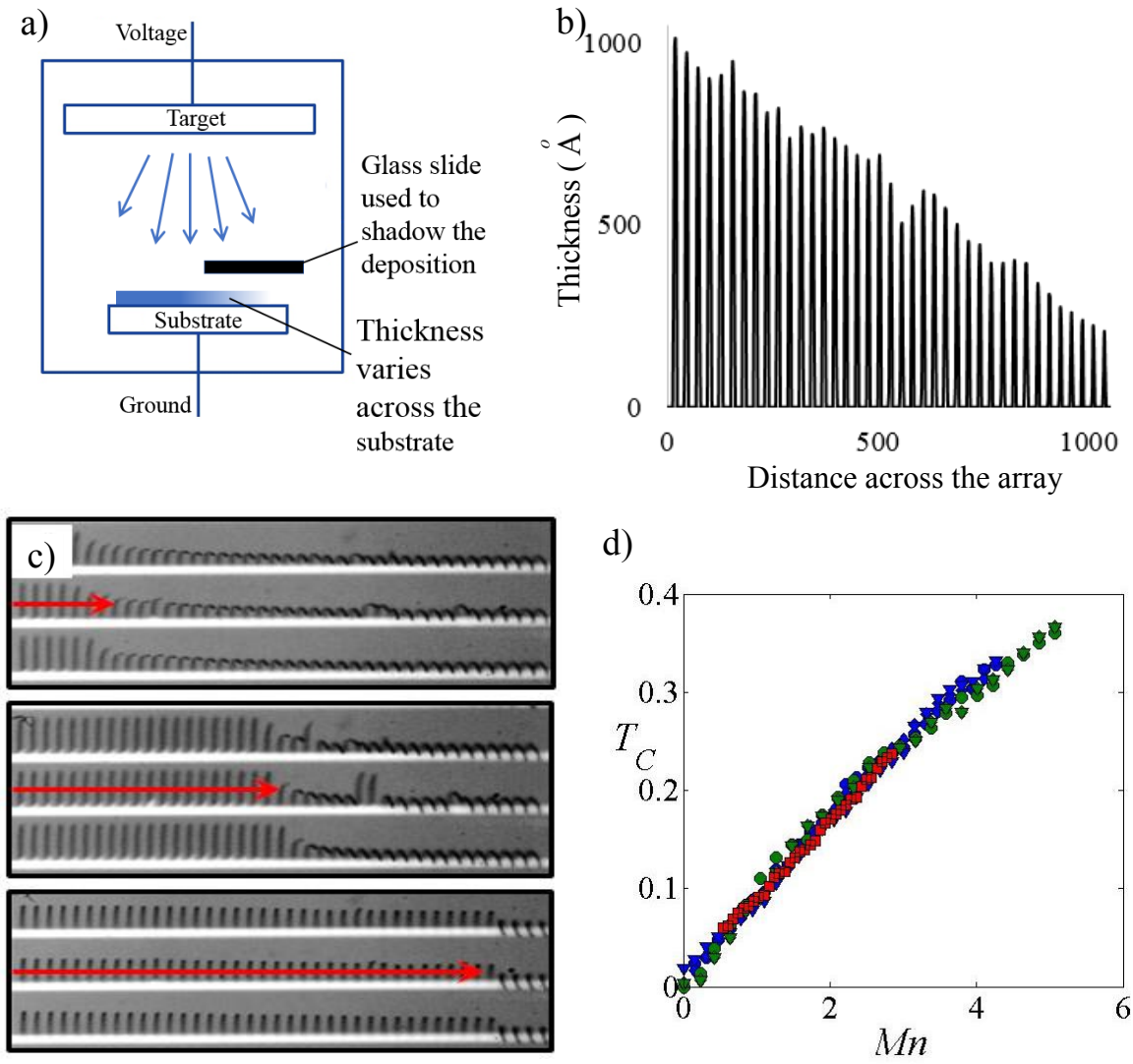

Figure 5-8: a) Schematic of the shadow setup used to fabricate cilia of increasing thickness. **b**) Measured thickness across a row of cilia. **c**) Snapshots at different instances of time as the metachronal motion propagates from left to right across the row of cilia. Red arrows indicate the position of the wave front. **d**) Cycle completion time T_c as a function of Mn for various cilia of different lengths and thicknesses.

As discussed in the previous section 5.2.1, the time at which cilium completes the cycle is solely dependent on the Mn. Recollect that Mn describes the balance between magnetic and elastic forces. Figure 8d is an over lay of the data points obtained for cilia

of varying thickness on the previously reported Figure 5-8. T_c is plotted as a function of Mn for cilia with different thickness, length, and frequency of oscillation. The red square points in the plot represent the points obtained for cilia of varying thickness. Note that all the data points collapse on to a single curve, which emphasizes that T_c solely depends on Mn.

In both the implementations discussed in the previous sections, the metachronal motion is perpendicular to the direction of the effective cilium stroke (i.e. laeoplectic). Such laeoplectic metachronal motion has been shown to produce secondary flows with a net fluid flux perpendicular to the beating plane.[69] It is note that by changing the spatial arrangement of cilia on the substrate such that cilia with different Mn are placed in front or behind of each other, either symplectic or antiplectic motion can be achieved. It has been shown that for antiplectic metachrony, the net flow generated by cilia is greater, whereas symplectic metachronal beating leads to a flow that is slower in comparison to synchronously beating cilia.[69] Furthermore, in the experiments demonstrated here, the phase difference is a direct consequence of the difference in kinematics of the cilia across the array. The asymmetric stroke pattern for each cilium is slightly different and therefore the pumping produced by each cilium can be expected to be different. The over all fluid flow produced by such an array is the combined effect of metachronal beating as well as the differences in asymmetric strokes. An example of such a flow pattern is shown in Figure 5-9. This figure shows flow produced by cilia with increasing lengths away from the center. Note that the circulation produced is denoted by the red arrows. Again, this flow pattern arises due to the metachronal effect as well as the differences in beating pattern of the different cilia. The coupling of cilia phase difference and the beating

pattern can be a limitation for isolating and purely studying the effect of metachronal motion on fluid pumping.

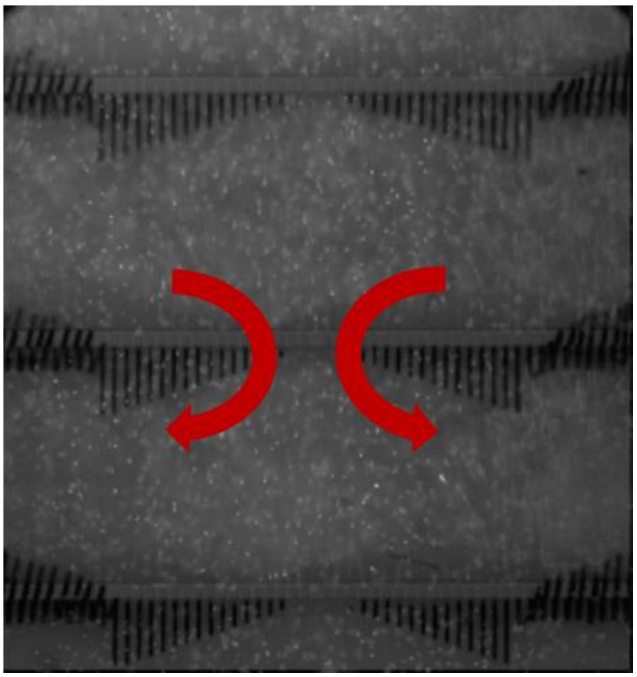

Figure 5-9: Flow produced by an array of cilia with varying cilium lengths. The fluid motion is the combined effect of metachronal motion and differences in kinematics due to changing lengths.

5.2.3 Varying width across the array

Recollecting the definition of magnetic number with $Mn = BL\left(WP/\mu_0 EI\right)^{0.5}$, note that Mn depends on cilium length and thickness, but is independent of the cilium width W. The width that appears in the numerator is cancelled by the width that appears in the moment of inertia I. Therefore, an array of cilia with identical length and thickness, but varying widths is expected to show no metachronal behavior. To test this hypothesis and validate the scaling of Mn, an array of cilia with increasing cilium width is fabricated

and subject it to a uniform rotating magnetic field. The setup used for this experiment is similar to the one shown in Figure 5-1. The cilium width in this array varies from $40\mu m$ on the left to 4um on the right. Indeed, the experiments reveal that cilia of different widths beat synchronously with no phase difference in their cycles. Figure 5-10 shows two snapshots of the synchronous beating cilia of different widths at different instances of time (See Video 8 in ESI for complete motion). Furthermore, the synchronized beating of cilia of different widths validates that Mn is independent of cilium width.

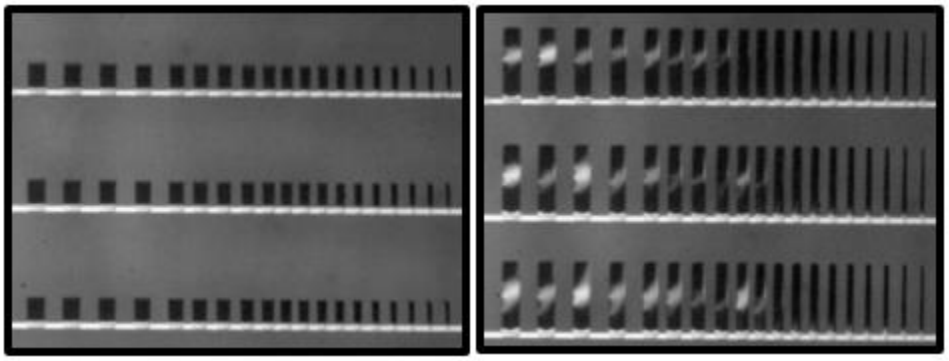

Figure 5-10: Array of cilia with varying cilium widths beat synchronously with no metachronal motion when actuated by a rotating magnetic field. $L = 200\mu m$, $W = 4\mu m - 40\mu m$.

5.3 Applying different forcing to each cilium

As mentioned in the previous sections metachronal motion can also be obtained by applying different forcing on each cilium. In the following sections two methods are discussed which achieve this outcome.

5.3.1 Translating the magnet

Translating the magnet across a large array of cilia such that the cilia in the different locations experience the magnetic field at different times, can actuate the cilia metachronally. For example, consider the schematic shown in Figure 5-11 showing a permanent magnet that is translated over an array of cilia consisting of multiple rows. Note the orientation of the permanent magnet and the direction of translation. Only the cilia directly under the influence of the magnet are actuated, while the others are not actuated. As the magnet moves in the direction indicated by the arrow, the direction of magnetic field as experienced by the rows of cilia changes.

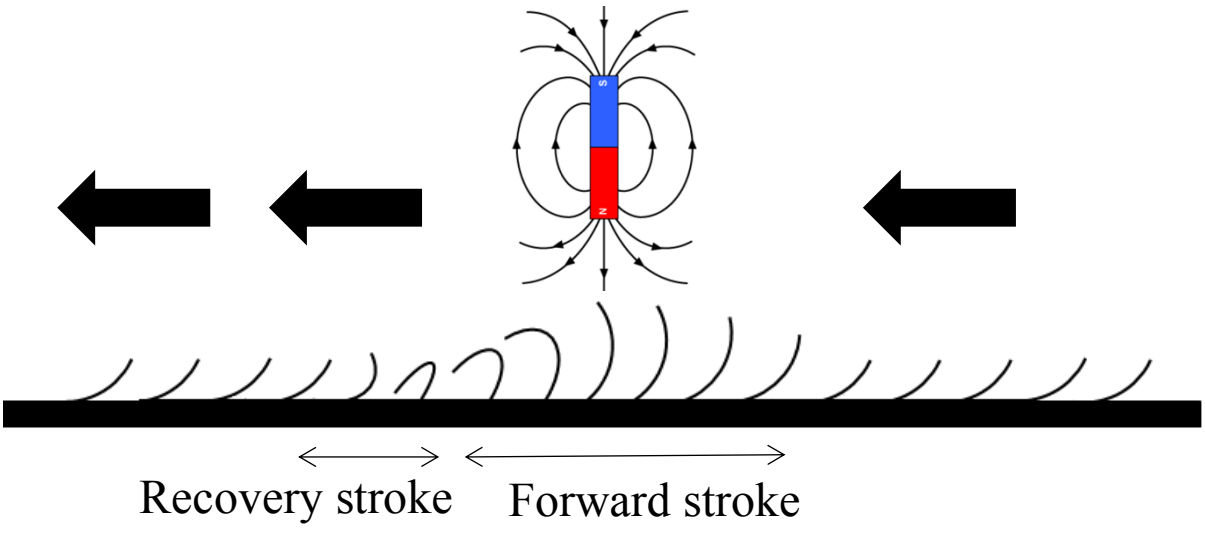

Figure 5-11: Schematic of the experiment with magnet translating along an array of cilia. The cilia are actuated from right to left in a sequential manner as the magnet translates.

As the magnet is moved from right to left, the cilia on the right are actuated first as they are closer to the magnet. The cilia start with the forward stroke in which they bend away from the substrate to orient along the direction of the magnetic field. When the magnet is directly above the cilia, the field is perpendicular to the substrate and the tip of the cilia underneath the magnet is expected to be perpendicular as well. As the magnet moves past a row of cilia, the bending for the row of cilia increases to a maximum after which they return to their initial position when the magnet is sufficiently far away. The moving magnet ensure that the cilia are actuated in a sequential manner leading to metachronal motion.

Unlike cilia under the influence of a uniform rotating magnetic field discussed in the previous section, these cilia are subjected to a magnetic field that is changing both in direction and magnitude. Therefore, the kinematics of beating and the asymmetric stroke pattern for such a system is expected to be different. Figure 5-12 shows the snapshots of the propagation of a metachronal wave in a large array of cilia subjected to a magnet that translates along the array. The magnet is initially positioned at the bottom of the array and translates along the direction of the array (shown in red). All cilia in a row experience the same magnetic force. Observe the sequential actuation of the cilia, one row after another as the magnet translates.

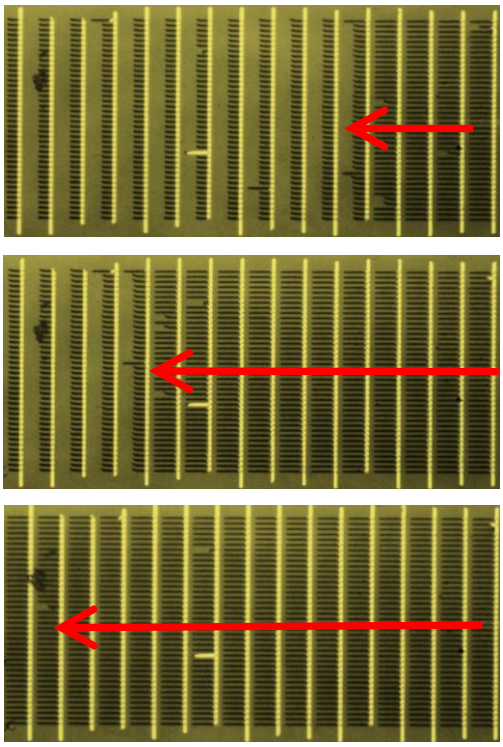

Figure 5-12: Metachronal motion in an array of cilia due to a magnet translating along the direction of the array. Cilium properties $L = 80\mu m$, $W = 8\mu m$, $P = 60nm$.

5.3.2 Rotating a magnet that is offset from the array center

Another method of actuating magnetic cilia metachronally is by translating the magnet diagonally across the array. Figure 5-13a shows an example of such a motion where a magnet is moved diagonally across a row of cilia. The movement along the direction of the array causes the cilia to perform the oscillations. These oscillations due to the magnet moving along the direction of the array is similar to the ones described in the previous section 5.3.1. The lateral motion, perpendicular to the direction of the array, actuates them in a sequential fashion. In the example schematic shown in Figure 5-13a, the magnet translates from the bottom left to the top right of the array. With this setup it

is expected that the cilia on the left of the array are actuated first, followed by the ones on the right. Note that the magnet has a magnetization perpendicular to the plane of view. Further, moving a magnet diagonally across the ciliary array is simpler to implement experimentally, with a permanent magnet simply rotated about point X, that is offset from the array (shown in the Figure 5-13a). Figure 5-13b shows the snapshots at different times during the actuation of the cilia, where the magnet is moved diagonally. The ones on the left are actuated first, followed successively by the ones on the right. The propagation of the wave front is indicated by the red arrows.

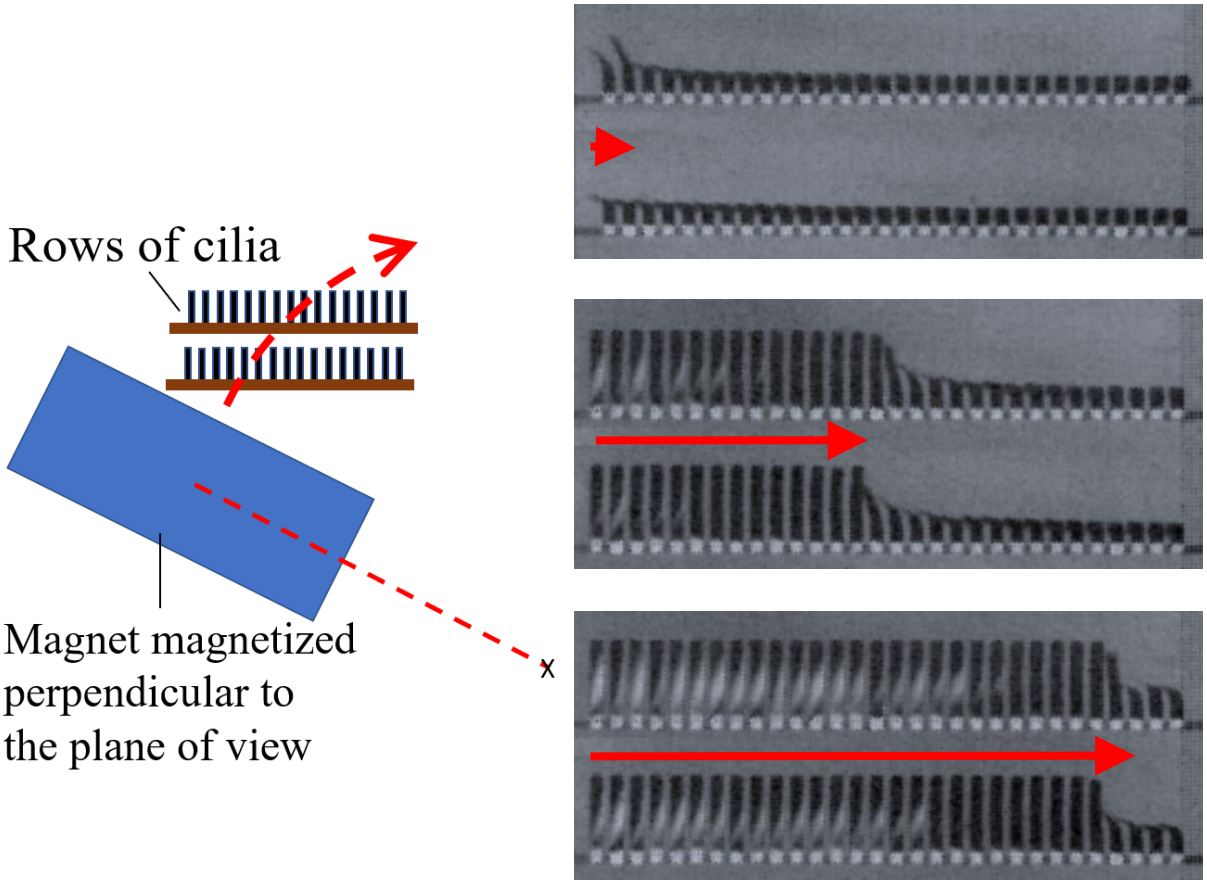

Figure 5-13: **a**) Schematic of the experimental setup with the magnet moved diagonally across an array. **b**) Snapshots at different times showing the propagation of the metachronal wave from left to right (See Video 9 in ESI).

In both the implementation demonstrate in sections 5.3.1 and 5.3.2, each cilium experiences the same magnetic field as the magnet translates, but at different instances of time. This leads to the same beating pattern for all the cilia. Furthermore, the propagating wave speed is determined by the speed of the translating magnet. The orientation and direction of translation can be controlled to obtain different types of metachrony.

5.4 Summary

Naturally occurring cilia are known to beat in a sequential metachronal motion to achieve fluid transport. This motion sequential motion is similar to a "Mexican wave" commonly seen in football games. It is also understood that the such motion provides additional advantages over synchronized beating of the cilia for achieving fluid transport. In this chapter, artificial magnetic cilia capable of performing metachronal motion is demonstrated. Array of magnetic cilia described in Chapter 2,Chapter 3 can be actuated, such that there is a phase difference in the beating cycles of individual cilium, which leads to sequential one by one actuation. This motion appears as travelling waves across a ciliary array. Phase difference in the actuation can be obtained by either changing properties of cilia, such that they respond differently to the same force, or by applying a different force on each cilium.

First, metachronal motion is demonstrate by varying cilium properties across the array, such that individual cilia respond differently for the same applied magnetic field. The transition of a cilium from forward stroke to recovery stroke depends on the ratio between the magnetic and elastic forces, which is characterized by the magnetic number. A phase difference in the beating cycles can be obtained by changing the magnetic number across the ciliary array. This enables their actuation with a phase difference and

leads to metachronal motion. Length and thickness are changed to create gradients in magnetic number across the array. The experiments reveal the sequential actuation forming metachronal motion. Furthermore, it is demonstrated that the metachronal wave speed is insensitive to the viscous dissipation forces, and only depends on the balance between magnetic and elastic force (the magnetic number - Mn).

Metachronal actuation can also be achieved by applying a magnetic force at different instances of time for each cilium in the array. A couple of methods are discussed to achieve this experimentally. The translation of the magnet determines the direction and speed of the travelling wave. Laeoplectic, antiplectic and symplectic metachrony can be obtained by controlling the orientation and direction of magnet travel. Again, the wave speed is insensitive to the fluid viscosity, and unaffected by the motion of neighboring cilia.

In conclusion, many approaches are demonstrated to create metachronal waves in an array of artificial cilia submerged in a viscous fluid and actuated by a uniform rotating or translating magnetic field. The fabrication approach enables creation of large arrays of microscopic magnetic cilia that can be readily integrated into various microfluidic devices. This in turn will facilitate the development of attractive biomimetic platforms that use metachronal cilia motion for fluid and particle manipulation.

Chapter 6. INDIVIDUAL CONTROL OF CILIA

In Chapter 4, a rotating magnetic field was used to actuate the cilia, which led to simultaneous actuation of all the individual filaments. A phase difference in their motion was demonstrate by varying cilium properties across the array, and metachronal-beating cilia was discussed in Chapter 5. In all these cases of purely magnetic actuation, all the cilia in an array are actuated together. It is not possible to selectively actuate only a few filaments, while the others remain stationary. In other words, it is not possible to individually control the actuation of the cilia. In this chapter, controlling the motion of individual cilia as an electrostatic actuator is proposed. An electrostatic force is applied in addition to the magnetic force on the cilia. If the magnitude of the electrostatic force is larger than the magnetic forcing, and therefore, the cilia do not respond to the magnetic actuation. Moreover, the electrostatic force can be applied only on individual filaments, which allows for selective beating of the cilia.

Toonder et al. have shown the use of purely electrostatically actuated filaments as artificial cilia[91]. Typical applications of parallel plate electrostatic actuation for out-of-plane motion include a variety of devices, such as micro-relays[111], optical switches[112] and many others[113]. Voltage control and charge control are the two general methods in for controlling the deflection of the filaments. In this chapter, voltage is controlled to immobilize the ciliary filaments on the substrate.

The proposed method for electrostatic actuation uses a bottom gold electrode that is embedded in a layer of silicon dioxide dielectric layer, and the NiFe filaments act as the top electrodes. A schematic of the actuator is shown in Figure 6-1. In a voltage

controlled electrostatic actuator, the electrostatic force is proportional to the inverse square of the separation distance. At small voltages, the electrostatic voltage is countered by the spring force, and the separation distance reduces with increasing voltage. After a certain "pull-in" voltage is reached, the electrostatic forces increase more than the elastic restoring forces, making the actuator unstable and the plates snap together[114–118]. In the implementation discussed in this chapter for immobilizing the cilia on the substrate, the voltage applied was always maintained about the pull-in voltage. This led to a situation in which the filaments and bottom electrode snap together when the voltage is turned on. Furthermore, the layout of the bottom electrode can be designed to only immobilize a certain number of cilia when the voltage is applied.

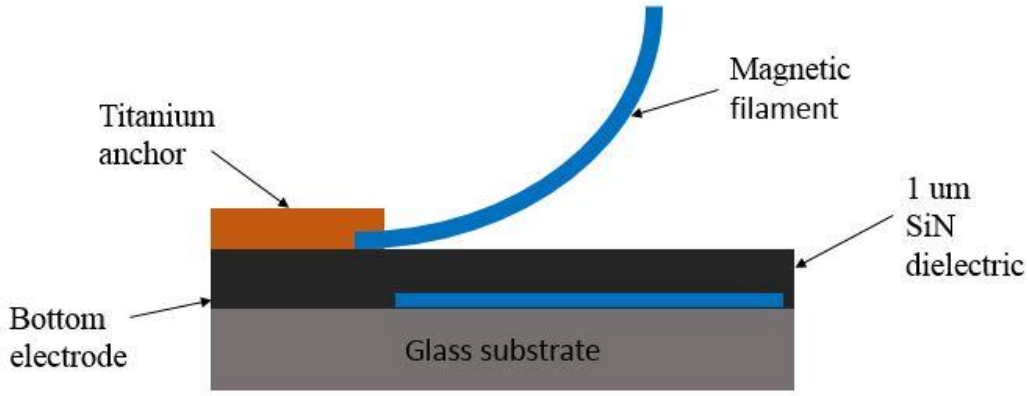

Figure 6-1: Schematic of electrostatic actuation of the cilia. A patterned layer of gold is used as the bottom electrode, and the cilia act as the top electrode.

6.1 Fabrication

The implementation of electrostatic actuation requires additional processing to incorporate a bottom electrode in the microfabrication process. First, the pattern of the bottom electrode is lithographically printed on the glass substrate and a 100nm layer of gold is deposited. Excess gold is removed by performing a lift off. Then, a dielectric layer of silicon nitride (SiN – 0.5um) and silicon dioxide (SiO_2) is grown using plasma enhanced chemical vapor deposition - PECVD process (Unaxis PECVD). Once the dielectric layer is deposited, the rest of the processing is similar to fabrication described in Chapter 2. The pattern of the cilia is imprinted using a negative photoresist (NR9 1500Py Futurex) on a glass substrate. A 40nm sacrificial layer of copper is then sputtered (Unifilm sputterer) followed by a layer of NiFe (80:20 Ni:Fe permalloy) of required thickness. Lift-off is done to remove the photoresist by dissolving it in acetone, which leaves the cilia features on the surface. The next step is to deposit an anchor for holding the cilia on the substrate. A second lithographic step is performed to obtain these features which are deposited with 150nm of titanium. This anchor layer sticks to the glass and ensures the NiFe cilia are held on the substrate. The anchor is also used to connect the cilia to the terminal of the voltage source. Electrical leads were wire-bonded from the bottom and top electrode contact pads, which in turn was connected to the voltage source. A flow chart of fabricating the electrostatic actuated cilia is shown in Figure 6-2.

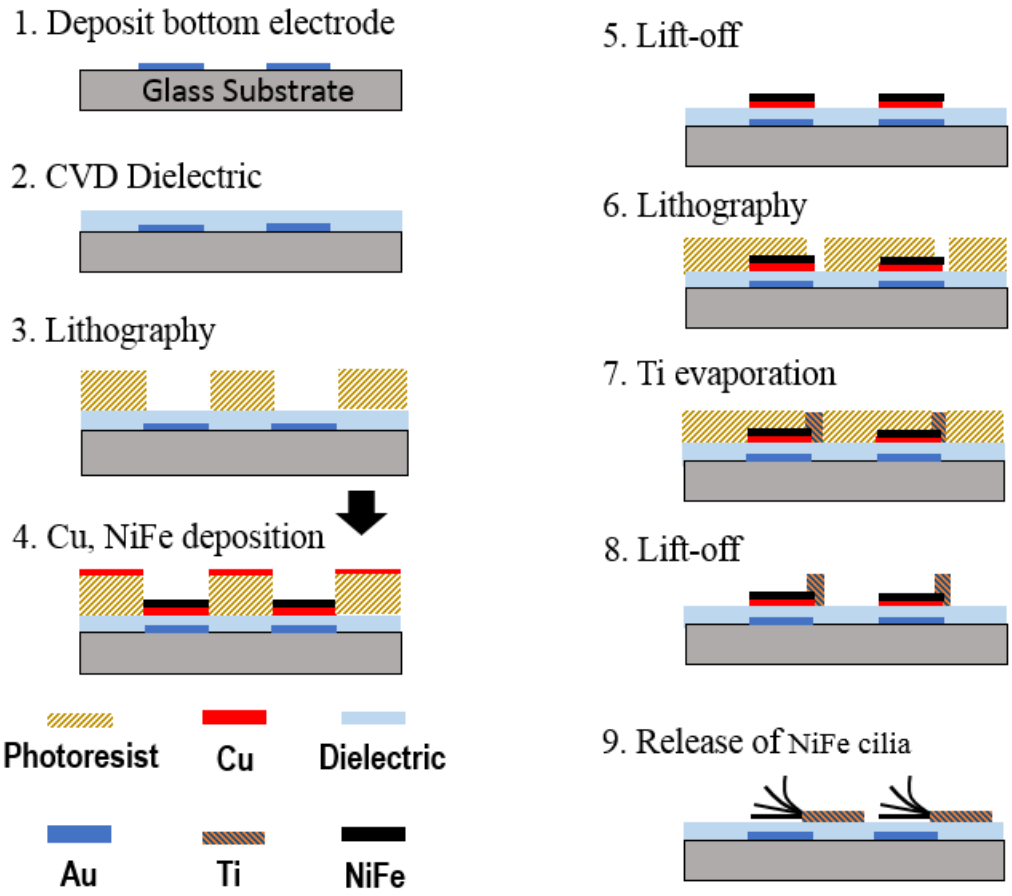

Figure 6-2: Flow chart showing the fabrication process for electrostatically actuated cilia.

6.2 Operation

Theoretically, a DC voltage can be applied on the plates of the actuator. Applying a DC bias however, led to a lot of bubble generation due to electrolysis at the electrodes. Therefore, a high frequency AC voltage was applied across the plates with a frequency of 400kHz. The high frequency voltage supply ensures minimum gas generation even in a buffer solution (1X PBS). A signal generator connected to a 20x voltage amplifier was used to maintain a constant AC voltage across the terminals of the actuator.

6.2.1 Static magnetic field:

A fixed magnetic field was applied to initially orient the filament perpendicular to the substrate. Voltage was then increased from 0V to 60V and the deflection of the filaments was observed. Figure 6-3 shows the deflection of filaments for various input voltages. For a small voltage (10V) applied across the terminals, negligible deflection in the cilia was observed. However, as the voltage was ramped up, and reaches the pull-in voltage, more of the filaments start to deflect and stick to the bottom surface. For a voltage that is high enough (60V) all the cilia deflect and stick to the surface. Care was taken to ensure that the maximum voltage applied did not exceed the dielectric breakdown.

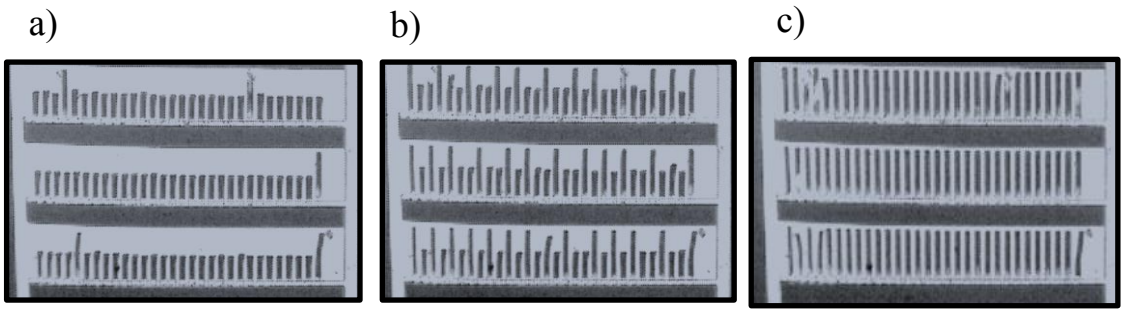

Figure 6-3: Deflection of cilia for various values of voltage applied across the plates.

6.2.2 Oscillating magnetic field

Next, to selectively actuate the cilia, an array of electrostatic cilia is fabricated with the bottom electrode placed only under a select few. Figure 6-4 shows the layout of the bottom electrode. Here, the bottom electrode is shaped in the form of letters ‘GT’. The magnetic field is first rotated with the voltage turned off. It is observed that all the cilia are actuated and behave the same way. After a certain duration, the voltage is turned on,

which immobilizes the cilia above the bottom ‘GT’ electrode. The other cilia are not influenced by the electrostatic forces and they continue to oscillate following the magnetic field.

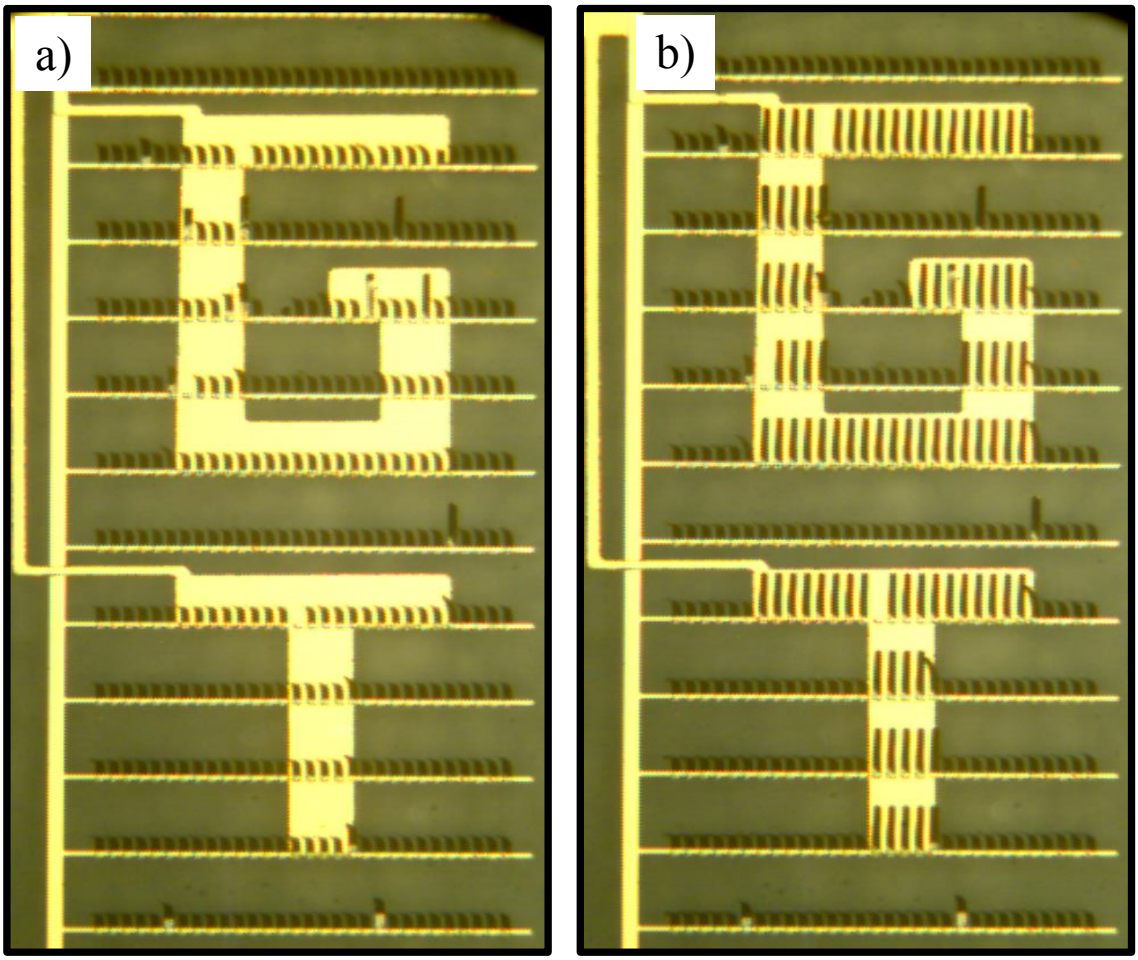

Figure 6-4: Snapshots from the Video 10. **a)** Voltage is OFF and all the cilia are actuated. **b)** Voltage is ON and the cilia over the bottom electrode – ‘GT’ are immobilized, while the other continue to oscillate.

6.3 Summary

A new method is demonstrated for fabricating artificial cilia which can be simultaneously actuated using magnetic forces and controlled using electrostatic forces. The method uses the concept of a simple electrostatic actuator. A bottom gold electrode is deposited, and the cilia act as the top electrode. The cilia snap to the bottom substrate when an AC voltage is applied. The described method for creating combined electrostatic and magnetic actuation of filaments allows for individually controllable cilia. The electrostatic field on each filament can be individually switched on and off to control its motion.

Chapter 7. BIOMIMETIC CAPTURE

Microorganisms use biological cilia to create various kinds of transport, and most important among them is the transport of suspended particles. Biological cilia are shown to effectively capture and trap specific particles for feeding[119–123]. Motivated by this, the use of artificial magnetic cilia to capture particles suspended in a fluid is proposed. Perhaps, such nature inspired ciliary capture and isolation of particles can be incorporated in microfluidic lab on chip devices for pre-concentration of cells and analytes. In this chapter, the particle capture capabilities of magnetic cilia and a proof of concept demonstration of *Salmonella* capture is discussed.

7.1 Introduction

Among the various functions of natural cilia, the feeding mechanism is the most important. It has been observed that organisms use cilia to sort, capture, divert and feed on particles of interest[119–124]. For example, *Vorticella*, a unicellular organism is known to create feeding current that transport the food particles towards the organism[125–127]. Starfish larvae are also shown to use ciliary bands to produce counter-rotating vortices to trap food particles and feed on them[10]. The surface of natural cilia can also act as active capture surfaces to capture food particles in the surrounding fluid[128–130]. The behavior of these biological cilia provides a useful design concept to create microfluidic devices where artificial cilia could regulate the movement of microscopic particles within the device. In particular, particle capture on the ciliary surface is investigated in this chapter.

The isolation of rare cells and pre-concentration of target species for analysis are important steps in detection and enumeration of bacteria [131,132] and cancer cells[42,133,134]. Many microfluidic techniques such as inertial focusing[135] and deterministic lateral

displacement[136] exploit the size difference among cells to separate and isolate them. The efficiency of these techniques is proportional to the cell volume. Therefore, bacterial cells, which are smaller in size ($\sim 1\mu m$) in comparison to animal cells ($< 5\mu m$)are much more difficult to isolate and detect. Furthermore, cell concentrations of $\sim 10 CFU/ml$ are usually the target detection limit, and it makes the problem more challenging.

A typical microfluidic approach for bacterial capture relies on target specific antibody coatings on stationary surfaces in a microchannel that are used to arrest the target cells dispersed in a fluid stream [137–140]. The efficiency of capture in such systems depend on the probability of target cells that come in contact with the antibody coated surface. Such immunoassays usually have low capture efficiency[141–144]. The probability of capture can be enhanced by the use of an active surface, such as the surface of cilia that vigorously oscillate in the fluid and produce chaotic motion, which can potentially increase the capture probability. Immunomagnetic separation of bacterial cells using magnetic beads is also widely used. In this method, an added step of separating the magnetics beads with the bacteria from the ones without the bacteria is required. The cilia act to mix fluid and to create flow circulations that bring bacteria closer to the cilium surface. Furthermore, antibody coated cilia that beat, sweep through a large area of fluid enhancing contact probability with target bacteria to facilitate their capture. Thus, the use of arrays of magnetic cilia can drastically increase the capture efficiency of the target compared to stationary surfaces.

With a motivation to develop an active ciliary system to perform bacteria pre-concentration in microfluidic devices, particle capture capabilities of magnetic cilia are demonstrated in this chapter. To this end, streptavidin functionalized cilia are used to

capture biotin particles its surface. Furthermore, capture of *Salmonella* bacteria on antibody functionalized ciliary surface is also demonstrated as a proof of concept.

7.2 Experimental setup

Particle capture by magnetic cilia is demonstrated using streptavidin-functionalized cilia that beat in the fluid to capture biotin labelled fluorescent particles. A schematic of the capture mechanism is shown in Figure 7-1a. The red circles in the figure represent the fluorescent-biotin particles that are captured on the surface. The cilia are incorporated inside a microchannel loop, like the setup described in Chapter 4. Biotin particles are introduced into the channel loop at known concentrations thorough the fluid reservoirs. The cilia are actuated by a rotating magnet, which pumps the fluid in the channel loop. The suspended particles are recirculated in the channel loop and perform several passes across the ciliary array. This biomimetic setup enables the cilia to simultaneously pump the fluid as well as capture particles, similar to natural cilia in suspension feeders.

7.3 Surface functionalization

To create capturing cilia, streptavidin-coated microbeads (Dynabeads M270, 65305, Thermofisher scientific) are immobilized on the surface of the cilia. To this end, the cilia are first immersed in 1% APTES solution. The silane group bind to the thin oxide layer on the NiFe, and the amine group is protonated $-NH_3^+$ to create an overall positive charge on the cilia. Next, carboxylate microbeads coated with *anti-Salmonella* are introduced. The beads with the carboxyl group $-COO^-$ have a slight negative charge and, therefore bind to the surface of the cilia. This procedure results in cilia covered with

streptavidin-coated microbeads that are electrostatically bound to the surface[145]. Similarly, the bottom glass wall of the microchannel is covered with streptavidin-coated microbeads. The latter is used to compare capture efficiency between cilia that beat actively, and a passive static surface. Figure 7-1d shows ciliary surface immobilized with the beads. This method enables us to visually verify that the beads are immobilized on the cilia, and therefore are the target specific receptor.

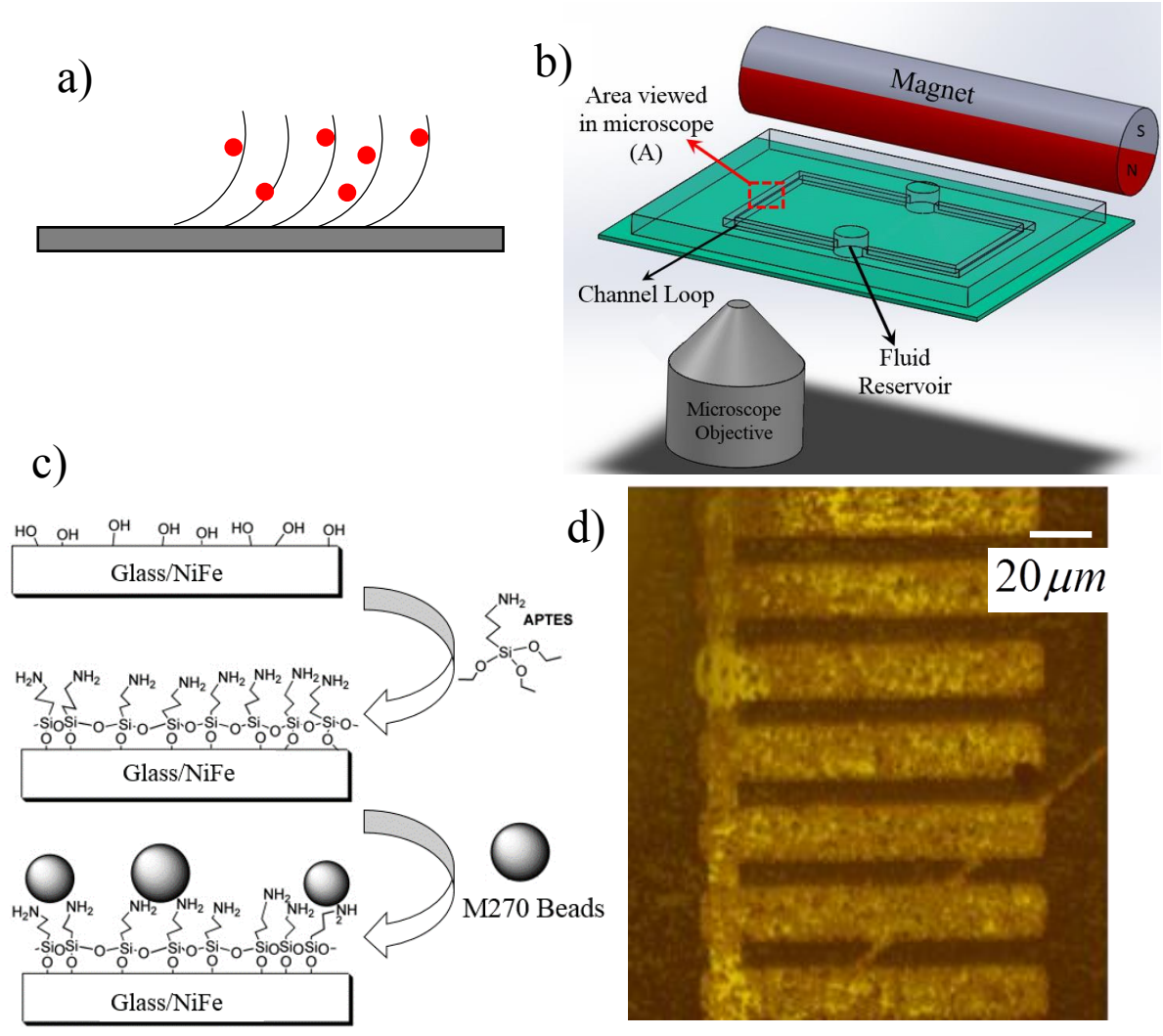

Figure 7-1: **a**) Mechanism of particle capture using magnetic cilia. The red dots indicate the particles captured on the cilia surface. **b**) schematic of the experimental setup consisting of a closed loop microchannel with cilia incorporated on one side. **c**)

Immobilization of streptavidin beads on the NiFe cilia. **d**) Microscope image of Dynabeads M270 immobilized on the cilia and glass surface.

7.4 Particle capture experiments and results

The experiments reveal a significant number of particles captured on the surface of the oscillating cilia. In the first set of experiments, the cilia are actuated for known intervals of time and images recorded periodically to measure the number of particles captured on the ciliary surface. It is found the number of particles captured on the ciliary surface increases with time (indicated in Figure 7-2). The cilia initially start with a low concentration of particles on the surface, and as time progresses, the number of particles captured increases. This result also implies that the captured particles are strongly bound to the cilia and rapid agitation does not release them back into the fluid. It is also found that the captured particles are selectively bound near the edges of the cilia, as shown by an outline of fluorescent particles along the filament edges in Figure 7-2. Such selective capture of particles near the ciliary edge is seen is all the experiments and is perhaps because a higher number of particles come in contact with the cilia edges as the fluid flows around the edge where the highest local shear rates can be expected.

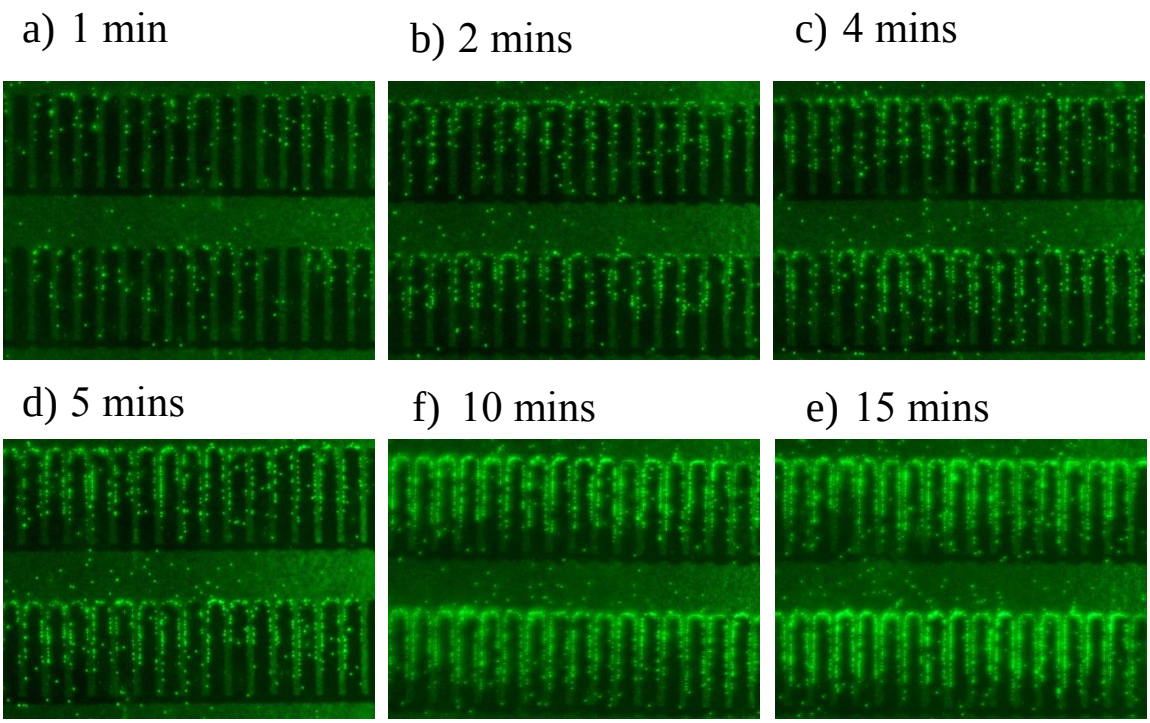

Figure 7-2: Snapshots of the ciliary array at different instances of time during a capture experiment. Note the increase in the number of fluorescent particles captured from 1min to 15mins. These images are taken for a cilia oscillation frequency $f = 8.3Hz, Sp = 1.9$, and particle concentration of $10^5/ml$.

The number of particles captured on the surface of the cilia is approximated by the use of the automatic particle counter in ImageJ (see APPENDIX B). A plot of the number of particles captured as a function of time for various oscillation frequencies is shown in Figure 7-3. The experiments with $Sp = 1.9$ of the magnet reveal that number of particles increase in a somewhat linear fashion with time. For higher frequencies of oscillations, the rate of particles captured is initially linear and reduces after a certain duration of time. For example, notice that the particles captured for $Sp = 2.4$ and $Sp = 2.4$ increases linearly until 2mins and 5mins respectively, and reduces beyond these

respective times. The reduction in the capture rate is perhaps because of reduced number of available capture sites as more and more particles accumulate on the ciliary surface. The surface of the cilia is ultimately expected to saturate with the fluorescent particles, and thus leave negligible capture sites to arrest additional particles.

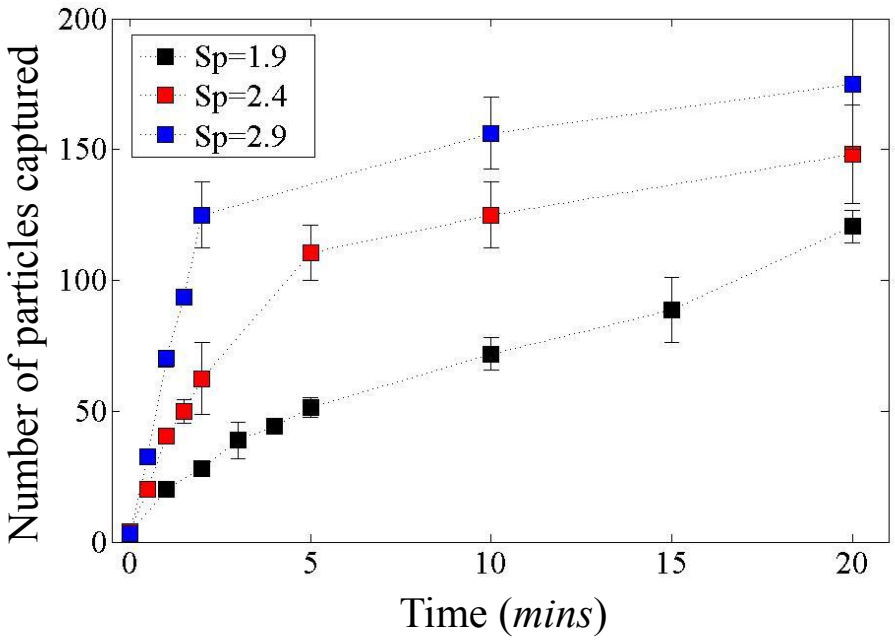

Figure 7-3: Number of particles captured as a function of time for different oscillation frequencies of the cilia. 16 rows of $200\mu m$ length, $20\mu m$ width cilia were used for these experiments.

Furthermore, the number of particles that are captured on the ciliary surface is significantly more than the number of particles captured on the bottom glass surface. Figure 7-4a shows a comparison of the number of particles captured on the cilia and glass surface. Note that the streptavidin beads are immobilized everywhere, including the bottom glass surface. Similarly, defective cilia that are not released from the substrate also show negligible capture. Figure 7-4b shows an example of defective cilia that shows

no particle capture. Therefore, the surface of glass substrate and the defective cilia act as negative controls, and the selective capture of particles on the surface of oscillating cilia proves their effectiveness in the capturing particles as compared to a stationary flat surface.

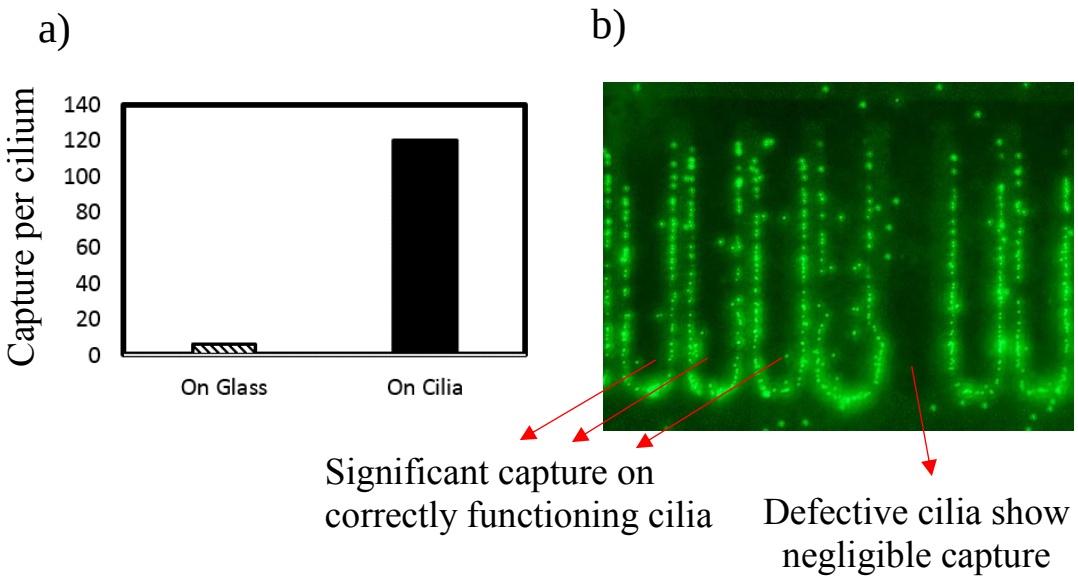

Figure 7-4: a) Comparison between the number of particles capture on the stationary glass surface and oscillating ciliary surface. b) Negligible particles captured on defective cilium that is not released.

As noted in Figure 7-3, the capture rate depends on the oscillation frequency of the cilia, with higher frequencies that result in higher capture. This dependence is characterized in the next set of experiments, in which capture is performed at various frequencies of oscillation for a period of $30s$ and the number of captured particles is counted. Since change in frequency of operation changes the Sp of operation, the average number of captured particles on each cilium is plotted as a function of Sp in Figure 7-5.

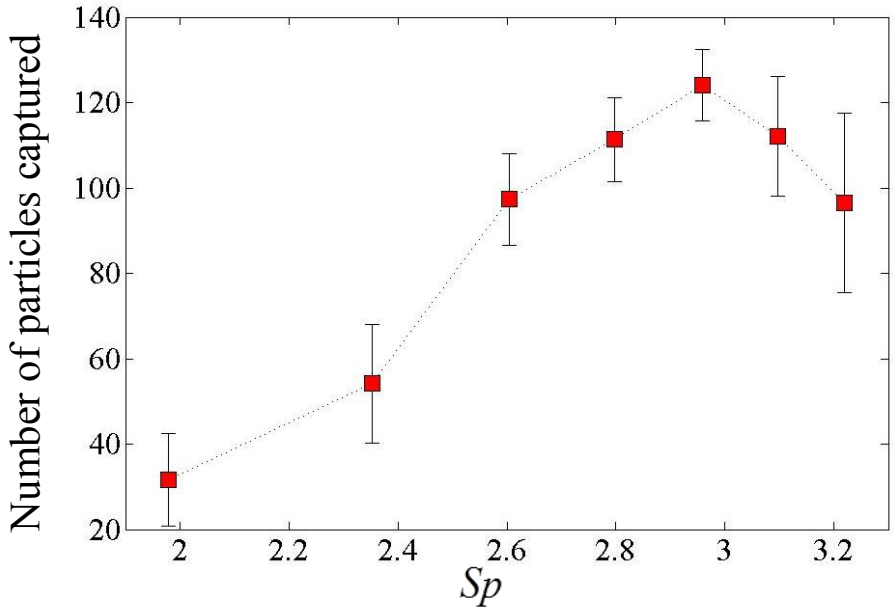

Figure 7-5: Number of particles captured per cilium after $30s$ of oscillation, as a function of Sp.

The capture count initially increases until a certain optimum Sp and reduces for further increase in Sp. Maximum capture is observed at $Sp \sim 2.9$. It is interesting to note that optimum for fluid pumping is also $Sp \sim 2.9$, as shown in Figure 4-2. This result indicates a direct correlation between the fluid pumping and particle capture in such magnetic cilia. For a fixed concentration of particles in the channel, the net particle flux that flows across the array of cilia is directly dependent on the fluid pumping, and therefore higher fluid pumping implies higher flux of particles that flow across the array. These results indicate that particle capture is directly influenced by the flux of particles that flow across the array.

7.4.1 Capture efficiency

In the previous section, the effectiveness of cilia in performing capture is demonstrated in comparison to a stationary surface. Next, the capability of magnetic cilia in the capture of low concentrations of particles in a sample is investigated. $30\mu l$ of samples containing biotin labelled particles is introduced at various concentrations into the microchannel loop and the particle concentration is monitored as a function of time. The cilia are actuated to circulate the sample in the microchannel loop and simultaneously capture particles upon contact. Therefore, the particle concentration in the sample is expected to deplete. The concentration of particles being recirculated in the channel is measured by recording images of particles in section A (Figure 7-1b) of the channel at various intervals of time. The particle concentrations in these experiments are kept very low (max of $250/\mu l$), to ensure that the ciliary surface is not saturated over time. The particle concentration is normalized using the initial particle concentration and plotted as a function of time in Figure 7-6.

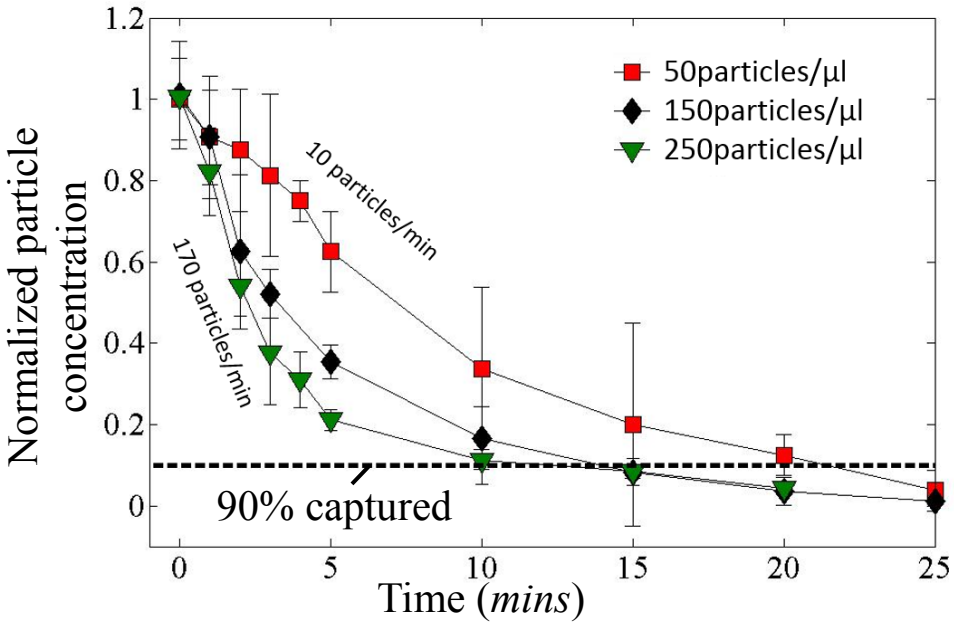

Figure 7-6: Particle concentration in the microchannel normalized with the initial concentration versus time. As the cilia oscillate to induce flow, the particles are captured and therefore the number of particles in the channel depletes. 40 rows of $80\mu m$ length, $8\mu m$ width cilia were used for these experiments.

The rate at which the particles deplete in the microchannel shows a direct relation with the particle concentration. A larger initial concentration results in higher depletion rates (indicated by the slope of the green data points), and a lower initial concentration leads to lower depletion rates(indicated by the slope of the red data points). This result implies that a sample with low concentration of particles takes more time to deplete. For example, a particle concentration of $250/\mu l$ takes about 10mins to show 90% depletion, whereas $50/\mu l$ sample takes about 20mins to show the same 90% depletion.

7.5 Specificity of capture

It is important to ensure that the capture demonstrated in this section is specific to a target. To test this, capture experiments similar to the ones described above are performed, but by introducing a binary mixture of two particles in the microchannel. Equal concentrations of green biotin particles (FluoSpheres™, $1\mu m$, Thermofisher Scientific) and red carboxyl beads (Fluoro-Max™, $3\mu m$, Thermofisher Scientific) are mixed thoroughly in PBS and introduced in the microchannel. The streptavidin beads immobilized on the ciliary surface are expected to capture the green biotin particles selectively, and any non-specific binding of the red carboxyl beads is expected to be low on the ciliary surface. Figure 7-7a shows the initial concentration of the red carboxyl and green biotin particles. Note that the initial concentration of both particles is similar ($\sim 10^6/ml$). The sample is introduced in the microchannel loop and processed by the oscillating cilia for 1min at $500RPM$, and the cilia are washed with 1x PBS $pH = 7.4$. Figure 7-7b shows the images of the ciliary array after the experiment under the red and green fluorescent filters to image the two kinds of particles. A significantly higher number of green biotin particles are captured on the ciliary surface. The number of non-specifically bound red carboxyl particles are much less in comparison. In Figure 7-7c the initial concentration of particles and the number of captured particles after the experiment is plotted. As can be noted, the initial concentration of red and green particles is similar. After the experiment, the final number of green particles captured on the ciliary surface is significantly higher than the non-specific capture of red particles. The number of biotin particles captured is around 10x times the non-specifically bound carboxyl particles. These experiments demonstrate a high specificity of capture in such ciliary systems.

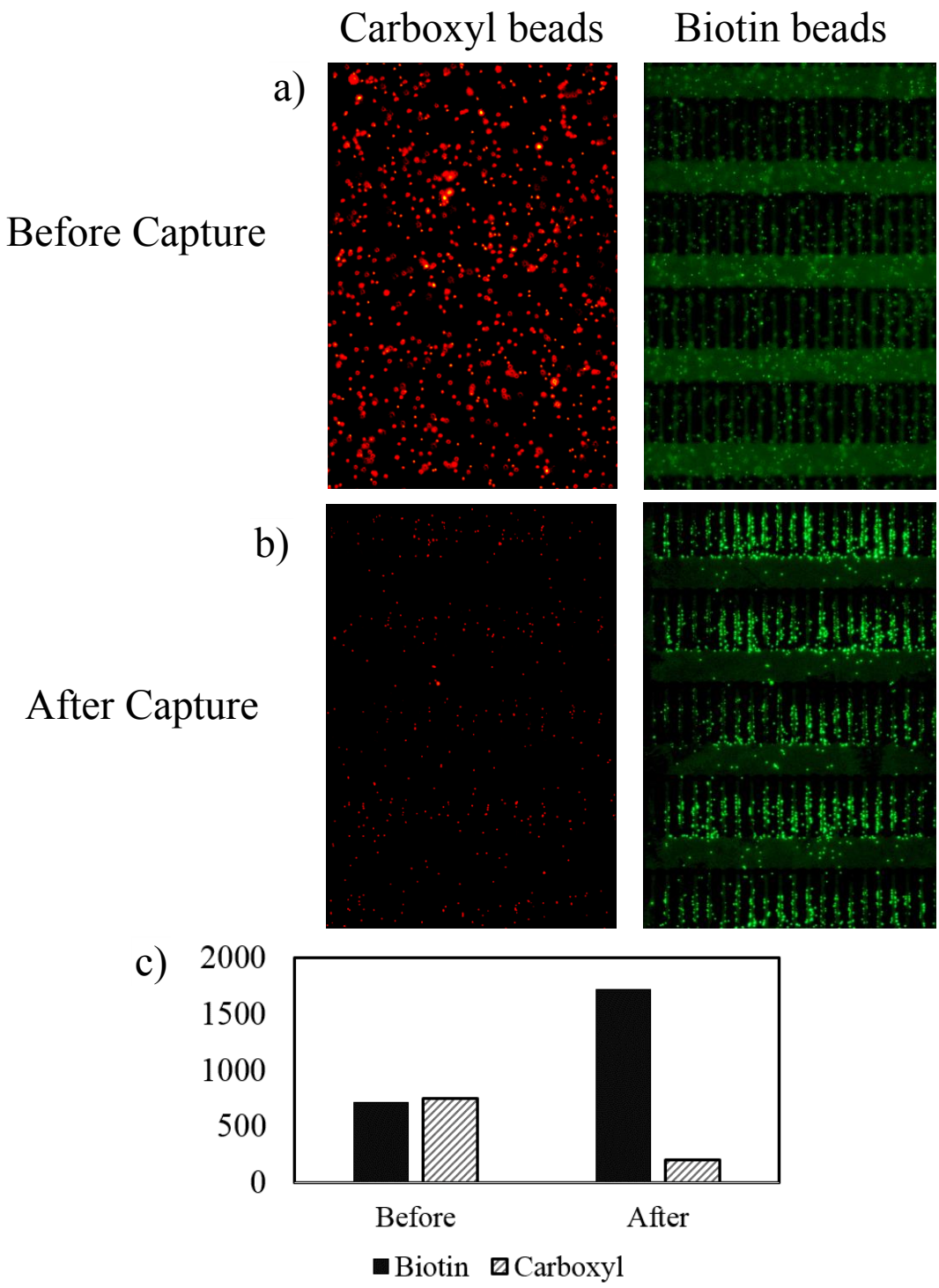

Figure 7-7: **a**) Initial concentration of carboxyl beads and biotin particles. **b**) Final concentration of carboxyl and biotin particles after the device is washed. **c**) Comparison of the initial and final concentration of the particles in the device. Note the higher number of biotin particles captured point to the specificity of capture.

7.6 Bacteria capture results

The capture of bacterial cells that are usually present in low concentrations (100 CFU/ml) is critical for food safety applications. To demonstrate capture of bacteria by magnetic cilia, antibody is immobilized on the ciliary surface and experiments similar to the ones discussed in the previous section 7.4 are performed. Specifically, the capture of *Salmonella enterica with anti-Salmonella* coated cilia is demonstrated in this section. These experiments were performed at the University of Georgia, in the lab of Dr. Ynes Ortega and Dr. Marilyn Erikson.

In order to be able to visualize *S. enterica* cells, they were labelled with Clontech Gfpuv green-fluorescent protein plasmid (Mountain View, CA) and use a calcium chloride heat shock transformation method[146]. This makes the bacteria fluorescent and can be directly visualized under a fluorescent microscope. Next, the method used to functionalize the antibody on the ciliary surface is an extension of the functionalization protocol discussed in the precious section (also shown in Figure 7-8). After the streptavidin beads are immobilized on the surface of the cilia, $10\mu l$ of biotin-labelled anti-salmonella (ab21118 - Rabbit polyclonal, Abcam) at $4mg/ml$ is introduced on the ciliary surface. The biotin-anti-salmonella antibody binds to the streptavidin beads. This leaves the antibody exposed and available for capture of the cells. *S. enterica* cells. The bacterial cells are then introduced with a concentration of $10^5 cells/ml$ suspended in 1x PBS $pH = 7.4$ into the channel loop and the cilia are actuated. *S. enterica* cells that encounter the antibody bind to it, thus enabling capture.

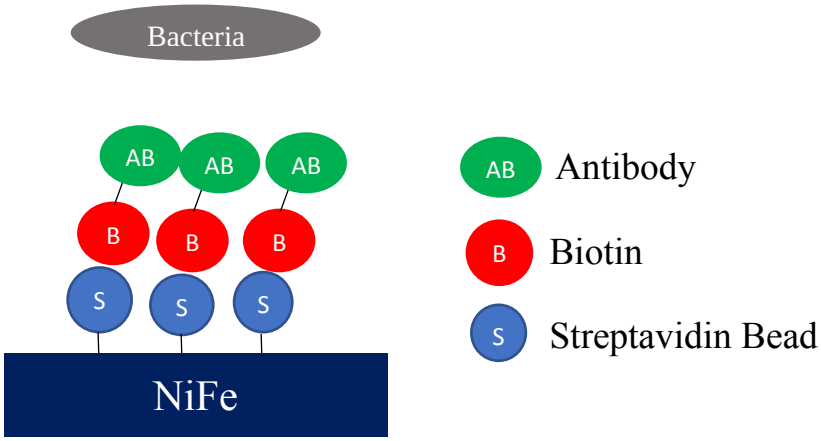

Figure 7-8: Schematic showing how the antibody is immobilized to the cilia.

The cilia are actuated at $50Hz$ for a period of 5 minutes. Figure 7-9 shows images obtained using fluorescence microscopy that visualize the location of captured fluorescent bacteria on the cilia and channel substrate. The experiment reveals that the amount of *S. enterica* cells captured by the cilia is significantly larger than the number of cells captured on the bottom glass surface. Indeed, only a few cells can be seen sticking to the glass, whereas most of the cells are found on the cilia. Furthermore, the captured cells are localized on the edges of beating cilia where the highest local shear rates can be expected (Figure 7-9b). These results are very similar to the ones observed for particle capture in the previous section. Thus, the experiment demonstrates the potential use of magnetic cilia to capture target species from a fluid for their effective isolation and pre-concentration. The pre-concentrated cells can be resuspended in a smaller volume of fluid for easier detection.

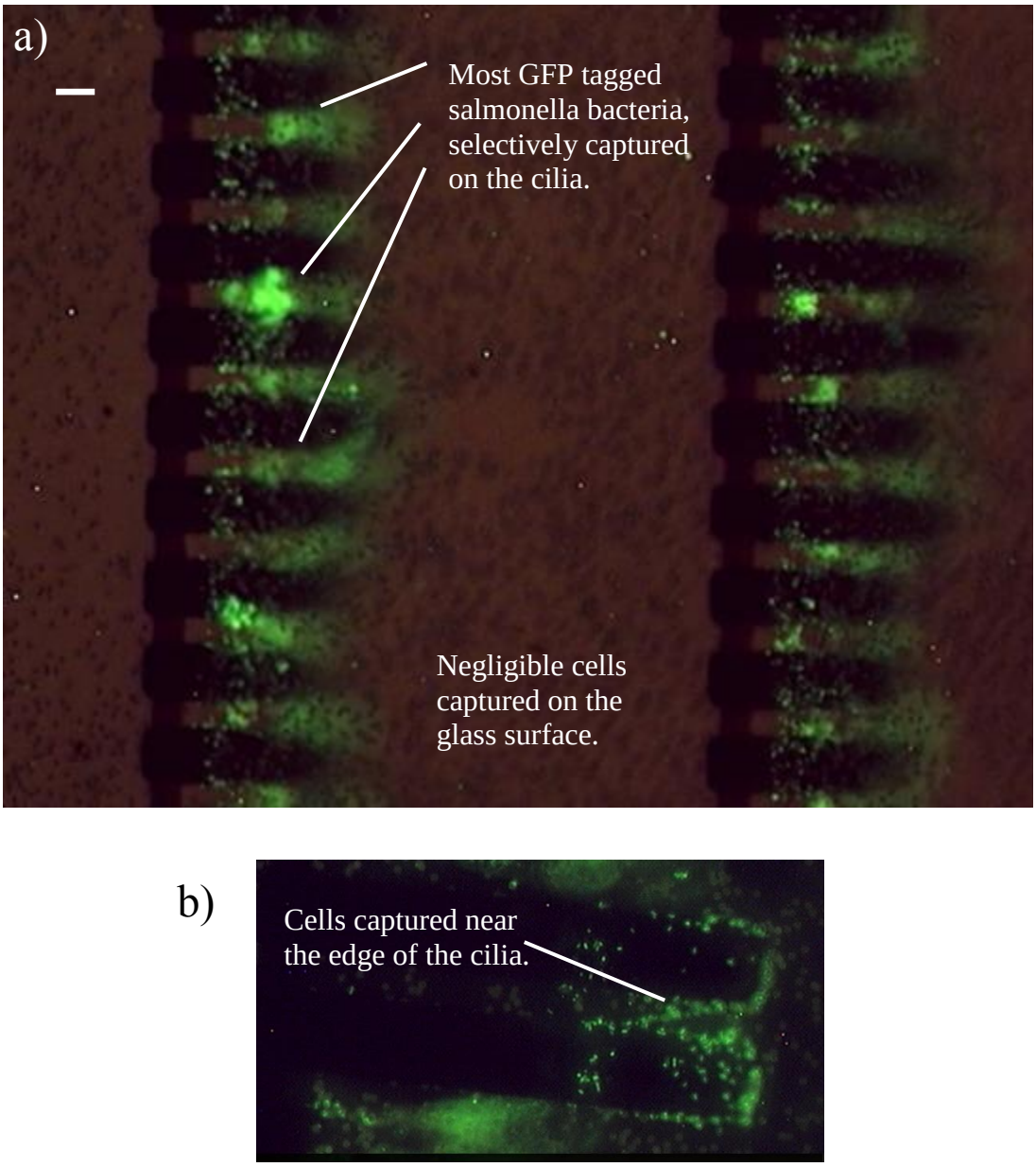

Figure 7-9: Bacteria capture with anti-body immobilized cilia. **a)** The GFP tagged fluorescent salmonella are selectively captured by the cilia. Very few cells attach to the bottom glass substrate. **b)** Close up of the captured salmonella cells on the cilia surface. Notice that the cells stick mostly to the edges of the cilium.

7.7 Summary

To summarize, biologically inspired particle capture capabilities of artificial magnetic cilia are demonstrated in this chapter. The surface of the cilia is uniformly functionalized with the target specific receptors which act as active binding sites for the target. The fast-asymmetric oscillations of the cilia enhance the local fluid mixing and enhances the particle capture. It is observed that the number of captured particles increases linearly with time, until the number of binding sites on the cilia reduces as more and more particles are captured. It is also noted that the capture count depends on the frequency of oscillation of the cilia. A maximum capture count is observed for cilia operating to produce maximum fluid pumping. This suggests a direct relation between the fluid pumping produced by the cilia and the capture efficiency. Furthermore, the capture rate is found to depend on the concentration of particles in the sample, with higher particle concentrations resulting in higher capture and lower concentrations resulting in lower capture. Sample with particles concentration as low as $50/\mu l$ were captured with efficiencies of up 90% in 20 *mins*. More generally, these results suggest a direct relation between capture and the flux of particles flowing over the ciliary array. The streptavidin coated cilia when exposed to a binary mixture consisting of biotin particles and carboxyl modified particles, show very specific binding of the biotin particles.

Owen[147] has previously reported capture of biotin particles using Streptavidin coated orbiting magnetic microbeads. It is reported that 90% capture can be obtained for a sample flowing at $0.5\mu l / \min$ using orbiting magnetic microbeads. This leads to a 90% capture efficiency for processing $10\mu l$ of sample in 20 *mins*. The artificial ciliary system

is capable of processing $30\mu l$ of sample in the same 20 *min* time frame and achieving 90% capture .Therefore, with the ciliary system, we are able to increase the throughput by a factor of three.

The same principle of operation can be applied to capture any target species. As a proof of concept, *Salmonella* cells are captured on antibody coated cilia. The bacteria capture experiments show comparable results to particle capture experiments. The bacteria are selectively bound on the surface of the cilia and on the edges. A negligible number of cells attach to the bottom stationary glass surface, which also contains the antibody.

Chapter 8. CONCLUSIONS

8.1 Concluding remarks

Cilia are hair-like protrusions on the surface of almost all cells/organisms and perform a vast variety of functions. In fact, cilia are the primary means through which cells interact with the surroundings. It is known that cilia function as sensory organelles used for chemical sensation, signal transduction, and control of cell growth, assist in creating fluid transport for swimming and feeding of the organism.

Inspired by biological cilia, this thesis aims at developing a new technology for microscale fluid manipulation using artificially fabricated cilia. The artificial cilia are made of a soft magnetic filaments that can be actuated by rotating an external magnetic field. A simple surface micromachining process is developed to fabricate the cilia on glass substrates, and their actuation is demonstrated using a simple rotating magnet. It is found that artificial magnetic cilia perform a time-irreversible beating pattern, similar to biologically cilia and therefore are capable of producing fluid transport. Furthermore, magnetic forces allow for actuation from a distance, which eliminates any wiring/interconnects to the device and is safe for use with biological matter. The developed synthetic cilia can be readily incorporated into various microfluidic lab-on-chip devices for a vast variety of applications requiring fluid transport.

The kinematics of motion of individual magnetic cilium have been characterized by imaging the beating pattern and is validated against computer simulations. It found that a magnetic moment which depends on the local position of the cilium causes the distinctly asymmetric beating. Furthermore, it is found that clockwise and counter-

clockwise motion of the magnetic field leads to significantly different beating pattern. It is shown that non-dimensional sperm number (Sp - ratio of viscous to elastic forces) and magnetic number (Mn - ratio of magnetic to elastic forces) determine the motion of the filaments. The asymmetric beating is characterized as function of magnetic and sperm numbers. These cilium oscillations are promising for creating spatially asymmetric motion required to induce fluid pumping and other transport processes in a low Reynolds number environment.

Next, the time-irreversible motion of magnetic cilia is shown to produce considerable fluid flow under continuous magnetic actuation. An array of cilia with 16 rows of cilia is shown to produce flow rate up to $1.4 mm/s$. This is the highest flowrate reported for a device of this scale. The self-pumping frequency, a metric used to assess the effectiveness of the pump based on its size, is estimated to be ~2.5/min. This is the highest reported value in similar ciliary microfluidic pumping systems. Therefore, artificial magnetic cilia such as developed in this study are promising for active control of fluid flow in microfluidic devices.

Furthermore, fluid pumping is characterized as a function of several parameters such as the channel dimensions, frequency of oscillation, and spacing between the rows of cilia. The fluid pumping is shown to be a maximum for an operating condition with $Sp \sim 2.9$. It is found that cilia are not affected by the oscillations of cilia in neighboring rows.

It is often observed that natural cilia beating in a sequential one by one metachronal fashion. Although the origin of metachronal motion is still debated, it is

shown to enhance the fluid transport produced by cilia. Perhaps, artificial cilia can be actuated in a biomimetic metachronal fashion to exploit the enhanced fluid transport. Studying the effects of metachronal motion has been particularly difficult for researchers given the experimental difficulties in achieve them. With the simple fabrication and actuation mechanism developed in this thesis, one can easily fabricate cilia to beat in a metachronal fashion. A variety of methods to create metachronal motion in artificial cilia is demonstrated. It is shown that a difference in the cilium beating phase can be obtained by varying the magnetic number (Mn) of operation. Cilium geometric properties such as the length and thickness are varied across the array such that Mn varies across the array, and they respond with a phase difference when actuated by a magnetic field. It is shown that metachronal motion thus obtained is only dependent on Mn , and independent of Sp .

One of the primary functions of natural cilia in suspension feeders is trapping particles for the organism's feeding. It is also known that natural cilia can be very specific in the particles they capture. In this thesis, particle capture capabilities of artificial cilia is demonstrated and characterized. The surface of the cilia is functionalized with a target specific receptor (streptavidin). The target particles ($1\mu m$ biotin coated) in concentrations as low as $50/\mu l$ are flown over the cilia and capture efficiencies of up 90% in 20 *mins* of processing a sample is demonstrated. It is also found that the capture is specific to a target of interest. When a sample with a binary mixture of two species is introduced, the cilia specifically capture only one type of particles and very little non-specific capture is observed. Thus, such artificial systems can be used for low concentration particle capture and pre-concentration. This can particularly be useful in isolating pathogenic bacteria in food samples for their easy detection. Once the target

cells are captured on the ciliary surface, they can be released in to smaller volumes of fluid, which will make their detection easier. As a proof of concept, *Salmonella* cells extracted from a food sample are specifically captured on the ciliary surface. The cilia are functionalized with *anti-Salmonella* to specifically bend to the bacteria. It is shown that the active oscillating cilia are particularly effective in capturing the cells as compared to a passive surface.

In conclusion, this thesis develops artificial cilia that are capable of producing microscale fluid transport in creeping flow regimes. Such fluid transport can be used in a wide variety of Lab-on-chip applications. The simplicity in the fabrication and actuation process with high repeatability in operation and function is the novelty of this work. Characterization of the cilium kinematics, pumping characteristics, metachronal actuation, provides guidelines for implementing such cilia in a wide variety of microfluidic applications.

8.2 Contributions of this thesis

1. Conceptualized artificial magnetic cilia for microfluidic applications. The cilia are made of soft magnetic NiFe filaments.
2. Developed a simple surface micromachining fabrication process to realize the cilia. The process uses standardized steps and the results are repeatable.
3. Characterized the kinematics of cilium beating and establishing the dependence on dimensionless parameters- sperm number and magnetic number.
4. Quantifying the fluid transport characteristics of magnetic cilia.
5. Demonstration of metachronal motion in arrays of artificial cilia.
6. Functionalizing the surface of cilia for target specific capture and characterizing the particle capture capabilities of artificial cilia.
7. Demonstrating the capture of *Salmonella* bacteria using antibody-functionalized cilia.

8.3 Outlook for future development for other applications

The artificial cilia demonstrated in this thesis can potentially be useful in a wide variety of microfluidic applications. The simplicity in design and implementation is the novelty of this work. Any fluid manipulation requiring precise metering and transport can make use of such artificial ciliary systems. The findings on magnetically actuated cilia not only guide the efficient design of microfluidic devices utilizing oscillating synthetic cilia, but can be applicable in understanding the behavior of biological cilia and their effect on fluid transport. Arrays of cilia can be used for organ-on-a-chip applications to reproduce physiological fluid flow environments for the cells/tissue to grow.

A valuable extension of this work would be the understanding of how cilia can pump non-Newtonian fluids and stratified layers of fluids, with applications in areas such as muco-ciliary clearance. Further, artificial cilia can be incorporated inside synthetic stents to allow for active pressure regulation. For example, cilia inside ocular stents can be used to actively regulate pressure for the reduction of glaucoma. Such cilia can also be implemented on microscopic artificial swimmers for drug delivery applications. Another potential application for such cilia is to remove plaque and bio-fouling by physically agitating the fluid flow. Implementing magnetic cilia on catheter can be useful in cleaning and anti-biofouling of implants.

APPENDIX A

COMSOL Modelling

Fluid structure interaction module in COMSOL was used to simulate the beating an individual cilium. Viscous forces and the system's pressure impose forces to the surface of a structure. The deformation in the soft structure is not small and the fluid regime will therefore change. This means that changes in the structure and the fluid dynamics are coupled. A flexible solid structure was constructed using multiple rectangles as shown in Figure A1a. The outside of the structure is defined as fluid. A fixed boundary condition is applied on one end of the structure. Moments proportional to $\sin(2\theta)$ is applied on each of the other nodes (See section for details on how this is derived). The magnitude of this moment is controlled by varying parameter AA to match the amplitude of the experimentally observed trajectory. The definition of this locally applied moment is as shown in Figure A1a.

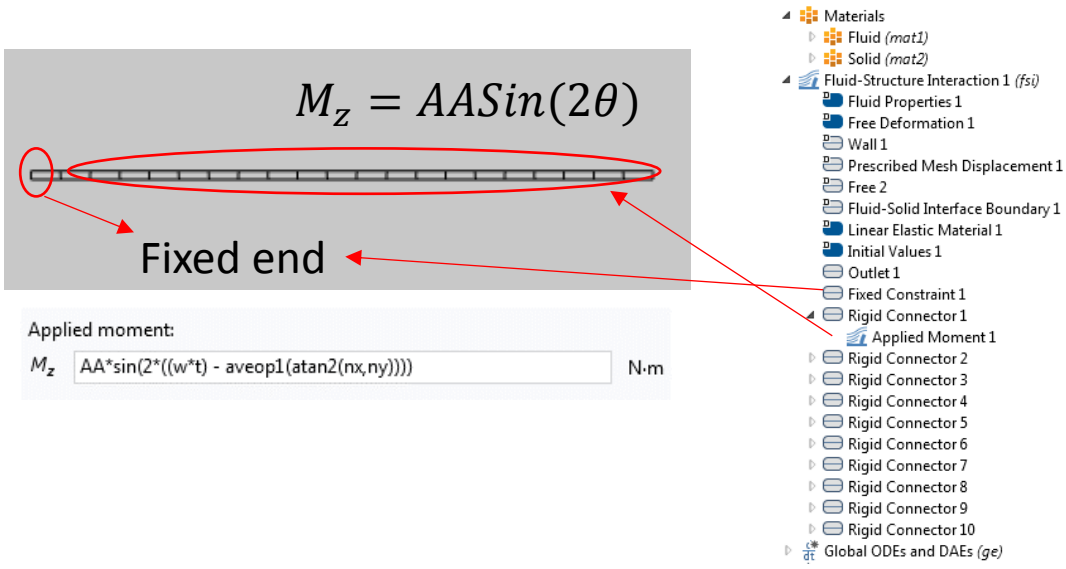

Figure A1: a) COMSOL model and the applied boundary conditions. b) Components used in the construction of the COMSOL model.

Meshing for this model is implemented in two steps. First, a mesh is created with the structure being horizontal. At larger deformation, the solver is unable to use the same mesh to perform the computations. Therefore, a stop condition is included in the solver to stop the computation when the mesh reaches a certain threshold. At this point the solver re-meshes the structure in the deformed state and continues the computation. The initial mesh used and the deformed mesh is shown in Figures A3a and A3b respectively.

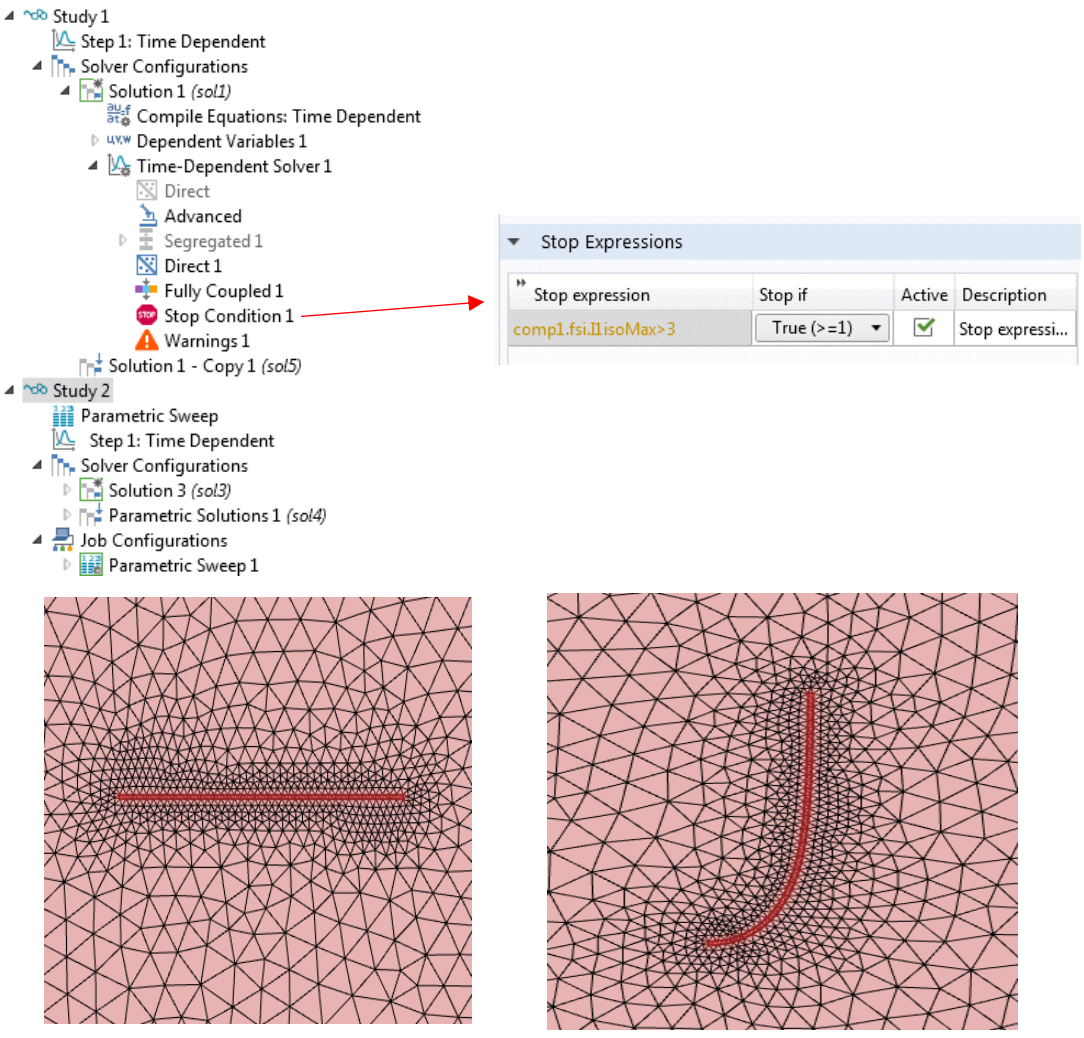

Figure A2: The simulation is done is two steps. a) Stop condition used in step 1 to determine the deformed state. b) Mesh used in the un-deformed state. c) Mesh used after the structure deformed.

APPENDIX B

Counting particles in ImageJ

The raw RGB image captured in JPEG format is first imported into ImageJ. This can be done with individual files or with a batch (Figure A21).

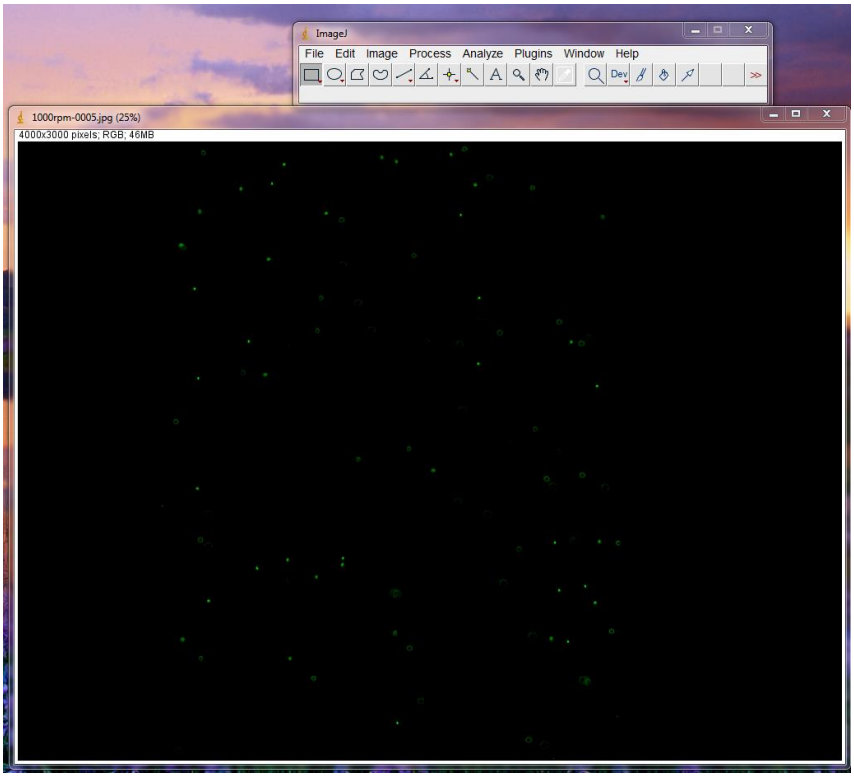

Figure A21: Importing raw images into ImageJ.

Next the image is converted into a 16bit greyscale and a threshold is set to delete the background. An example of the applied threshold and the processed image is shown in Figure A22.

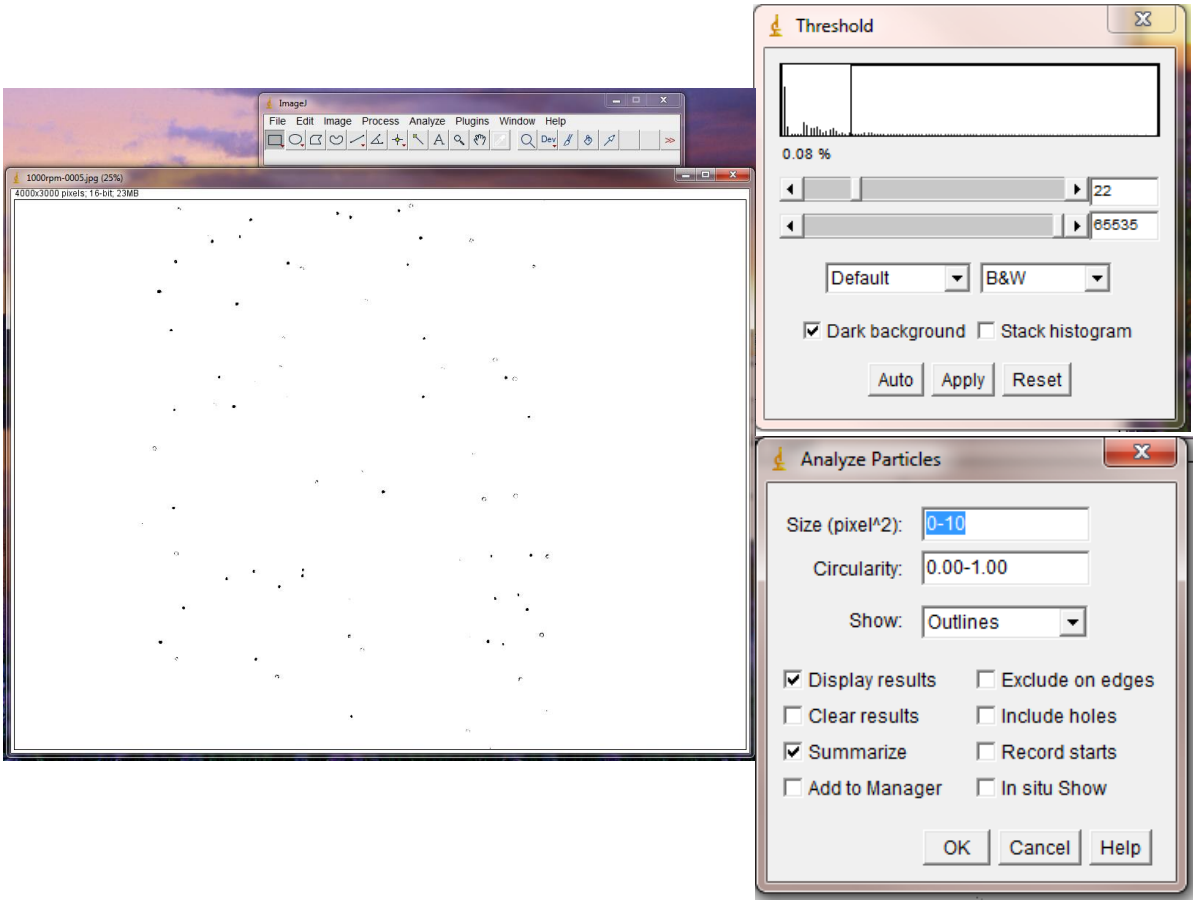

Figure A22: a) Converting the RGB image to greyscale and setting a threshold. b) Example of the set threshold to obtain the processed image. c) Parameters set to analyze the number of particles in the image.

Next, the number of particles is counted using the A**nalyze Particles** option under the **Analyze** tab. The parameters that determine the circularity and size of the individual particles is set. An example is shown in Figure A22c. The number of particles in then counted by pressing the OK button. The summary of results is displayed with the program displaying the average size of the particles as well as the number of counted particles. An example is shown in Figure A23.

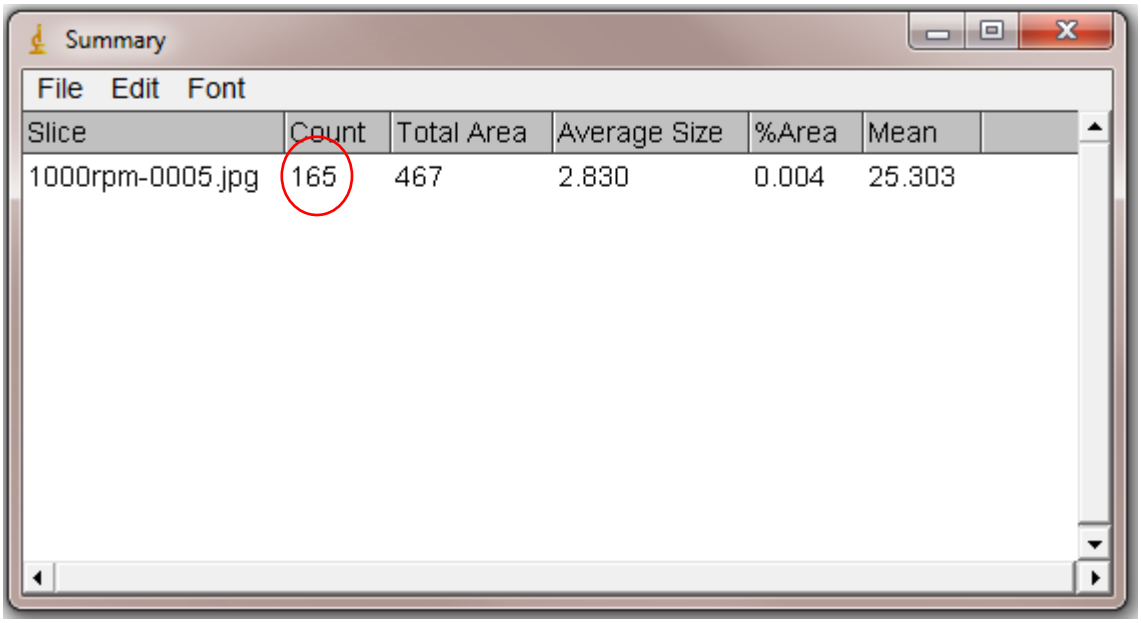

Figure A23: Example of the result obtained by counting the number of particles.

REFERENCES

1. Kovarik, M. L. *et al.* Micro Total Analysis Systems for Cell Biology and Biochemical Assays. *Anal. Chem.* **84,** 516–540 (2012).
2. Taylor, G. Analysis of the swimming of microscopic organisms. in *Proceedings of the Royal Society of London A: Mathematical, Physical and Engineering Sciences* **209,** 447–461 (The Royal Society, 1951).
3. Purcell, E. M. Life at low Reynolds number. *Am. J. Phys.* **45,** 3–11 (1977).
4. Qiu, T. *et al.* Swimming by reciprocal motion at low Reynolds number. *Nat. Commun.* **5,** 5119 (2014).
5. Turner, L., Ryu, W. S. & Berg, H. C. Real-Time Imaging of Fluorescent Flagellar Filaments. *J. Bacteriol.* **182,** 2793–2801 (2000).
6. Brokaw, C. J. Non-Sinusoidal Bending Waves of Sperm Flagella. *J. Exp. Biol.* **43,** 155–169 (1965).
7. Babu, D. & Roy, S. Left–right asymmetry: cilia stir up new surprises in the node. *Open Biol.* **3,** (2013).
8. Norris, D. P. Cilia, calcium and the basis of left-right asymmetry. *BMC Biol.* **10,** 102 (2012).
9. Marrase, C., Costello, J. H., Granata, T. & Strickler, J. R. Grazing in a turbulent environment: energy dissipation, encounter rates, and efficacy of feeding currents in Centropages hamatus. *Proc. Natl. Acad. Sci.* **87,** 1653–1657 (1990).
10. Gilpin, W., Prakash, V. N. & Prakash, M. Vortex arrays and ciliary tangles underlie the feeding-swimming tradeoff in starfish larvae. *Nat. Phys.* **13,** 380–386 (2016).

11. Afzelius, B. A. The fine structure of the cilia from ctenophore swimming-plates. *J. Cell Biol.* **9,** 383–394 (1961).
12. Ballard, M., Mills, Z. G., Beckworth, S. & Alexeev, A. Enhancing nanoparticle deposition using actuated synthetic cilia. *Microfluid. Nanofluidics* **17,** 317–324 (2014).
13. Mills, Z. G., Aziz, B. & Alexeev, A. Beating synthetic cilia enhance heat transport in microfluidic channels. *Soft Matter* **8,** 11508–11513 (2012).
14. Masoud, H. & Alexeev, A. Harnessing synthetic cilia to regulate motion of microparticles. *Soft Matter* **7,** 8702–8708 (2011).
15. Branscomb, J. & Alexeev, A. Designing ciliated surfaces that regulate deposition of solid particles. *Soft Matter* **6,** 4066–4069 (2010).
16. Ghosh, R., Buxton, G. A., Usta, O. B., Balazs, A. C. & Alexeev, A. Designing Oscillating Cilia That Capture or Release Microscopic Particles. *Langmuir* **26,** 2963–2968 (2010).
17. Dreyfus, R. *et al.* Microscopic artificial swimmers. *Nature* **437,** 862–865 (2005).
18. Honda, T., Arai, K. I. & Ishiyama, K. Micro swimming mechanisms propelled by external magnetic fields. *IEEE Trans. Magn.* **32,** 5085–5087 (1996).
19. Ghosh, A. & Fischer, P. Controlled Propulsion of Artificial Magnetic Nanostructured Propellers. *Nano Lett.* **9,** 2243–2245 (2009).
20. Magnetic Helical Micromachines: Fabrication, Controlled Swimming, and Cargo Transport - Tottori - 2012 - Advanced Materials - Wiley Online Library. Available at: https://onlinelibrary.wiley.com/doi/epdf/10.1002/adma.201103818. (Accessed: 30th June 2018)

21. Gao, W. *et al.* Bioinspired Helical Microswimmers Based on Vascular Plants. *Nano Lett.* **14,** 305–310 (2014).

22. Venugopalan, P. L. *et al.* Conformal Cytocompatible Ferrite Coatings Facilitate the Realization of a Nanovoyager in Human Blood. *Nano Lett.* **14,** 1968–1975 (2014).

23. Kaynak, M. *et al.* Acoustic actuation of bioinspired microswimmers. *Lab. Chip* **17,** 395–400 (2017).

24. Ahmed, D. *et al.* Selectively manipulable acoustic-powered microswimmers. *Sci. Rep.* **5,** (2015).

25. Zhang, L. *et al.* Artificial bacterial flagella: Fabrication and magnetic control. *Appl. Phys. Lett.* **94,** 064107 (2009).

26. Hu, W., Lum, G. Z., Mastrangeli, M. & Sitti, M. Small-scale soft-bodied robot with multimodal locomotion. *Nature* **554,** 81–85 (2018).

27. Kim, Y., Yuk, H., Zhao, R., Chester, S. A. & Zhao, X. Printing ferromagnetic domains for untethered fast-transforming soft materials. *Nature* **558,** 274–279 (2018).

28. Table 2. Estimated annual number of episodes of illnesses caused by 31 pathogens transmitted commonly by food, United States*. 1

29. Fukushima, H., Katsube, K., Hata, Y., Kishi, R. & Fujiwara, S. Rapid Separation and Concentration of Food-Borne Pathogens in Food Samples Prior to Quantification by Viable-Cell Counting and Real-Time PCR. *Appl. Environ. Microbiol.* **73,** 92–100 (2007).

30. Pereiro, I. *et al.* A new microfluidic approach for the one-step capture, amplification and label-free quantification of bacteria from raw samples †Electronic supplementary information (ESI) available. See DOI: 10.1039/c6sc03880h Click

here for additional data file. Click here for additional data file. Click here for additional data file. Click here for additional data file. Click here for additional data file. Click here for additional data file. *Chem. Sci.* **8,** 1329–1336 (2017).

31. (2) Challenges to developing real-time methods to detect pathogens in foods. *ResearchGate* Available at: https://www.researchgate.net/publication/313641116_Challenges_to_developing_real-time_methods_to_detect_pathogens_in_foods. (Accessed: 30th June 2018)
32. Au, S. H. *et al.* Microfluidic Isolation of Circulating Tumor Cell Clusters by Size and Asymmetry. *Sci. Rep.* **7,** (2017).
33. Dong, Y. *et al.* Microfluidics and Circulating Tumor Cells. *J. Mol. Diagn.* **15,** 149–157 (2013).
34. Khamenehfar, A. & Li, P. C. H. Microfluidic Devices for Circulating Tumor Cells Isolation and Subsequent Analysis. *Curr. Pharm. Biotechnol.* **17,** 810–821 (2016).
35. Cima, I. *et al.* Label-free isolation of circulating tumor cells in microfluidic devices: Current research and perspectives. *Biomicrofluidics* **7,** (2013).
36. Hou, H. W. *et al.* Isolation and retrieval of circulating tumor cells using centrifugal forces. *Sci. Rep.* **3,** (2013).
37. Lee, M. G., Shin, J. H., Bae, C. Y., Choi, S. & Park, J.-K. Label-Free Cancer Cell Separation from Human Whole Blood Using Inertial Microfluidics at Low Shear Stress. *Anal. Chem.* **85,** 6213–6218 (2013).
38. Bitting, R. L. *et al.* Development of a method to isolate circulating tumor cells using mesenchymal-based capture. *Methods San Diego Calif* **64,** (2013).
39. Zhao, W. *et al.* Label-free ferrohydrodynamic cell separation of circulating tumor cells. *Lab. Chip* **17,** 3097–3111 (2017).

40. Bhana, S., Wang, Y. & Huang, X. Nanotechnology for enrichment and detection of circulating tumor cells. *Nanomed.* **10,** 1973–1990 (2015).

41. Huang, S.-B. *et al.* High-purity and label-free isolation of circulating tumor cells (CTCs) in a microfluidic platform by using optically-induced-dielectrophoretic (ODEP) force. *Lab. Chip* **13,** 1371–1383 (2013).

42. Gascoyne, P. R. C., Noshari, J., Anderson, T. J. & Becker, F. F. Isolation of rare cells from cell mixtures by dielectrophoresis. *Electrophoresis* **30,** 1388–1398 (2009).

43. Cho, I.-H. & Ku, S. Current Technical Approaches for the Early Detection of Foodborne Pathogens: Challenges and Opportunities. *Int. J. Mol. Sci.* **18,** (2017).

44. Ngo, V. K. T. *et al.* Quartz crystal microbalance (QCM) as biosensor for the detecting of Escherichia coli O157:H7. *Adv. Nat. Sci. Nanosci. Nanotechnol.* **5,** 045004 (2014).

45. Bouguelia, S. *et al.* On-chip microbial culture for the specific detection of very low levels of bacteria. *Lab. Chip* **13,** 4024–4032 (2013).

46. Lisdat, F. & Schäfer, D. The use of electrochemical impedance spectroscopy for biosensing. *Anal. Bioanal. Chem.* **391,** 1555 (2008).

47. Liu, T.-Y. *et al.* Functionalized arrays of Raman-enhancing nanoparticles for capture and culture-free analysis of bacteria in human blood. *Nat. Commun.* **2,** 538 (2011).

48. Cheng, I.-F., Chang, H.-C., Chen, T.-Y., Hu, C. & Yang, F.-L. Rapid (<5 min) Identification of Pathogen in Human Blood by Electrokinetic Concentration and Surface-Enhanced Raman Spectroscopy. *Sci. Rep.* **3,** 2365 (2013).

49. Sackmann, E. K., Fulton, A. L. & Beebe, D. J. The present and future role of microfluidics in biomedical research. *Nature* **507,** 181–189 (2014).

50. Hanasoge, S. & J. Diez, F. Vortex chain formation in regions of ion concentration polarization. *Lab. Chip* **15,** 3549–3555 (2015).

51. Gravesen, P., Branebjerg, J. & Jensen, O. S. Microfluidics-a review. *J. Micromechanics Microengineering* **3,** 168 (1993).

52. Kang, D.-K. *et al.* Rapid detection of single bacteria in unprocessed blood using Integrated Comprehensive Droplet Digital Detection. *Nat. Commun.* **5,** 5427 (2014).

53. Lee, W. *et al.* 3D-Printed Microfluidic Device for the Detection of Pathogenic Bacteria Using Size-based Separation in Helical Channel with Trapezoid Cross-Section. *Sci. Rep.* **5,** (2015).

54. Toonder, J. M. J. den & Onck, P. R. Microfluidic manipulation with artificial/bioinspired cilia. *Trends Biotechnol.* **31,** 85–91 (2013).

55. Gorissen, B., Volder, M. de & Reynaerts, D. Pneumatically-actuated artificial cilia array for biomimetic fluid propulsion. *Lab. Chip* **15,** 4348–4355 (2015).

56. Masuda, T., Akimoto, A. M., Nagase, K., Okano, T. & Yoshida, R. Artificial cilia as autonomous nanoactuators: Design of a gradient self-oscillating polymer brush with controlled unidirectional motion. *Sci. Adv.* **2,** e1600902 (2016).

57. Orbay, S., Ozcelik, A., Bachman, H. & Huang, T. J. Acoustic actuation of *in situ* fabricated artificial cilia. *J. Micromechanics Microengineering* **28,** 025012 (2018).

58. Khaderi, S. N., Baltussen, M. G. H. M., Anderson, P. D., den Toonder, J. M. J. & Onck, P. R. Breaking of symmetry in microfluidic propulsion driven by artificial cilia. *Phys. Rev. E* **82,** 027302 (2010).

59. Wang, Y., den Toonder, J., Cardinaels, R. & Anderson, P. A continuous roll-pulling approach for the fabrication of magnetic artificial cilia with microfluidic pumping capability. *Lab. Chip* **16,** 2277–2286 (2016).

60. Khaderi, S. N. *et al.* Magnetically-actuated artificial cilia for microfluidic propulsion. *Lab. Chip* **11,** 2002–2010 (2011).

61. Roper, M. *et al.* On the dynamics of magnetically driven elastic filaments. *J. Fluid Mech.* **554,** 167 (2006).

62. Hanasoge, S., Hesketh, P. J. & Alexeev, A. Microfluidic pumping using artificial magnetic cilia. *Microsyst. Nanoeng.* **4,** 11 (2018).

63. Hanasoge, S., Ballard, M., J. Hesketh, P. & Alexeev, A. Asymmetric motion of magnetically actuated artificial cilia. *Lab. Chip* **17,** 3138–3145 (2017).

64. Fahrni, F., Prins, M. W. J. & van Ijzendoorn, L. J. Micro-fluidic actuation using magnetic artificial cilia. *Lab. Chip* **9,** 3413 (2009).

65. Vilfan, M. *et al.* Self-assembled artificial cilia. *Proc. Natl. Acad. Sci.* **107,** 1844–1847 (2010).

66. Toonder, J. den *et al.* Artificial cilia for active micro-fluidic mixing. *Lab. Chip* **8,** 533 (2008).

67. Khaderi, S. N., den Toonder, J. M. J. & Onck, P. R. Magnetic Artificial Cilia for Microfluidic Propulsion. in *Advances in Applied Mechanics* **48,** 1–78 (Elsevier, 2015).

68. Khaderi, S. N. *et al.* Nature-inspired microfluidic propulsion using magnetic actuation. *Phys. Rev. E* **79,** 046304 (2009).

69. Khaderi, S. N. & Onck, P. R. Fluid–structure interaction of three-dimensional magnetic artificial cilia. *J. Fluid Mech.* **708,** 303–328 (2012).

70. Khaderi, S. N., den Toonder, J. M. J. & Onck, P. R. Magnetically Actuated Artificial Cilia: The Effect of Fluid Inertia. *Langmuir* **28,** 7921–7937 (2012).

71. Balazs, A. C., Bhattacharya, A., Tripathi, A. & Shum, H. Designing Bioinspired Artificial Cilia to Regulate Particle?Surface Interactions. *J. Phys. Chem. Lett.* **5,** 1691–1700 (2014).

72. Alexeev, A., Yeomans, J. M. & Balazs, A. C. Designing Synthetic, Pumping Cilia That Switch the Flow Direction in Microchannels. *Langmuir* **24,** 12102–12106 (2008).

73. Belardi, J., Schorr, N., Prucker, O. & Rühe, J. Artificial cilia: generation of magnetic actuators in microfluidic systems. *Adv. Funct. Mater.* **21,** 3314–3320 (2011).

74. Jogschies, L., Rittinger, J., Klaas, D. & Wurz, M. C. Stress Reduction in Sputtered Thin NiFe 81/19 Layers for Magnetic Field Sensors. *Procedia Technol.* **26,** 162–168 (2016).

75. Brennen, C. & Winet, H. Fluid Mechanics of Propulsion by Cilia and Flagella. *Annu. Rev. Fluid Mech.* **9,** 339–398 (1977).

76. Zhou, Z. *et al.* Evaluation of Young's Modulus and Residual Stress of NiFe Film by Microbridge Testing, Evaluation of Young's Modulus and Residual Stress of NiFe Film by Microbridge Testing. *J. Mater. Sci. Technol.* **22,** 345–348 (2009).

77. Babataheri, A., Roper, M., Fermigier, M. & Du Roure, O. Tethered fleximags as artificial cilia. *J. Fluid Mech.* **678,** 5–13 (2011).

78. Fluid-Structure Interaction, COMSOL Multiphysics® reference manual. version 5.3. (2017).

79. Khaderi, S. N., Toonder, J. M. J. den & Onck, P. R. Microfluidic propulsion by the metachronal beating of magnetic artificial cilia: a numerical analysis. *J. Fluid Mech.* **688,** 44–65 (2011).

80. Lauga, E. Life around the scallop theorem. *Soft Matter* **7,** 3060–3065 (2011).

81. Sampaio, P. *et al.* Left-right organizer flow dynamics: how much cilia activity reliably yields laterality? *Dev. Cell* **29,** 716–728 (2014).

82. Lodish, H. *et al.* Cilia and Flagella: Structure and Movement. in *Molecular Cell Biology*. Section 19.4, New York, USA (2000).

83. Huang, B. K. & Choma, M. A. Microscale imaging of cilia-driven fluid flow. *Cell. Mol. Life Sci.* **72,** 1095–1113 (2015).

84. Funfak, A. *et al.* Paramecium swimming and ciliary beating patterns: a study on four RNA interference mutations. *Integr. Biol.* **7,** 90–100 (2015).

85. Satir, P., Heuser, T. & Sale, W. S. A Structural Basis for How Motile Cilia Beat. *Bioscience* **64,** 1073–1083 (2014).

86. denToonder, J. & Onck, P. *Artificial Cilia*. (RCS Publishing. Cambridge, UK, 2013). doi:10.1039/9781849737098

87. Alexeev, A., Yeomans, J. M. & Balazs, A. C. Designing Synthetic, Pumping Cilia That Switch the Flow Direction in Microchannels. *Langmuir* **24,** 12102–12106 (2008).

88. Oh, K., Smith, B., Devasia, S., Riley, J. J. & Chung, J.-H. Characterization of mixing performance for bio-mimetic silicone cilia. *Microfluid. Nanofluidics* **9,** 645–655 (2010).

89. Wang, Y., Gao, Y., Wyss, H., Anderson, P. & den Toonder, J. Out of the cleanroom, self-assembled magnetic artificial cilia. *Lab. Chip* **13,** 3360–3366 (2013).

90. Laser, D. J. & Santiago, J. G. A review of micropumps. *J. Micromechanics Microengineering* **14,** R35 (2004).

91. Toonder, J. den *et al.* Artificial cilia for active micro-fluidic mixing. *Lab. Chip* **8,** 533 (2008).

92. Hussong, J. *et al.* Experimental investigation of the flow induced by artificial cilia. *Lab. Chip* **11,** 2017–2022 (2011).

93. Chateau, S., Favier, J., 'Ortona, U. D. & Poncet, S. Transport efficiency of metachronal waves in 3d cilia arrays immersed in a two-phase flow. *ArXiv170308313 Phys.* (2017).

94. Xia, Y. & Whitesides, G. M. Soft Lithography. *Annu. Rev. Mater. Sci.* **28,** 153–184 (1998).

95. Blake, J. On the movement of mucus in the lung. *J. Biomech.* **8,** 179–190 (1975).

96. Mitran, S. M. Metachronal wave formation in a model of pulmonary cilia. *Comput. Struct.* **85,** 763–774 (2007).

97. Elgeti, J. & Gompper, G. Emergence of metachronal waves in cilia arrays. *Proc. Natl. Acad. Sci.* **110,** 4470–4475 (2013).

98. Wilkinson, M. *The Story of Life in Ten Movements*. (Basic Books, 2016).

99. Aiello, E. & Sleigh, M. A. The metachronal wave of lateral cilia of Mytilus edulis. *J. Cell Biol.* **54,** 493–506 (1972).

100. Gueron, S., Levit-Gurevich, K., Liron, N. & Blum, J. J. Cilia internal mechanism and metachronal coordination as the result of hydrodynamical coupling. *Proc. Natl. Acad. Sci.* **94,** 6001–6006 (1997).

101. Sleigh, M. A. Coordination of the Rhythm of Beat in Some Ciliary Systems. in *International Review of Cytology* (eds. Bourne, G. H., Danielli, J. F. & Jeon, K. W.) **25,** 31–54 (Academic Press, 1969).

102. Machemer, H. Ciliary activity and the origin of metachrony in Paramecium: effects of increased viscosity. *J. Exp. Biol.* **57,** 239–259 (1972).

103. Osterman, N. & Vilfan, A. Finding the ciliary beating pattern with optimal efficiency. *Proc. Natl. Acad. Sci.* **108,** 15727–15732 (2011).

104. Khaderi, S. N., den Toonder, J. M. J. & Onck, P. R. Fluid flow due to collective non-reciprocal motion of symmetrically-beating artificial cilia. *Biomicrofluidics* **6,** 014106-014106–14 (2012).

105. Guirao, B. & Joanny, J.-F. Spontaneous Creation of Macroscopic Flow and Metachronal Waves in an Array of Cilia. *Biophys. J.* **92,** 1900–1917 (2007).

106. Ding, Y. & Kanso, E. Selective particle capture by asynchronously beating cilia. *Phys. Fluids* **27,** 121902 (2015).

107. Tsumori, F. *et al.* Metachronal wave of artificial cilia array actuated by applied magnetic field. *Jpn. J. Appl. Phys.* **55,** 06GP19 (2016).

108. Cebers, A. & Livanovics, R. Flexible ferromagnetic filaments as artificial cilia. *Int. J. Mod. Phys. B* **25,** 935–941 (2011).

109. Hanasoge, S. *et al.* Active fluid mixing with magnetic microactuators for capture of Salmonella. in (eds. Kim, M. S., Chao, K. & Chin, B. A.) 986405 (2016). doi:10.1117/12.2225571

110. Hanasoge, S., J. Hesketh, P. & Alexeev, A. Metachronal motion of artificial magnetic cilia. *Soft Matter* **14,** 3689–3693 (2018).

111. Schiele, I. & Hillerich, B. Comparison of lateral and vertical switches for application as microrelays. *J. Micromechanics Microengineering* **9,** 146 (1999).

112. Syms, R. R. A. & Moore, D. F. Optical MEMS for telecoms. *Mater. Today* **5,** 26–35 (2002).

113. Rosa, M. A., Bruyker, D. D., Völkel, A. R., Peeters, E. & Dunec, J. A novel external electrode configuration for the electrostatic actuation of MEMS based devices. *J. Micromechanics Microengineering* **14,** 446–451 (2004).

114. Hoffmann, M., Nüsse, D. & Voges, E. Electrostatic parallel-plate actuators with large deflections for use in optical moving-fibre switches. *J. Micromechanics Microengineering* **11,** 323–328 (2001).

115. Rollier, A.-S., Legrand, B., Collard, D. & Buchaillot, L. The stability and pull-in voltage of electrostatic parallel-plate actuators in liquid solutions. *J. Micromechanics Microengineering* **16,** 794 (2006).

116. Seeger, J. I. & Boser, B. E. Charge control of parallel-plate, electrostatic actuators and the tip-in instability. *J. Microelectromechanical Syst.* **12,** 656–671 (2003).

117. Krylov, S. & Bernstein, Y. Large displacement parallel plate electrostatic actuator with saturation type characteristic. *Sens. Actuators Phys.* **130–131,** 497–512 (2006).

118. Seeger, J. I., Boser, B. E. & Hall, C. Dynamics And Control of Parallel-Plate Actuators Beyond The Electrostatic Instability. 4

119. Dodd, J. M. Ciliary Feeding Mechanisms in Anuran Larvæ. *Nature* **165,** 283 (1950).

120. Atkins, D. Ciliary Feeding Mechanisms of Brachiopods. *Nature* **177,** 706–707 (1956).

121. Pernet, B., Harris, L. H. & Schroeder, P. Development and larval feeding in the capitellid annelid Notomastus cf. tenuis. *Biol. Bull.* **228,** 25–38 (2015).

122. Fenchel, T. Suspension feeding in ciliated protozoa: Feeding rates and their ecological significance. *Microb. Ecol.* **6,** 13–25 (1980).

123. Riisgård, H. U. & Larsen, P. S. Minireview: Ciliary filter feeding and bio-fluid mechanics—present understanding and unsolved problems. *Limnol. Oceanogr.* **46,** 882–891 (2001).

124. Mayne, R., Whiting, J. G. H., Wheway, G., Melhuish, C. & Adamatzky, A. Particle sorting by Paramecium cilia arrays. *Biosystems* **156–157,** 46–52 (2017).

125. Sleigh, M. A. & Barlow, D. Collection of Food by Vorticella. *Trans. Am. Microsc. Soc.* **95,** 482–486 (1976).

126. Pepper, R. E. *et al.* A New Angle on Microscopic Suspension Feeders near Boundaries. *Biophys. J.* **105,** 1796–1804 (2013).

127. Ryu, S., Pepper, R. E., Nagai, M. & France, D. C. Vorticella: A Protozoan for Bio-Inspired Engineering. *Micromachines* **8,** 4 (2016).

128. Mayer, S. Particle capture in the crown of the ciliary suspension feeding polychaete Sabella penicillus: videotape recordings and interpretations. *Mar. Biol.* **119,** 571–582 (1994).

129. Hart, M. W. Particle captures and the method of suspension feeding by echinoderm larvae. *Biol. Bull.* **180,** 12–27 (1991).

130. Grünbaum, D., Eyre, D. & Fogelson, A. Functional Geometry Of Ciliated Tentacular Arrays In Active Suspension Feeders. 15

131. Liu, C., Lagae, L. & Borghs, G. Manipulation of magnetic particles on chip by magnetophoretic actuation and dielectrophoretic levitation. *Appl. Phys. Lett.* **90,** 184109 (2007).

132. Wu, Z., Willing, B., Bjerketorp, J., Jansson, J. K. & Hjort, K. Soft inertial microfluidics for high throughput separation of bacteria from human blood cells. *Lab. Chip* **9,** 1193–1199 (2009).

133. Nagrath, S. *et al.* Isolation of rare circulating tumour cells in cancer patients by microchip technology. *Nature* **450,** 1235–1239 (2007).

134. Pratt, E. D., Huang, C., Hawkins, B. G., Gleghorn, J. P. & Kirby, B. J. Rare Cell Capture in Microfluidic Devices. *Chem. Eng. Sci.* **66,** 1508–1522 (2011).

135. Zhang, J. *et al.* Fundamentals and applications of inertial microfluidics: a review. *Lab. Chip* **16,** 10–34 (2015).

136. Hanasoge, S., Devendra, R., Diez, F. J. & Drazer, G. Electrokinetically driven deterministic lateral displacement for particle separation in microfluidic devices. *Microfluid. Nanofluidics* **18,** 1195–1200 (2015).

137. Gleghorn, J. P. *et al.* Capture of circulating tumor cells from whole blood of prostate cancer patients using geometrically enhanced differential immunocapture (GEDI) and a prostate-specific antibody. *Lab. Chip* **10,** 27–29 (2010).

138. Ji, H. M. *et al.* Silicon-based microfilters for whole blood cell separation. *Biomed. Microdevices* **10,** 251–257 (2008).

139. Wang, Z. *et al.* Microfluidic CD4+ T-cell counting device using chemiluminescence-based detection. *Anal. Chem.* **82,** 36–40 (2010).

140. Murthy, S. K., Sin, A., Tompkins, R. G. & Toner, M. Effect of flow and surface conditions on human lymphocyte isolation using microfluidic chambers. *Langmuir ACS J. Surf. Colloids* **20,** 11649–11655 (2004).

141. Rotem, S., Raz, N., Kashi, Y. & Mor, A. Bacterial Capture by Peptide-Mimetic Oligoacyllysine Surfaces. *Appl. Environ. Microbiol.* **76,** 3301–3307 (2010).

142. Hosseinidoust, Z., Van de Ven, T. G. M. & Tufenkji, N. Bacterial Capture Efficiency and Antimicrobial Activity of Phage-Functionalized Model Surfaces. *Langmuir* **27,** 5472–5480 (2011).

143. Andree, K. C. *et al.* Capture of Tumor Cells on Anti-EpCAM-Functionalized Poly(acrylic acid)-Coated Surfaces. *ACS Appl. Mater. Interfaces* **8,** 14349–14356 (2016).

144. Ivnitski, D., Abdel-Hamid, I., Atanasov, P. & Wilkins, E. Biosensors for detection of pathogenic bacteria. *Biosens. Bioelectron.* **14,** 599–624 (1999).

145. Sivagnanam, V., Sayah, A., Vandevyver, C. & Gijs, M. Micropatterning of protein-functionalized magnetic beads on glass using electrostatic self-assembly. *Sens. Actuators B Chem.* **132,** 361–367 (2008).

146. Ma, L., Zhang, G. & Doyle, M. P. Green Fluorescent Protein Labeling of Listeria, Salmonella, and Escherichia coli O157:H7 for Safety-Related Studies. *PLoS ONE* **6,** e18083 (2011).

147. Owen, D. Mixing And Sampling In A Microfluidic Channel Using Rotating Magnetic Microbeads [Ph.D. Dissertation]. (2016).